



## Index of contributed posters CMiF 2019

<b>P01</b>	Ksenia	Loskutova	KTH Royal Institute of Technology (SE)
<b>P02</b>	Zhixiong	Gong	Université de Lille (FR)
<b>P03</b>	Mahdi	Rezayati Charan	Lund University (SE)
<b>P04</b>	Utkarsh	Jain	University of Twente (NL)
<b>P05</b>	Bjørn G	Winckelmann	Technical University of Denmark (DK)
<b>P06</b>	André Gugele	Steckel	Technical University of Denmark (DK)
<b>P07</b>	Amirabas	Bakhtiari	Bundeswehr University (DE)
<b>P08</b>	Chuanyu	Zhang	Université Paris Diderot (FR)
<b>P09</b>	William Naundrup	Bodé	Technical University of Denmark (DK)
<b>P10</b>	Jonas Helboe	Jørgensen	Technical University of Denmark (DK)
<b>P11</b>	Julien	Bouvard	Université Paris-Sud (FR)
<b>P12</b>	Marvin	Detert	University of Twente (NL)
<b>P13</b>	Cecile	Lalanne	Sorbonne Université (FR)
<b>P14</b>	Wojciech	Kwiciński	University of Twente (NL)
<b>P15</b>	Steven	Armstrong	Northumbria University (GB)
<b>P16</b>	Hernán	Barrio Zhang	Northumbria University (GB)
<b>P17</b>	Miguel Angel	Quetzeri-Santiago	Queen Mary University of London (GB)
<b>P18</b>	Saurabh	Nath	ESPCI (FR)
<b>P19</b>	Aditya	Jha	EPSCI & Ecole Polytechnique (FR)
<b>P20</b>	Diego	Díaz	Max Planck Inst, Polymer Research (DE)
<b>P21</b>	Alexis	Darras	University of Liège (BE)
<b>P22</b>	Paul	Lilin	Massachusetts Institute of Technology (US)
<b>P23</b>	Ricardo Arturo	Lopez de la Cruz	University of Twente (NL)
<b>P24</b>	Lijun	Thayyil Raju	University of Twente (NL)
<b>P25</b>	Mathieu	Oléron	Université Paris Diderot (FR)
<b>P26</b>	Rui	Yang	University of Twente (NL)
<b>P27</b>	Frederik Lange	Zafiryadis	Technical University of Denmark (DK)
<b>P28</b>	Yogesh	Jethani	University of Twente (NL)
<b>P29</b>	Lennart	van de Velde	University of Twente (NL)
<b>P30</b>	Yanshen	Li	University of Twente (NL)
<b>P31</b>	Qi	Wang	University of Twente (NL)
<b>P32</b>	Tanumoy	Dhar	JNCASR, Bangalore (IN)
<b>P33</b>	Manon	L'Estimé	ESPCI (FR)
<b>P34</b>	Maria	Tatulea-Codrean	University of Cambridge (GB)
<b>P35</b>	Antoine	Lagarde	Sorbonne Université & CNRS (FR)
<b>P36</b>	Ylona	Collard	University of Liege (BE)
<b>P37</b>	Martin Herbert	Essink	University of Twente (NL)
<b>P38</b>	Tom	Maddalena	École Polytechnique (FR)
<b>P39</b>	Yibo	Chen	University of Twente (NL)
<b>P40</b>	Alessandro	Bongarzone	EPFL (CH)



# The physical properties of cellulose nanofiber-coated capsules in an ultrasonic standing wave

Ksenia Loskutova<sup>1</sup>, Morteza Ghorbani<sup>1,2</sup>, and Dmitry Grishenkov<sup>1</sup>

<sup>1</sup>Department of Biomedical Engineering and Health Systems, KTH Royal Institute of Technology, Stockholm, Sweden

E-mail: [ksestial@kth.se](mailto:ksestial@kth.se), URL: <http://www.fysik.dtu.dk/CMiF2019>

<sup>2</sup>Mechatronics Engineering Program, Faculty of Engineering and Natural Science, Sabanci University, Istanbul, Turkey

## Introduction

Acoustic droplet vaporization (ADV) is a physical process in which a liquid undergoes phase-transition to gas after ultrasound exposure. ADV has great potential in different medical applications involving ultrasound, such as molecular imaging [1] and localized drug delivery [2]. Recently, a novel type of capsules has been developed by Ghorbani et al. [3] with a cellulose nanofiber (CNF) shell and perfluoropentane (PFC5) core that is able to go through ADV at medically approved pressures. These capsules have the potential to be used as drug carriers in localized drug delivery. Previously, it was shown that cells are relocated to pressure anti-nodes when suspended in a density changing agent and that the cell viability was not affected [5]. Therefore, the medical potential of the novel capsules could be tested on tumor spheroids created by USW for realistic simulations [6]. In this experimental work, the physical properties such as density and compressibility of these capsules are studied in a temperature-controlled acoustophoresis setup.

## Materials and methods

The capsules are produced by adding PFC5 to a 0.28 wt% cationic CNF solution prepared according to a scheme described elsewhere (Svagan et al.) and mixing them together using a sonicator. The size distribution of the capsules was determined using dynamic light scattering (ZetaSizer Nano ZS, Malvern Panalytical, UK) and optical microscopy (Eclipse Ni-E, Nikon Corporation, Japan). The mean diameter was found to be  $1.36 \pm 0.43 \mu\text{m}$ .

A glass-silicon-glass microfluidic device shown in figure 1 (GeSim GmbH, Dresden, Germany) was used for measurements in the acoustophoresis setup. For acoustophoretic manipulation the lead zirconate titanium (PZT) transducer with fundamental driving frequency of 2.8 MHz is mounted on the chip by water-soluble glue (Tensive conductive adhesive gel by Perker Labs Inc. USA). The width of the channel inside the device was  $535 \mu\text{m}$ , and the ultrasound frequency was set to 2.70 MHz so that three pressure anti-nodes formed: two at the walls and one in the middle of the microchannel. Capsules were mixed with  $10 \mu\text{m}$  diameter polystyrene beads suspended in distilled water and exposed to ultrasonic standing waves. A Point Grey camera was used to image the motion of both capsules and beads. From the collected images, the energy density inside the channel and the contrast factor of the capsules were estimated.

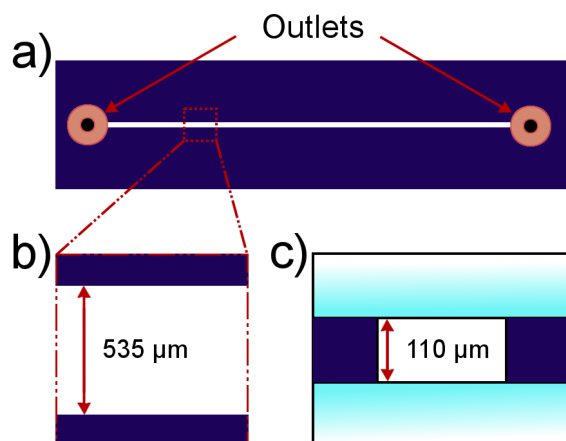


**Figure 1:** (a) The microfluidic device as seen from the top. The device is a glass-silicon-glass construction with the microchannel etched into the silicon. Two outlets enable connection to the microchannel through tubing. (b) Zoomed-in image of the microchannel as seen from the top. The microchannel width is  $620 \mu\text{m}$ . (c) The microchannel as seen at the cross-section. The depth of the microchannel is  $110 \mu\text{m}$ .

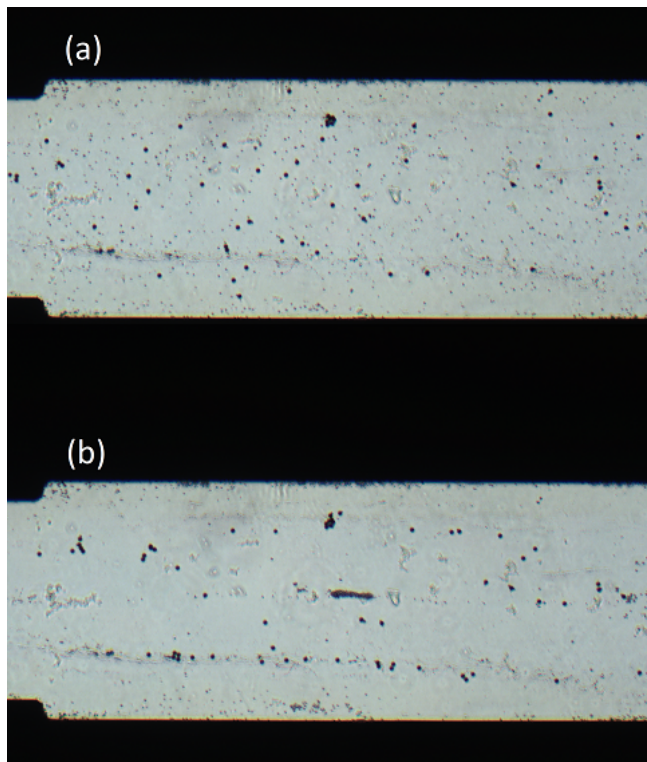


**Figure 2:** Image showing the placement of beads and capsules inside the microchannel (a) before USW, and (b) after USW. The polystyrene beads are relocated to the pressure nodes, while the capsules are collected at the pressure anti-nodes.

## Results and discussion

As can be seen in figure 2, the polystyrene beads and capsules were relocated to different locations due to different acoustic factors. The polystyrene beads moved to the pressure nodes, while the capsules go to the pressure anti-nodes. The reason is the difference in the sign of the acoustic contrast factor due to differences in compressibility and density. These tests should therefore be repeated at different voltages for pressure calibration and to evaluate the compressibility of the capsules.

## Conclusion

The capsules relocated to pressure anti-nodes when exposed to USW, as was predicted by theory. It would be of great interest to redo measurements at various voltages for pressure calibration and introduce tumor spheroids to see the bioeffects with non-loaded and loaded capsules.

## References

- [1] Sheeran, Paul S and Streeter, Jason E and Mullin, Lee B and Matsunaga, Terry O and Dayton, Paul A. *Ultrasound in medicine & biology* 39(5), 893-902 (2013).
- [2] Ho, Yi-Ju and Yeh, Chih-Kuang. *Theranostics* 7(6), 1477-1488 (2017).
- [3] Ghorbani, Morteza and Olofsson, Karl and Benjamins, Jan-Willem and Grishenkov, Dmitry and Svagan, Anna. Submitted to *Langmuir*, under review.
- [4] Svagan, Anna J and Benjamins, Jan-Willem and Al-Ansari, Zeinab and Shalom, Daniel Bar and Müllertz, Anette and Wågberg, Lars and Löbmann, Korbinian. *Journal of Controlled Release* 244, 74-82 (2016).
- [5] Loskutova, Ksenia. Master's thesis, KTH Royal Institute of Technology (2018).
- [6] Olofsson, Karl and Carannante, V and Ohlin, Mathias and Frisk, Thomas and Kushiro, K and Takai, M and Lundqvist, A and Önfelt, Björn and Wiklund, Martin. *Lab on a Chip* 1816, 2466-2476 (2018).



# Assembly of small particles with synchronized acoustical vortices

Zhixiong Gong, Michael Baudoin

Univ. Lille, CNRS, Centrale Lille, ISEN, Univ. Polytechniques Hauts-de-France, UMR 8520-IEMN, International laboratory LIA/LICS, F-59000 Lille, France

E-mail: [zhixiong.gong@iemn.fr](mailto:zhixiong.gong@iemn.fr), URL: <http://films-lab.univ-lille1.fr/michael/>

## Introduction

The efficiency of acoustical tweezers based on acoustical vortices to trap and manipulate individual particles selectively at microscales has been recently demonstrated [1-3]. Nevertheless, the possibility to assemble several particles with these tweezers has not been demonstrated yet and is essential for many applications such as tissue engineering or microsystems assembly. This operation remains challenging since the ring of high intensity used for particles trapping is repulsive for particles located outside the trap, hence preventing the assembly of several particles. In this work, we show theoretically that it is possible to assemble particles if they are trapped at the center of two synchronized vortices. Indeed, the destructive interference between two neighboring synchronized vortices provokes the creation of a pathway between the two rings, hence enabling the assembly of particles located at the core of each vortex. This work paves the way toward particles assembly with multiple vortices.

## Theoretical Methods

In this work we consider the interaction between two synchronized cylindrical Bessel beams with parallel axes for 2D particles assembly, as shown in Fig.1(a). While it is not a necessary condition, we will consider particles with the same acoustic properties for the sake of simplicity. The complex pressure field resulting from the interaction between two acoustical vortices can be expressed as:

$$p = \sum_{j=1,2} A_j J_m(k_{\perp} r_j) e^{im\theta_j}, \text{ with } r_{1,2} e^{i\theta_{1,2}} = r e^{i\theta} \pm s \quad (1)$$

where  $A_j$ ,  $r_j$  and  $j$  are the beam amplitude, radial distance with respect to the origin of the  $j$ th vortex beam and the azimuthal angles, respectively (see Fig. 1(b)).  $m$  is the topological number (i.e., vortex order),  $J_m$  the cylindrical Bessel function of the first kind,  $k_{\perp} = k \sin(\gamma)$  the transverse wavenumber with the wavenumber  $k = \omega/c$ ,  $c$  the sound speed in the fluid,  $\omega$  the angular frequency and  $\gamma$  the so-called cone angle. If we consider small particles compared to the wavelength (e.g. polystyrene particles of radius  $a=5 \mu\text{m}$  embedded in water with driving frequency 5 MHz), the radiation force can be obtained from the negative gradient of Gor'kov potential  $\mathbf{F} = -\nabla U$ , with  $U$  [3]

$$U = 2\pi a^3 \rho_0 [f_1 \langle p^2 \rangle / (3\rho_0^2 c_0^2) - f_2 \langle \mathbf{v}^2 \rangle / 2] \quad (2)$$

where the angled bracket indicates time average of indicated arguments. The velocity vector  $\mathbf{v}$  can be calculated with the relationship  $\mathbf{v} = -i/(\rho\omega)\nabla p$ .  $\rho_0$  and  $c_0$  are the fluid density and the acoustic velocity. The coefficients of  $f_1$  and  $f_2$  are given in detail in our recent work [4].

## Gor'kov potential and radiation force: numerical results

If we consider particles initially trapped at the center of two vortices, the calculation shows that as long as the vortices are sufficiently far away from each other, the interaction between the two vortices is weak and each particle is trapped individually at the core of each vortex. When the distance ( $\delta$ ) between the core of the two vortices is reduced, the destructive interaction between the spinning vortices creates a path between the two rings until the vortices merge into a single vortex. The Gor'kov potential and 2D radiation force arrows are depicted on Fig. 2. The computational results demonstrate the ability of synchronized acoustic vortices (here  $m=1$ ) to assemble particles initially located at the center of two separate vortices.

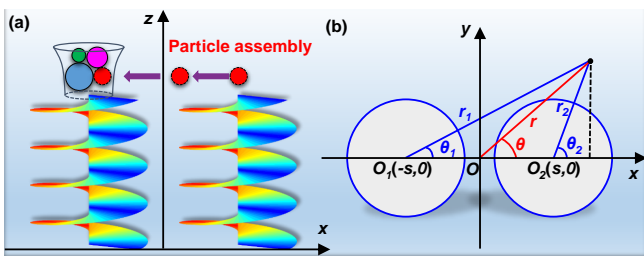


**Figure 1:** Schematic of two cylindrical Bessel vortices. (a) Particle assembly with two acoustical vortices. The particles can have different properties and size within the Rayleigh regime; (b) Geometrical relationship of radii and azimuthal angles in local and global coordinates systems. The left vortex is numbered as  $j=1$  while the right one is  $j=2$ .

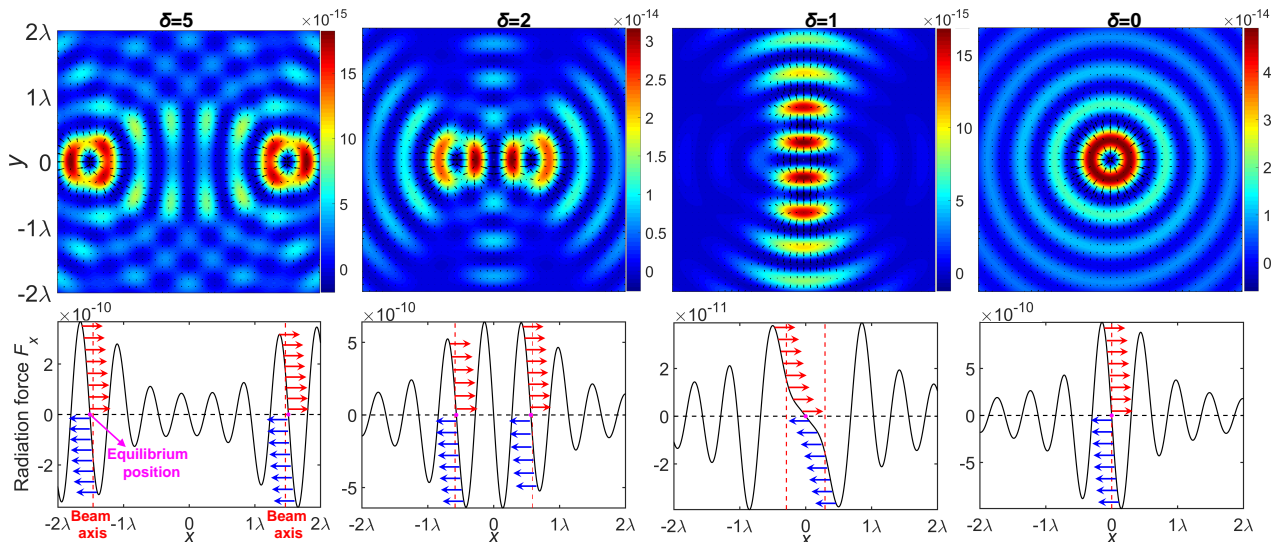


**Figure 2:** Upper rows: Gor'kov potential (color background) and radiation forces (black arrows) resulting from the interaction of two interacting acoustical vortices (of amplitudes  $A = 10^6$  Pa and driving frequency  $f = 1$  MHz) with PS spheres of  $5 \mu\text{m}$  for different offset ratios  $\delta = s/l_0$  (dimensionless distance between the two vortices with  $s$  the distance between the beam axis  $O_{1,2}$  and the origin  $O$  (see Fig.1b) and  $l_0$  the distance between the maximum pressure amplitude on the first ring and the origin of a single vortex beam). Lower row: Lateral forces  $F_x$  applied on the particles as a function of  $x$ . The static equilibrium positions (traps) correspond to the null force values in regions of negative force gradient ( $(\partial F_x/\partial x < 0)$ ). The individual vortex cores (in absence of interference) are represented with a red dashed line. The quasi-static equilibrium positions are indicated by magenta solid spheres.

### Critical Stokes' drag force and speed of moving tweezers

A critical information for practical applications is the speed at which trapped particles can be assembled. Indeed, when the particles are moved, a drag force is applied on the particles. If this drag force exceed the radiation force exerted by the vortex, then the particle can escape. The critical speed of the moving tweezers is thus determined from a balance between the Stokes' drag and the radiation force, when this latter is minimum during the merging process. In practice, this occurs when  $\delta=0.95$  (cf. Fig. 3). This leads to the critical speed  $v_{cr} = F_x^{\text{peak}}(\delta = 0.95)/6\pi\eta$  with  $\eta$  the viscosity. The inset of Fig.3 depicts the linear relationship of critical speed  $v_{cr}$  on various beam amplitude square  $A^2$  for three kinds of materials with acoustic properties given in Ref. [4].

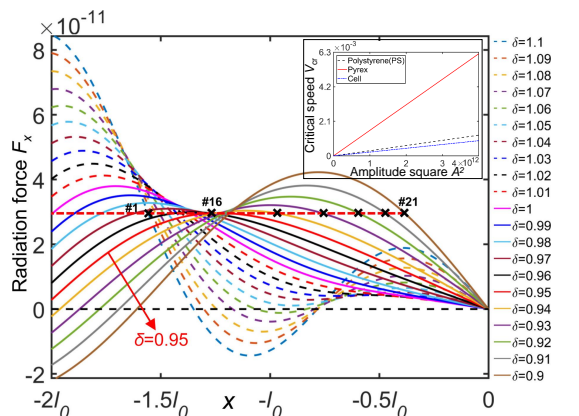


**Figure 3:** Lateral radiation force  $F_x$  applied on PS spheres immersed in water by two interfering vortex beams with offset ratio ranging from  $\delta=1.1$  to  $\delta=0.9$ . The graph only shows the force for particles located in the half plane  $x < 0$  on the  $x$  axis. Results for particles located in the half plane  $x > 0$  can be inferred from these data by simple symmetry. The red dashed line describes the critical radiation force at  $\delta=0.95$  which is balanced by the Stokes drag force to determine the critical velocity  $v_{cr}$  of the moving tweezers. Inset: Critical speed for three specific materials as a linear dependence of the square of the acoustic wave pressure amplitude  $A^2$ .

### Conclusion

In this work, we demonstrate theoretically the possibility to assemble two particles in 2D, and in the long wavelength regime, by using two synchronized vortices. We also investigate the critical speed at which these particles can be assembled, a critical information for engineering applications e.g. in the fields of biophysics and microfluidics.

### References

- [1] D. Baresch, J.-L. Thomas, and R. Marchiano. Phys. Rev. Lett. **116**, 024301 (2016).
- [2] M. Baudoin, *et al.* Sci. Adv **5**, eaav1967 (2019).
- [3] L.P. Gor'kov. Sov. Phys. Dokl. **6**, 773-775 (1962).
- [4] Z. Gong, and M. Baudoin. arXiv:1904.05039v1 (2019).



# Iso-acoustic Focusing Cancer Cell Trajectories in A Diffusing Iodixanol Gradient

Mahdi RezaYati Charan<sup>1</sup> and Per Augustsson<sup>1</sup>

<sup>1</sup>Department of Biomedical Engineering, Lund University, Lund, Sweden  
 E-mails: Mahdi.rezaYati\_charan@bme.lth.se, Per.augustsson@bme.lth.se  
 URL: <http://bme.lth.se/staff/augustsson-per/per-augustsson/>

## The concept of iso-acoustic focusing

The present abstract investigates the acoustic properties of cancer cells based on their trajectories by implementing iso-acoustic focusing (IAF). The technique is based on acoustic radiation forces that can push cells relative to their suspending liquid inside a microchannel. This is a fundamental refinement of an established method called acoustophoresis that has shown potential applications for positioning, concentration, washing, separation and sorting cells [1]. Acoustophoresis is one of the most promising label free approaches, together with e.g. inertia-based, microvortex-based and DLD methods, that allow high enough throughput to enable isolation of target cells in a rich population of other cells. Moreover, acoustophoresis have been shown in a number of research studies to not affect viability or function of cells.

Importantly, IAF overcomes all the three main limitations in conventional acoustophoresis and numerous other methods. IAF enables size-insensitive separation, it can be used with cell-rich suspensions and it pushes the lower size limit to the sub-micrometer regime. IAF is analogous to density gradient centrifugation, where cells are pushed by a centrifugal force to rest in their point of neutral buoyancy and this happens through layered liquids of increasing density. In IAF, cells are instead pushed sideways by an acoustic resonance which is oriented orthogonal to the laminar flow in a vibrating microchannel. Rather than based on density, in IAF, cells reach an equilibrium point called iso-acoustic point (IAP) based on their acoustic properties, more specifically their acoustic impedance ( $Z_{\text{cell}}$ ).

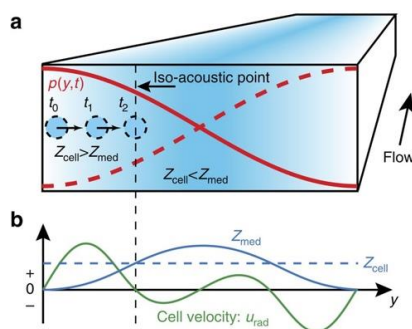


Figure 1: Principal of IAF [1]

As it is schematically shown in figure 1.a, cells suspended in a friendly medium, are introduced near both side walls of the channel and liquid of higher acoustic impedance  $Z_{\text{med}}$  containing no cell is injected in a central inlet to occupy the central part of the flow. The flow velocity in the channel is tuned in a way that a smooth acoustic impedance profile  $Z_{\text{med}}(y)$  takes place by means of molecular diffusion. Cells are moving sideways towards the node of an acoustic resonant pressure field  $p(y,t)$ . Figure 1.b illustrates the distribution of  $Z_{\text{med}}$  and also showing that when the acoustic impedance  $Z_{\text{cell}}$  of a given cell matches  $Z_{\text{med}}$  at the IAP, its transverse velocity  $u_{\text{rad}}$  becomes zero so that its position along  $y$  reflects its individual effective acoustic impedance.

## Experimental work

The silicon chip consisted of a straight channel was sandwiched between two glass slides of thickness 200  $\mu\text{m}$  using anodical bonding. A plate shape zirconate titanate (PZT) transducer bonded on top of the chip was implemented to transfer the sound wave produced by Analog Discovery 2. Optiprep solution containing 60% (w/v) Iodixanol was used to modify the density and speed of sound. At the main channel inlet, three streams

join in a trifurcation of which the two side streams containing 10% Iodixanol, while the center stream containing 36% Iodixanol. A motorized four-port, two-way diagonal valve was used to stop the flow. The valve was used to do a short circuit for the stop flow measurement of cell trajectories. The cancer cells trajectories were studied by recording the motion of the cells using the technique “defocusing particle-tracking (GDPT)” [2]. GDPT is a single-camera particle-tracking method, in which the defocused images of a spherical particle in the depth coordinate  $z$ , are used to monitor particle trajectories in three-dimension. GDPT is basically based on set of calibration images that should be obtained before performing the final measurements. In our case, a stack of calibration images was obtained with an interval of  $2\ \mu\text{m}$  in the depth coordinate by moving a motorized  $z$  stage equipped on the microscope. Eventually, it was assured the  $z$  stage is in the correct height and then, the motion of cells was recorded. The acquired images were analyzed in GDPTlab by performing a normalized cross-correlation and comparing the acquired images with the calibration stack [3]. At the end, the trajectories of cells were constructed.

### Preliminary results and anticipated progress

In figure 2, the recognized cells in GDPTLab are shown on their way to reach to pressure node in the middle of the channel. GDPT was able to track cells with a very good correction factor regarding to the calibration images.

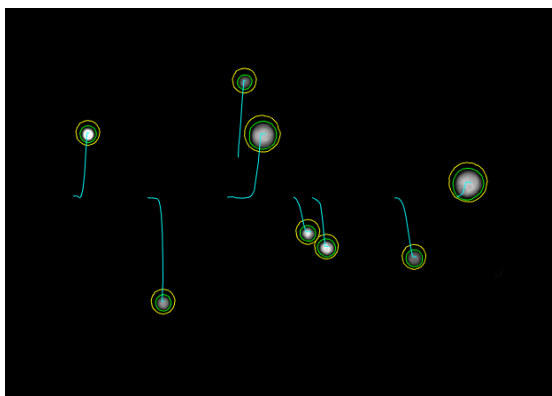


Figure 2: Cell trajectories in an acoustic field

Finally, figure 3 demonstrates the data for the trajectories of cells.

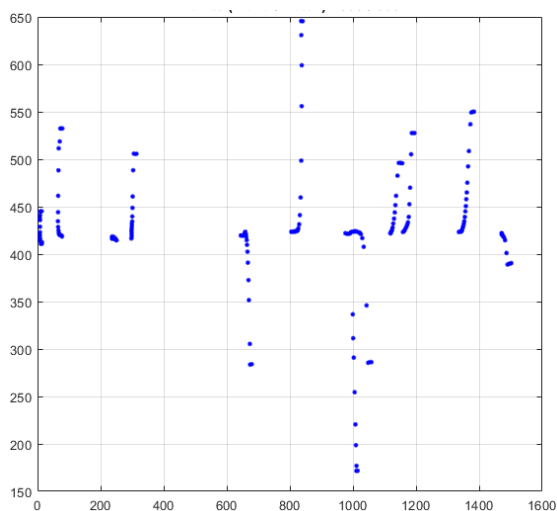


Figure 3: Data obtained from GDPT on how each cell migrates to its final location

In the present abstract our results show that GDPT works very good for cancer cells to track them in a homogeneous fluid while they migrate due to acoustic force. As it is mentioned in the title of the abstract, the next step is to track cancer cells in inhomogeneous fluid to extract their acoustic impedance.

### References

- [1] P. Augustsson et al., *Nature Communications*, **7**, 11556, (2016).
- [2] R. Barnkob et al., *Lab Chip*, **15**, 3556-3560, (2015).
- [3] W. Qiu et al., *Phys. Rev. Applied*, **11**, 024018, (2019).



## Donut sloshing waves

Utkarsh Jain<sup>1</sup>, Francesco Viola<sup>1</sup>, Detlef Lohse<sup>1,2</sup> and Devaraj van der Meer<sup>1</sup>

<sup>1</sup>Physics of Fluids Group and Max Planck Center Twente for Complex Fluid Dynamics, MESA+ Institute and J. M. Burgers Centre for Fluid Dynamics, University of Twente, P.O. Box 217, 7500AE Enschede, the Netherlands

E-mail: [u.jain@utwente.nl](mailto:u.jain@utwente.nl), URL: [www.pof.tnw.utwente.nl](http://www.pof.tnw.utwente.nl)

<sup>2</sup>Max Planck Institute for Dynamics and Self-Organization, Am Fassberg 17, 37077 Göttingen, Germany

### Motivation and context

Gravity waves are a common phenomenon that affects a variety of flows in Nature. Some examples include wave formation in deep water by shear forcing by wind [1], tides, and ocean surface dynamics caused by forcing imposed, for instance, by a tornado [2]. Indeed the forcing from wind can itself induce rogue waves [3–5], which can cause damage to offshore structures in ocean engineering [6,7].

### Experiments

In the present work, we use experiments to study gravity waves' propagation caused by an oscillating pressure over the free surface. We place a flat disk oscillating in air close to a water surface, which imposes a periodic flow in the air layer trapped between the disk and water surface with a frequency imposed by its oscillations. This oscillating air-layer creates waves on the water surface [8]. These surface waves are measured both under and outside the disk's shadow using an in-house experimental method, using which we are able to visualise and reconstruct the instantaneous free surface elevation of the whole domain. A schematic of the setup is shown in figure 1.

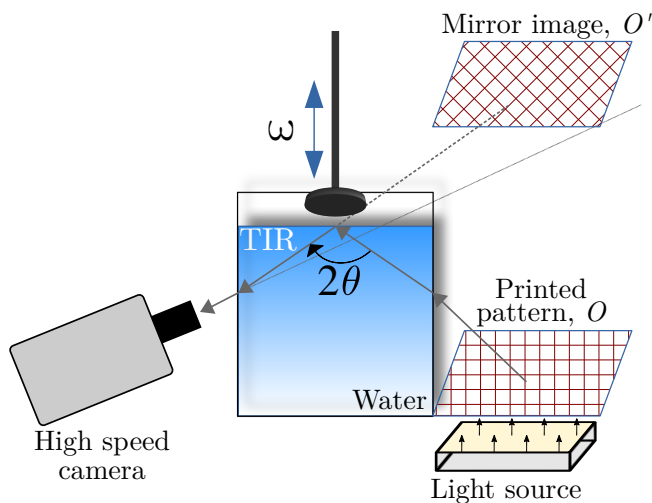


**Figure 1:** Schematic of the experimental setup. A brightly lit, large light source is used to illuminate the printed pattern. The image from the printed pattern is reflected at the water-air interface and enters a suitably placed high speed imaging camera. The water-air interface acts as a mirror due to total internal reflection, and the camera only observes the mirror image. The light rays are shown to help the reader follow the general optics of the problem. Images from the camera are shown in upper panels of figure 2.

### Rationalising observations and modelling

It results that the mass of air under the disk creates a time-harmonic pressure condition on the water surface, which induces sloshing waves. This oscillating mass of air in the gap meets the atmosphere under the disk's edge, thereby limiting the forcing to the region under the disk's shadow. Outside this region, the energy in the surface waves dissipates in the form of outwards moving gravity waves. Some snapshots from an experiment are shown in figure 2.

To rationalise our experimental observations, we model air flow in the gap under the disk using lubrication equations. We find that both in the quasi-steady and unsteady regimes, inertia has little effect in the air layer, at least for the experimental parameters chosen. The resulting oscillating pressure in the air layer triggers gravity waves because it acts as an external forcing in the Young-Laplace equation at the free surface. Thus it serves as the dynamic boundary condition at the free surface. Finally, the inviscid sloshing equations, forced at the free surface by the harmonic pressure, are solved analytically in the limit of small wave amplitude by using Fourier-Bessel series. In particular, the

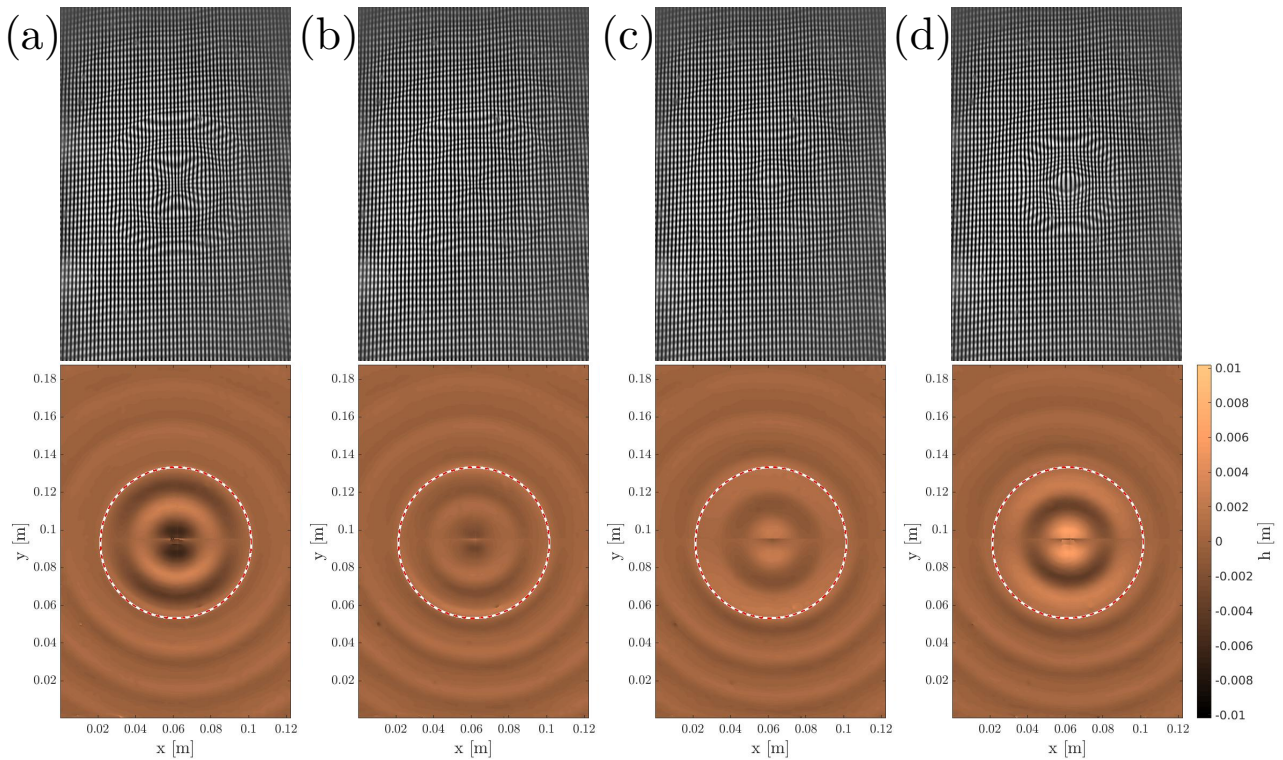


**Figure 2:** Some experimental snapshots of the water surface (top row) and reconstructed water surface profiles (bottom row) from an experiment where an 8 cm wide disk was sinusoidally-shaken above water surface with a frequency of 10Hz. The axis of oscillation lies in the direction perpendicular to the paper. The initial position of the disk was chosen to be 3 mm away from the water surface, and the oscillation amplitude was 2.7 mm. Each successive panel from (a)–(d) is separated by 0.01 s in time. The circle drawn in bottom panels shows the outline of where the disk edges lie.

analytical solution is seen to reproduce the main features observed in the experiments. Sloshing waves from the experiments and analytical solutions are compared.

## Conclusion

We investigate axisymmetric sloshing waves on water surface generated by oscillating a flat disk placed above the water surface. Standing waves are confined to the water surface that lies under the disk, whereas outside this region, we find outwards propagating gravity waves. The free surface behaviour in both the regions is measured experimentally and then modelled mathematically combining lubrication equation for forcing the air pressure and linear inviscid sloshing theory.

## References

- [1] J.W. Miles. *Journal of Fluid Mechanics*, **3(2)**, 185–204 (1957).
- [2] R.L. Walko. *Journal of the Atmospheric Sciences*, **45(16)**, 2251–2267 (1988).
- [3] A.A. Abrashkin and O.E. Oshmarina. *Communications in Nonlinear Science and Numerical Simulation*, **34**, 66–76 (2016).
- [4] A.A. Abrashkin and A. Soloviev. *Physical Review Letters*, **110(1)**, 014501 (2013).
- [5] S. Yan and Q.W. Ma. *European Journal of Mechanics-B/Fluids*, **30(1)**, 1–11 (2011).
- [6] R. Baarholm and O.M. Faltinsen. *Journal of Marine Science and Technology*, **9(1)**, 1–13 (2004).
- [7] O.M. Faltinsen. *Sea Loads on Ships and Offshore Structures*, Cambridge University Press (Cambridge, 1993).
- [8] T.H. Havelock. *Proceedings of the Royal Society of London. Series A, Containing Papers of a Mathematical and Physical Character*, **81(549)**, 398–430 (1908).
- [9] T.H. Havelock. *The London, Edinburgh, and Dublin Philosophical Magazine and Journal of Science*, **8(51)**, 569–576 (1929).
- [10] L. Debnath. *Nonlinear water waves*, Academic Press (1994).



# Modeling piezo-actuation methods for acoustophoresis

Bjørn G. Winckelmann and Henrik Bruus

Department of Physics, Technical University of Denmark, Kongens Lyngby, Denmark  
 E-mail: [s153418@student.dtu.dk](mailto:s153418@student.dtu.dk), URL: <http://www.fysik.dtu.dk/microfluidics>

## Introduction

To produce reliable high throughput acoustophoresis, we seek to understand how different means of piezo-actuation couple into an acoustic half wave mode. Numerical modeling is used to explore the acoustofluidic response of a water-filled microchannel embedded in a pyrex slab. The amplitudes of the acoustic fields are found at resonance to study the effectiveness of different actuation schemes.

## Numerical setup

The numerical studies are carried out in COMSOL Multiphysics as described in Ref. [1], and the simulations are all performed on 2D cross-sections to lower the computational efforts. The base geometry of the simulations is a slab of pyrex with dimensions  $4 \text{ mm} \times 1.5 \text{ mm}$  and an engraved water-filled channel of dimensions  $375 \mu\text{m} \times 160 \mu\text{m}$ . First, a simplified vertical actuation is implemented as a Dirichlet boundary condition on the mechanical displacement field in the bottom of the pyrex slab. The fractional coverage of the vertical actuation is denoted by  $D$ . Two other systems are simulated with piezoelectric actuation by a Pz26 transducer of dimensions  $6 \text{ mm} \times 1 \text{ mm}$ . In one system the transducer is implemented with single electrodes at its top and bottom surfaces, and in the other system the top electrode is split in two by a cut into the transducer. The two transducer configurations are actuated by one or two ac sources respectively, where the double-ac configuration is driven with a phase difference of  $\pi$  between the two power sources. Different placements of the transducer are tested for the single-ac setup, and these placements will be described by the parameter  $F$ . The three different setups are illustrated in figure 1.

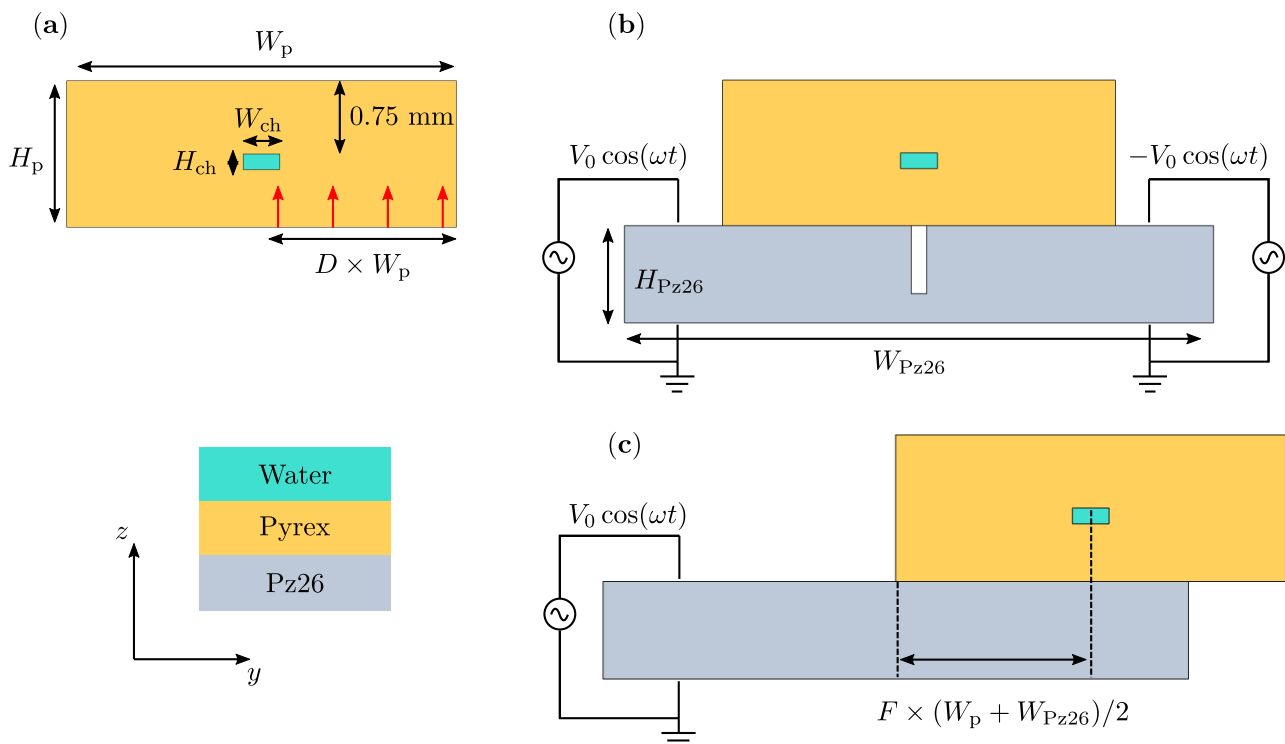


**Figure 1:** (a) A pyrex chip with the simplified Dirichlet-boundary-condition actuation on the mechanical displacement field (illustrated by the red arrows). The parameter  $D$  denotes the fraction of the bottom boundary moving up and down, and the remainder of the bottom boundary is kept stationary. (b) Double electrode system with two ac sources running in antiphase. (c) Single electrode system at a given actuator displacement. For all simulations including the piezoelectric actuator we set  $V_0 = 1 \text{ V}$ .

## Simulation results

Simulations are performed for varying driving frequencies around 2 MHz, and the acoustic energy density  $E_{ac}$  is calculated at each frequency to identify acoustic resonances for each setup. The resonance frequency close to 2 MHz corresponds to an anti-symmetric widthwise half wave pressure mode. Resonance sweeps are performed

at varying values of the geometrical parameters  $D$  and  $F$ , and the acoustic energy density at resonance is found as a function of  $D$  and  $F$ . Further, the time averaged power per electrode area due to the induced polarization current in the transducer  $U_{\text{avg}}$  is found at each frequency, and the power per area normalized acoustic energy densities are calculated for the two systems actuated by piezoelectric transducers. The simulation results for the three setups are shown in figure 2. The resulting curve from varying the parameter  $D$  in the system described in figure 1 (a) is seen to be symmetric around  $D = 0.5$ . This suggests that symmetries in the boundary condition around the center of the fluid channel cannot contribute to the build up of the anti-symmetric resonance mode. The double-ac-actuated system is entirely anti-symmetric by construction and the resonance curve is seen to be elevated compared to most of the resonance strengths found for the single-ac actuated system. The single-ac actuated system responds very differently to various displacements of the actuator, which could cause inconsistency problems for chip batches. Only very specific positionings of the actuator appear to provide resonances comparable in amplitude to the double-ac-actuated configuration. For the completely symmetric case ( $F = 0$ ) the resonance almost vanishes.

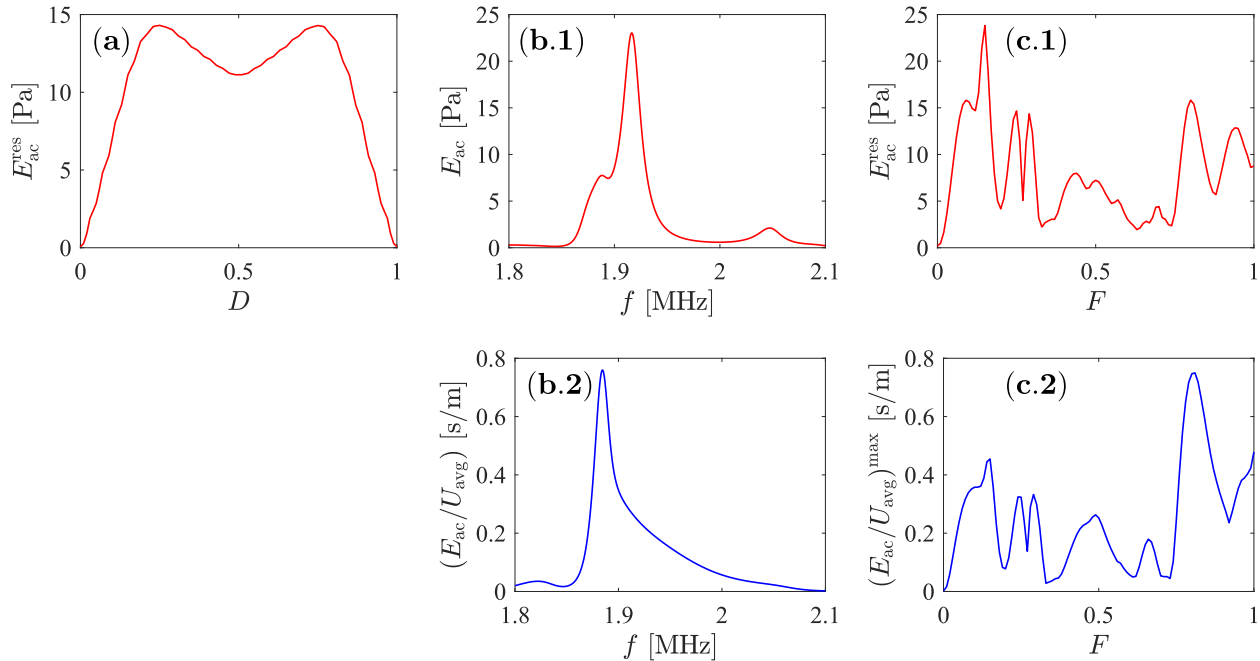


**Figure 2:** (a) The acoustic energy density at resonance  $E_{\text{ac}}^{\text{res}}$  for the artificial actuation with varying coverage. We notice that the curve is symmetric around  $D = 0.5$ , and the optimal coverage is found at  $D = 0.25$  and  $D = 0.75$  respectively. (b) The acoustic energy density  $E_{\text{ac}}$  and the power per area normalized acoustic energy density  $E_{\text{ac}}/U_{\text{avg}}$  as functions of driving frequency for the double-ac-actuated configuration. (c) Acoustic energy density at resonance and the maximum power per area normalized acoustic energy density  $(E_{\text{ac}}/U_{\text{avg}})^{\text{max}}$  as functions of the geometric parameter  $F$ .

## Conclusion

Our numerical analysis suggest that the use of an inherently anti-symmetric actuation method would be very effective for actuation of anti-symmetric modes. At a given voltage the double-ac actuation method created more powerful resonances than what was obtained for most configurations with the more standard single-ac actuation. Generally, the strength of the resonances appears to be very sensitive to the method of actuation, and it would be of great interest to study the agreement between numerical predictions and experimental findings on this.

## References

- [1] NR Skov, JS Bach, BG Winckelmann, and H Bruus, *AIMS Mathematics* **4**, 99-111 (2019).



## Mode anti-crossing in thin-film-membrane-driven acoustofluidics

André G. Steckel and Henrik Bruus

Department of Physics, Technical University of Denmark, Kongens Lyngby, Denmark  
 E-mail: [angust@fysik.dtu.dk](mailto:angust@fysik.dtu.dk), URL: <http://fysik.dtu.dk/microfluidics>

### Introduction

Recently, thin-film-membrane-driven acoustophoresis has been realized in a PZT-driven silicon-glass-based device [1], however many aspects still need to be clarified for this interesting new class of devices. Here, we study numerically how the resulting acoustophoresis depends on the thickness of the silicon membrane, when this is driven by a thin film of the lead-free piezoelectric material  $\text{Al}_{0.6}\text{Sc}_{0.4}\text{N}$ . We find anti-crossing behavior between a membrane mode and a chip mode, which results in an optimal membrane thickness for maximizing the acoustical energy density  $E_{\text{ac}}$  in the fluid. The anti-crossing also results in a band gap in the energy-versus-frequency spectrum.

### The model system

The model device, sketched in Fig. 1(a), consists of a 0.1-mm-thick Pyrex base, onto which is placed a 150- $\mu\text{m}$ -thick silicon slab. A 400- $\mu\text{m}$ -wide microchannel is carved out in the slab, which then is sealed by a silicon lid of thickness  $t_m$  ranging from 2 to 24  $\mu\text{m}$ . The microchannel is filled with water kept at 25  $^\circ\text{C}$ . On the top-side of the membrane is placed a piezoelectric thin film of  $\text{Al}_{0.6}\text{Sc}_{0.4}\text{N}$ .

Acoustic modes are excited in the system by an ac-voltage of 1  $\text{V}_{\text{pp}}$  in the following manner. The bottom-side of the piezoelectric film is grounded, while the top-left side and top-right side of this film is excited in anti-phase. The applied excitation frequency lies in the range from 0.1 to 2 MHz. In Fig. 1(b)-(d) are shown the acoustofluidic response of a device with a 7- $\mu\text{m}$ -thick membrane driven at its lowest resonance frequency 0.50 MHz. In Fig. 1(b) is seen how approximately a standing pressure half-wave  $p_1$  of amplitude 300 kPa is established in the water due to the vertical displacement of the membrane. The acoustic streaming pattern shown in Fig. 1(c) reveals that the acoustic field is not a perfect standing half-wave: in stead of the conventional quadrupolar streaming field, only two dominant flow rolls are seen. Moreover, in Fig. 1(d) we see that the resulting acoustic radiation force acting on suspended 5- $\mu\text{m}$ -diameter polystyrene beads [2] are not resulting in the usual particle focusing along the vertical center plane, but instead at the focusing is directed towards the top-center of the channel.

In the following, the strength of a given acoustic mode is characterized by the average acoustic energy density in the water  $E_{\text{ac}} = \frac{1}{4}\kappa|p_1|^2 + \frac{1}{4}\rho|v_1|^2$  in terms of the acoustic pressure  $p_1$  and the acoustic velocity  $v_1$ , where  $\rho$  and  $\kappa$  is the density and compressibility of water, respectively [2].

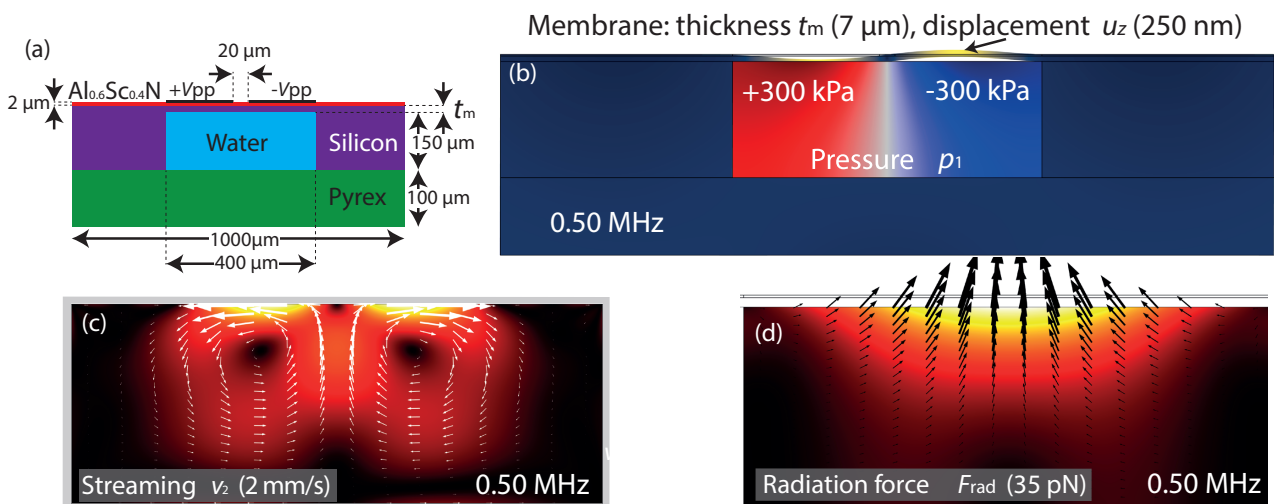


**Figure 1:** (a) A sketch of the model system including the materials and dimensions used in the simulation. The acoustic transducer of the silicon-water-Pyrex device is the silicon membrane of thickness  $t_m$  with the 2- $\mu\text{m}$ -thick piezoelectric  $\text{Al}_{0.6}\text{Sc}_{0.4}\text{N}$  film on top. (b)-(d) are the resulting acoustofluidic response in a device with a 7- $\mu\text{m}$ -thick silicon membrane at the fundamental 0.50-MHz resonance. (b) The pressure  $p_1$  in the water and the vertical displacement  $u_z$  of the membrane. (c) The steady time-averaged acoustic streaming velocity  $\mathbf{v}_2$  in the water showing only two dominant flow rolls. (d) The time-averaged acoustic radiation force  $\mathbf{F}_{\text{rad}}$  acting on 5- $\mu\text{m}$ -diameter polystyrene particles suspended in the water [2].

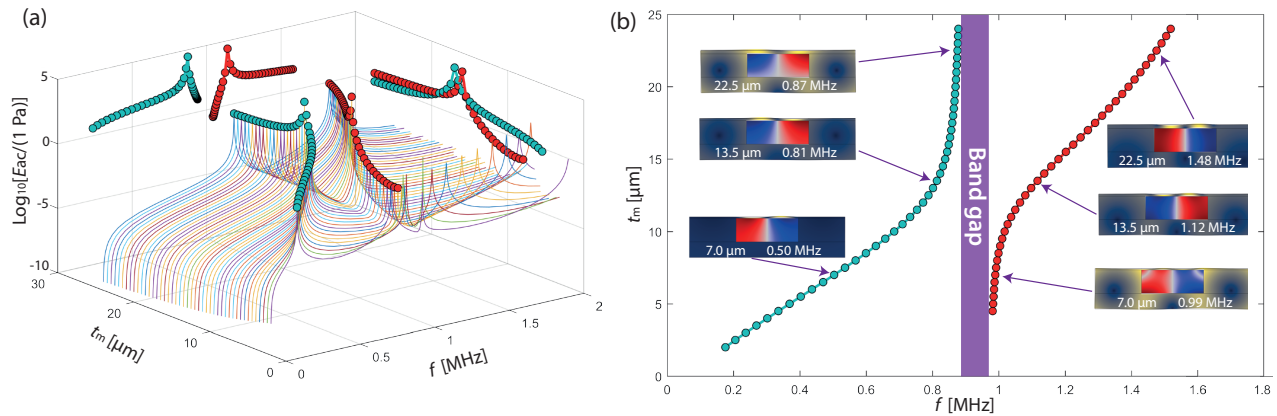


**Figure 2:** (a) A family of energy spectra  $\log_{10}[E_{ac}/(1 \text{ Pa})]$  vs. excitation frequency  $f$  in the range from 0.1 to 2.0 MHz (colored curves) as a function of the membrane thickness  $t_m$  from 2.0 to 24.0  $\mu\text{m}$  in steps of 0.5  $\mu\text{m}$ , where  $E_{ac}$  is the average acoustic energy density in the water. Two anti-crossing branches of peaks (cyan and red dots) are clearly visible, and for further clarity they are projected onto the  $E_{ac}$ - $f$  and the  $E_{ac}$ - $t_m$  planes. (b) Top view of the  $f$ - $t_m$  plane showing the two peak branches (cyan and red dots) as well as insets of six selected resonance modes (blue-red pressure  $p_1$  and dark-blue-yellow displacement  $u_z$ ). Moreover, a frequency band gap without any peaks is identified (purple rectangle).

### Mode anti-crossing as a function of the membrane thickness

The system is analyzed by making a combined sweep in the excitation frequency  $f$  from 0.1 to 2.0 MHz and in the silicon-membrane thickness  $t_m$  from 2 to 24  $\mu\text{m}$  as shown in Fig. 2. In Fig. 2(a) the energy spectra  $E_{ac}$  (colored curves), each corresponding to a given membrane thickness  $t_m$ , clearly show the existence of at least two mode branches identified by the colored dots (cyan and red) representing the peaks in  $E_{ac}$ .

Intuitively, the two branches are related to two different modes in the system: a membrane mode and a solid-chip mode. The frequency of the membrane resonance mode is dependent on the combined thickness of the silicon membrane and piezoelectric film. It is low when the membrane is very thin, and it increases as the membrane thickness increases. The solid-chip mode is essentially independent of the tiny part of the system consisting of the membrane and thin-film actuator. If the two modes were independent, the membrane mode would show up as a straight line of the form  $f_{\text{membrane}}(t_m) = at_m + b$ , while the solid-chip mode would be of the form  $f_{\text{chip}}(t_m) = \text{const}$ . However, the two modes do couple, and therefore we end up with the anti-crossing behavior most clearly seen in Fig. 2(b). The mode of the cyan-colored branch is mainly a membrane mode for low frequencies, however, at  $f = 0.8$  MHz near the anti-crossing point, the character of the mode changes into a  $t_m$ -independent solid-chip mode. The inverse is true for the red-colored branch, which is a solid-chip mode at small membrane thicknesses  $t_m$ , and then past  $t_m \sim 10$   $\mu\text{m}$ , it turns into a  $t_m$ -dependent membrane mode. Near the anti-crossing point, the two modes have a strong interaction, and the resulting acoustic energy density  $E_{ac}$  in the water reaches a maximum giving rise to an optimal membrane thickness for high acoustofluidic action near  $t_m = 13$   $\mu\text{m}$ .

The two interacting modes establish the pressure wave in the water by different mechanisms. For the membrane mode, a high displacement of the membrane will push on the water, and thereby generate a bulk acoustic wave in the water. This mechanism is fundamentally different from the solid-chip mode, where the acoustic wave is established as a standing wave between two acoustically hard, parallel side walls forming an acoustic resonator.

Finally, the anti-crossing behavior is associated with a downward and upward shift, respectively, in the resonance frequencies of the two coupled modes, which results in the frequency band gap represented by the purple rectangle in Fig. 2(b). In this band gap there are no resonance peaks.

### Conclusion

We have shown that in acoustofluidic systems excited by a thin-film-on-a-membrane transducer, it is possible to identify optimal membrane thicknesses for acoustofluidic action. The optimal membrane thickness can be fine tuned by varying the size of the chip, as this will affect the coupling between the underlying membrane modes and solid-chip modes. This work was supported by the BioWings project funded by the European Union's Horizon 2020 Future and Emerging Technologies (FET) programme, grant No. 801267.

### References

- [1] P Reichert, D Deshmukh, L Lebovitz, J Dual *Lab Chip* **18**, 3658 (2018)
- [2] N.R. Skov, J.S. Bach, B.G. Winkelmann, and H. Bruus *AIMS Math* **4**, 99-111 (2019).



## Experimental description of 3D streaming in a square microcavity Bundeswehr University Munich

Amirabas Bakhtiari<sup>1</sup>, Tamara Guimarães<sup>1</sup>, and Christian Kähler<sup>1</sup>

<sup>1</sup>Institute of Fluid Mechanics and Aerodynamics, Bundeswehr University Munich, Munich, Germany  
E-mail: amirabas.bakhtiari@unibw.de, URL: <https://www.unibw.de/lrt7-en>

### Introduction

The acoustic manipulation of microparticles in microfluidic configurations is becoming increasingly popular for medical and biological applications as an excellent technique that can be used for non-contact particle sorting and fluid mixing. The acoustic force can be applied by using acoustic standing waves or inter-digital transducers [1,2].

As two main acoustic effects, the acoustic radiation force and acoustic streaming can displace suspended particles into or from pressure nodes and transfer them over the entire solvent respectively [3,4]. Acoustic streaming like Eckart or bulk-driven acoustic streaming can be generated by the dissipation of acoustic energy flux in the bulk of a viscous fluid [5]. An analytical study was conducted by J.S. Bach and H. Bruus [6] to derive the solutions for the double modes for a shallow square cavity in the bulk-driven acoustic streaming condition. They showed that the strong streaming can be derived by body force  $f_{ac}$  when two overlapping single modes are simultaneously excited at the same frequency. They demonstrated that double modes can be rotating even by a non-rotating actuation coupled in case of presence of a weak asymmetry in the geometry. Due to validating the analytical results, an experimental investigation is done at Fluid Mechanics Institute of Bundeswehr University Munich. All experiments are carried out in a square cavity ( $2 \times 2 \times 0.1 \text{ mm}$ , see Fig 1) with straight inlet/outlet ( $S = 380 \times 100 \text{ }\mu\text{m}$ ) in a microchannel (Micronit) to see the effect of acoustic streaming on the motion of polystyrene particles of different sizes ( $d_p = 1,5$  and  $10 \text{ }\mu\text{m}$ ).

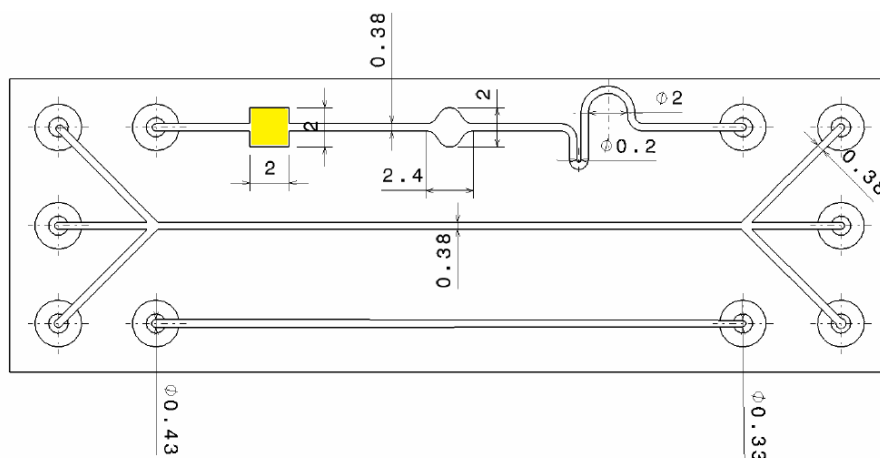


**Figure 1:** Schematic view of the microchip. Measurements are carried out in the square cavity of the top channel (highlighted in yellow).

The microchip, which contains a solution of glycerol-water (23.1%), is acoustically actuated by a piezoelectric transducer (Pz26, Ferroperm piezoceramic). In order to obtain a full standing wave across the square cavity, the excitation frequency  $f = 0.733 \text{ MHz}$  was selected to actuate the microchannel. Imaging setup consists of a microscope (Axio Observer Z1, Zeiss) and a CMOS Camera (PCO Edge 5.5, PCO). The camera is equipped with a cylindrical lens which causes particle-image-distortion that is corresponding to the depth of individual particle (distance from the camera). Post-processing of the acquired data is done using the GDPTlab program [7]. It is expected that the motion of the smallest particle would be dominated by the acoustic streaming forces, the motion of the biggest particles by the acoustic radiation forces, and the motion of intermediate particle size would be influenced by a mixture of both forces. Figure 2 shows the 2D view of the preliminary experimental results of the actuated particles at  $f = 0.733 \text{ MHz}$ .

As expected, the smaller particles ( $1 \text{ }\mu\text{m}$  diameter) show a strong streaming pattern, with the streaming rolls circulating towards and away from the pressure nodes of the actuation pattern. These

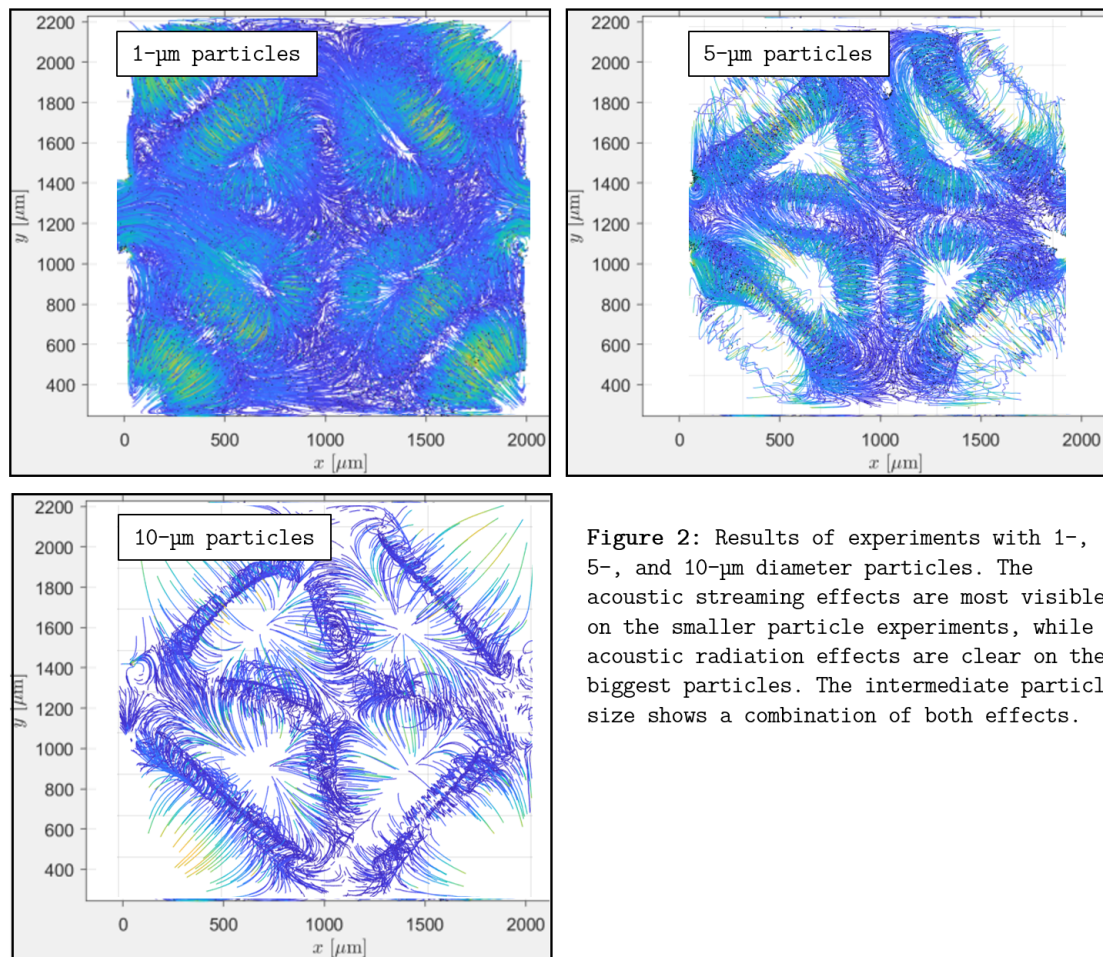


**Figure 2:** Results of experiments with 1-, 5-, and 10- $\mu\text{m}$  diameter particles. The acoustic streaming effects are most visible on the smaller particle experiments, while acoustic radiation effects are clear on the biggest particles. The intermediate particle size shows a combination of both effects.

pressure nodes are very clear in the presented results for the biggest particles (10  $\mu\text{m}$  diameter). For the intermediate-sized particles, a combination of both phenomena is observed, with tighter rolling streaming patterns than in the small particles, and also a tendency of particles to focus in the pressure nodes due to the radiation forces. Even though only the 2D view of the results are shown here, the 3D characteristics of this flow are very clear, unlike the results of the experiments performed by Hagsäter et al. [8], which only described the 2D motion of the particles. The main difference between their experiments and the ones presented in this abstract is the geometry of the square cavity. While theirs was 200  $\mu\text{m}$  in height, this one is only 100  $\mu\text{m}$ , leading to believe that the streaming motion is led by slightly different phenomena. This is to be determined with further experiments in different frequencies.

## Conclusions

With these experiments, it was possible to verify the highly-3D motion of particles of different sizes in a square microcavity. Further work is being done on a detail description of this 3D motion at different actuation frequencies.

## References

- [1] Augustsson, Per, et al. "Iso-acoustic focusing of cells for size-insensitive acousto-mechanical phenotyping." *Nature communications* **7** (2016): 11556.
- [2] Collins, David J., et al. "Two-dimensional single-cell patterning with one cell per well driven by surface acoustic waves." *Nature communications* **6** (2015): 8686.
- [3] King, Louis Vessot. "On the acoustic radiation pressure on spheres." *Proceedings of the Royal Society of London. Series A-Mathematical and Physical Sciences* **147.861** (1934): 212-240.
- [4] Nyborg, Wesley L. "Acoustic streaming near a boundary." *The Journal of the Acoustical Society of America* **30.4** (1958): 329-339.
- [5] Eckart, Carl. "Vortices and streams caused by sound waves." *Physical review* **73.1** (1948): 68.
- [6] Bach, Jacob S., and Henrik Bruus. "Bulk-driven acoustic streaming at resonance in closed microcavities." *arXiv preprint arXiv:1905.09132* (2019).
- [7] Barnkob, Rune, Christian J. Kähler, and Massimiliano Rossi. "General defocusing particle tracking." *Lab on a Chip* **15.17** (2015): 3556-3560.
- [8] Hagsäter, S.M., Glasdam Jensen, T., Bruus, H., and Kutter, J.P. "Acoustic resonances in microfluidic chips: full-image micro-PIV experiments and numerical simulations." *Lab on a Chip* **7** (2007): 1336-1344.



## Comparing direct numerical simulation and perturbation theory on the modelling of acoustic induced streaming around sharp edges

Chuanyu ZHANG<sup>1</sup>, Xiaofeng GUO<sup>1</sup>, Philippe BRUNET<sup>2</sup> and Laurent ROYON<sup>1</sup>

<sup>1</sup>Univ Paris Diderot, Sorbonne Paris Cité, LIED, UMR 8236, CNRS, F-75013, Paris, France  
E-mail: chuanyu.dream@gmail.com

<sup>2</sup>Univ Paris Diderot, Sorbonne Paris Cité, MSC, UMR 7057, CNRS, F-75013, Paris, France  
E-mail: philippe.brunet@univ-paris-diderot.fr

### Introduction

Acoustic streaming was previously visualized around a sharp edge in a mixing micro-channel under piezoelectric transducer excitation at low frequency (2.5kHz). Maximum streaming velocities appear around the tip of the sharp structure and are measured under different vibration amplitudes and geometry structures. To gain deeper understanding of the experiment trend, numerical modelling using both Perturbation Theory (PT) and Direct solving of N-S equations (DNS) are conducted to investigate the characteristic of the streaming near the sharp structure at other conditions (low frequency, controllable curvature diameters etc.). This study aims to compare the two simulation methods with experimental results as reference[1].

### Theory Model

Decomposing the flow variables into two terms, with the first one represented by  $\mathbf{v}_\omega p_\omega$ , respectively vibration velocity and pressure (complex value ( $Re(\mathbf{v}_a e^{i\omega t})$ ) and  $p_\omega = Re(p_a e^{i\omega t})$ ), and the second one by  $\mathbf{v}_s p_s$  meaning steady streaming velocity and pressure, the momentum equation can be separated into two equations[2], respectively standing for the time-dependent terms at angular frequency  $\omega$ , and for the steady terms:

$$i\omega v_a + (\mathbf{v}_s \cdot \nabla)v_a + (\mathbf{v}_a \cdot \nabla)v_s = -\frac{1}{\rho}\nabla p_a + \nu\nabla^2 v_a \quad \text{Eq. 1}$$

$$((\mathbf{v}_s \cdot \nabla)v_s + \frac{1}{2}R[(\mathbf{v}_a \cdot \nabla)v_a^*]) = -\frac{1}{\rho}\nabla p_s + \nu\nabla^2 v_s \quad \text{Eq. 2}$$

The PT method assumes that the  $Re(\mathbf{v}_a) \gg v_s$  so that the inertial terms in the Eq. 1 can be considered negligible. Without the inertial terms, Eq. 1 and Eq. 2 become independent and can be solved to obtain  $v_a$  and  $v_s$  separately. In most acoustic streaming cases, the PT method remains valid. However, in case of higher acoustic streaming effects (especially locally near a sharp structure), the assumption by PT might fail since the terms  $Re(\mathbf{v}_a)$  and  $v_s$  becomes comparable in magnitude.

For DNS,  $\mathbf{v} = \mathbf{v}_a + \mathbf{v}_s$  as an ensemble variable to be solved from N-S equations with periodic boundary conditions. Then streaming velocity  $\mathbf{v}_s$  can be accessed by time integral of  $\mathbf{v}$ . Thus, the DNS is expected to better predict the streaming field. One of the inconveniences though is the heavy computing requirement since a transient resolution of the acoustic field is necessary.

### Geometry structure

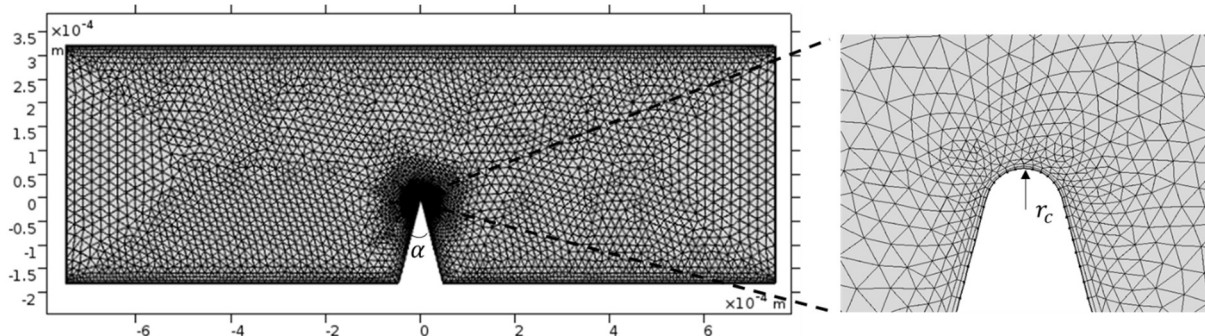
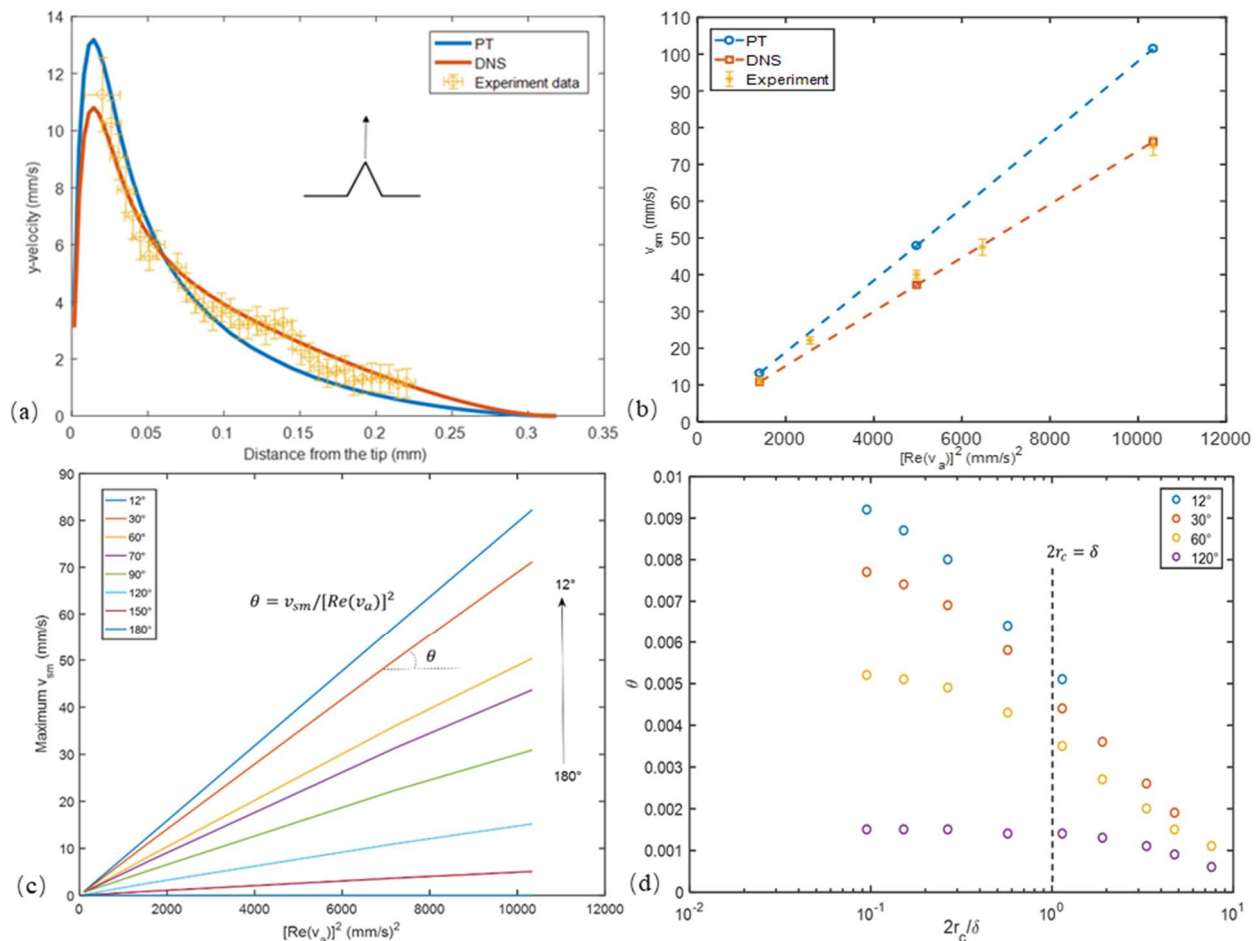


Fig 1 Sharp structure in the channel;  $\alpha$  means the tip angle of the sharp edge,  $2r_c$  means curvature diameter of the tip

As shown in Fig.1, the length, width of the channel is respectively 1.4mm and 0.5mm. The height of the sharp edge is 0.18mm. Different tip angles  $\alpha$  ( $15^\circ$ ,  $30^\circ$ ,  $45^\circ$ ,  $60^\circ$ ,  $80^\circ$ ,  $90^\circ$ ,  $120^\circ$ ) and curvature diameters  $2r_c$  (from  $1.2 \mu\text{m}$  to  $50 \mu\text{m}$ ) are investigated in our study and fixed independently to each other. For boundary conditions, the left and right sides of the channel are considered to have periodic horizontal velocity. Other sides are treated as non-slip walls.



**Fig 2** Comparison of maximum streaming velocity between experiment and simulation and its variations with different tip angle and curvature diameter (a) variation of  $v_{sm}$  with square of the amplitude of vibration velocity :  $\alpha = 30^\circ, 2r_c = 2.8 \mu m$  (b) variation of streaming velocity along y direction from the tip:  $\alpha = 30^\circ, 2r_c = 2.8 \mu m$  (c) relation between  $v_{sm}$  and  $[Re(v_a)]^2$  with different  $\alpha$ :  $2r_c = 2.8 \mu m$ ; (d) coefficient of linear relationship extracted from (c), with  $\delta = \sqrt{2\nu/\omega}$  is the acoustic boundary layer.

## Results and discussions

As shown in Fig.2, simulations corresponding to different tip angles and curvature diameters have been conducted. Fig.2(a) shows the streaming velocity reaches its maximum value near the boundary layer thickness along y direction and decreases quickly after the peak. Fig.2(b) shows that with a certain geometry structure,  $v_{sm}$  (it is the maximum streaming velocity value along y direction from the tip, which is referred to as a characteristic value of the streaming velocity field, shown as the peak values in Fig.2(a)) linearly varies with  $[Re(v_a)]^2$  (square of acoustic vibration amplitude).

In addition, it is obvious that, compared with classic PT method, results by direct solving of the N-S equations are closer to the experiment data, especially at higher vibration amplitude. As it has been mentioned, from Fig.2(b), we can see that when  $Re(v_a) = 101 \text{ mm/s}$ ,  $v_{sm}$  can reach  $69.5 \text{ mm/s}$ , which means the streaming velocity is comparable to vibration velocity and the inertia terms in Eq.1 can't be neglected.

Fig.2(c) demonstrates the effect of the tip angle  $\alpha$  on the gradient  $\theta$ , which is independent of the excitation conditions and characterizes the influence of the tip geometry on the streaming field. From Fig.2(c), with certain  $2r_c$ , smaller tip angle means larger gradient. Fig.2(d) shows the variations of  $\theta$  with  $2r_c/\delta$  (by changing  $2r_c$ ). Under the same vibration condition, streaming phenomenon is less obvious when  $2r_c/\delta$  becomes larger.

## Conclusion

Acoustic streaming phenomenon can be induced near a sharp structure, which is confirmed by experimental and numerical studies. In the local area near the tip where streaming velocity is comparable to vibration velocity, DNS can give a better prediction of streaming velocity field than the PT method. Geometries with smaller tip angle and curvature diameter offer larger  $\theta$ , which means stronger streaming under the same excited vibration conditions.

## References

- [1] C. Zhang, X. Guo, P. Brunet, M. Costalonga, L. Royon, Acoustic streaming near a sharp structure and its mixing performance characterization, (n.d.) 1–36. [under review]
- [2] M. Ovchinnikov, J. Zhou, S. Yalamanchili, Acoustic streaming of a sharp edge, J. Acoust. Soc. Am. 136 (2014) 22–29. doi:10.1121/1.4881919.



## Modeling of acoustic streaming in Al-PDMS acoustofluidic chips

William N. Bodé<sup>1</sup>, Henrik Bruus<sup>2</sup>

<sup>1</sup>Department of Physics, Technical University of Denmark, Kongens Lyngby, Denmark  
E-mail: [s141209@student.dtu.dk](mailto:s141209@student.dtu.dk), URL: <http://www.fysik.dtu.dk/microfluidics>

<sup>2</sup>Department of Physics, Technical University of Denmark, Kongens Lyngby, Denmark

### Introduction

We study numerically the acoustophoretic response in water-filled acoustically hard microchannels with acoustically soft lids. In particular, we focus on the rapid prototyping developed at Lund University, made by milling of the microchannels in the surface of an aluminum slab, and covered by a thin PDMS lid [1].

### Device design

The hard-wall-soft-lid acoustofluidic system is sketched in Fig. 1. It consists of a piezoelectric PZT transducer ( $20 \text{ mm} \times 5 \text{ mm} \times 1 \text{ mm}$ ) mounted underneath an aluminum base ( $60 \text{ mm} \times 5 \text{ mm} \times 0.4 \text{ mm}$ ). A microchannel ( $40 \text{ mm} \times 430 \text{ }\mu\text{m} \times 200 \text{ }\mu\text{m}$ ) is milled along the top center line of the base, and it is fully covered by a  $20\text{-}\mu\text{m}$  thick PDMS rubber lid. The PZT transducer is excited by an ac voltage in the MHz range with amplitude  $10 V_{pp}$  applied to its electrodes. To increase the coupling with the antisymmetric standing half-wave in the microchannel, the PZT transducer is displaced a distance  $\Delta \approx 1 \text{ mm}$  relative to the aluminum base.

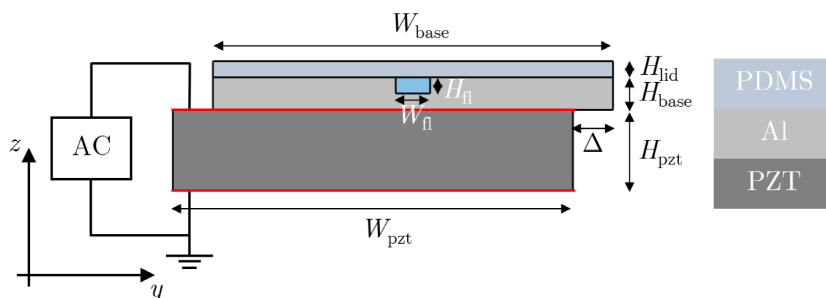


**Figure 1:** Sketch of the hard-wall-soft-lid aluminum-PDMS device showing the PZT transducer, the aluminum chip, and the PDMS lid. The electrodes of the PZT transducer are marked by the two red lines.

### Numerical simulations of the acoustofluidic system

Using the COMSOL Multiphysics implementation presented in Ref. [2], we set up a numerical model of the hard-wall-soft-lid device that includes the piezoelectricity of the PZT transducer, the solid mechanics of the aluminum base and the PDMS lid, the acoustics in the water including the viscous boundary layer, radiation force, and streaming. Eight resonance modes of the system was determined as the peaks in a plot of the acoustic energy density  $E_{ac}$  as a function of excitation frequency from 1.8 to 2.8 MHz. To determine the quality of a resonance mode, Moiseyenko and Bruus have in Ref. [3] introduced a figure of merit  $R$  as the ratio of the horizontal to vertical component of the average acoustic radiation force in the water domain. A large value of  $R$  means that the radiation force has a large horizontal and small vertical component, and is this close to the ideal standing half-wave mode. Among the eight resonance modes in the hard-wall-soft-lid device, the one at 2.246 MHz had the largest figure of merit,  $R = 1.1$ . This mode is shown in Fig. 2(a).

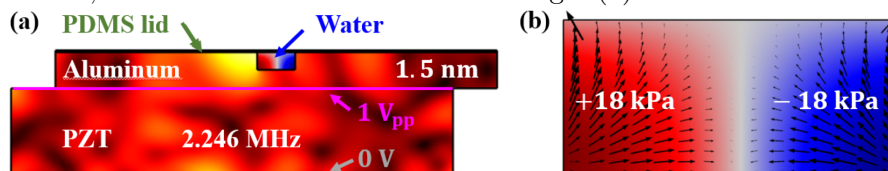


**Figure 2:** (a) Color plot of the displacement field from 0 (black) to 1.5 nm (white) in the hard-wall-soft-lid device at the 2.246 MHz resonance excited by a  $1 V_{pp}$  voltage applied to the PZT transducer. In the water channel is shown a color plot of the acoustic pressure from  $-18 \text{ kPa}$  (blue), through  $0 \text{ kPa}$  (gray) to  $+18 \text{ kPa}$  (red). (b) A zoom-in on the water channel showing the pressure (color plot) and radiation force (black arrows).

We note that the displacement field in both the PZT transducer and in the aluminum base appears rather random. Notably, the motion in the PZT is far from the idealized coherent vertical motion

that one normally associates with its fundamental excitation. Nevertheless, the acoustic pressure in the water channels appears almost symmetric around the center line, as in the conventional standing half-wave resonance, but it is not horizontal. As revealed by the figure of merit being close to unity, the vertical component is as big as the horizontal one, and the radiation force tends to push suspended particles inwards and upwards. This focusing pattern is qualitatively different from the conventional focusing-in-the-center-plane pattern of the standing half-wave.

### Hard-wall-soft-lid compared to hard-wall-hard-lid devices

In Fig. 3, we compare the hard-wall-soft-lid Al-PDMS device with a pure aluminum hard-wall-hard-lid system for the strongest resonance for the three different lid heights 400, 100, and 20  $\mu\text{m}$ . As the channel width is 430  $\mu\text{m}$ , the frequency of the ideal half-wave resonance is 1.74 MHz.

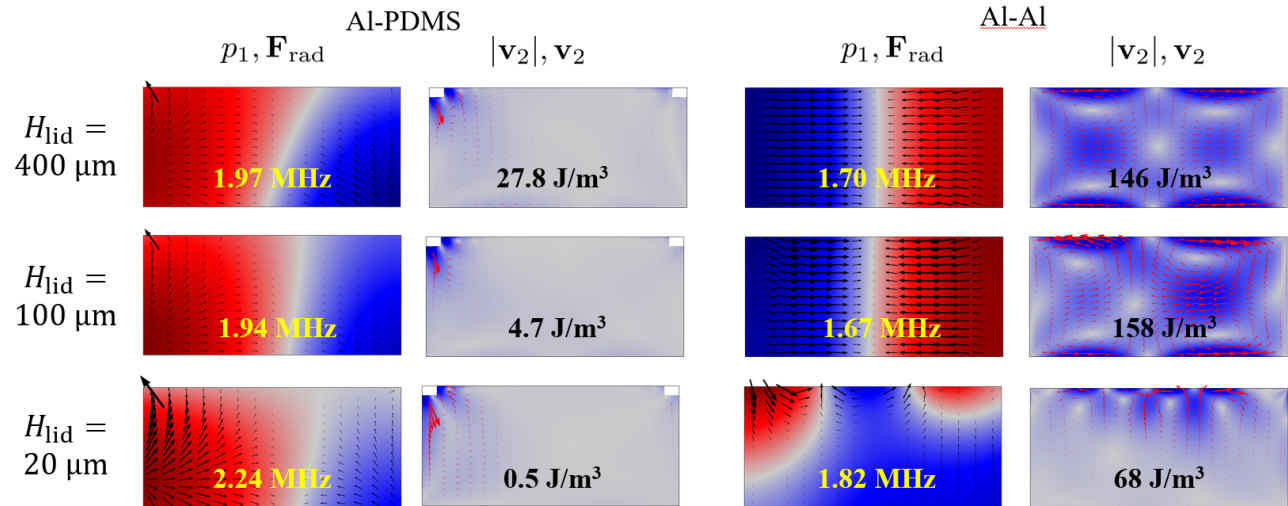


**Figure 3:** The two left-most columns: The pressure (red-gray-blue color plot), radiation force (black arrows), and streaming velocity (gray-blue color plot and red arrows for hard-wall-soft-lid Al-PDMS devices for the lid-heights 400, 100 and 20  $\mu\text{m}$ . The resonance frequency is shown in yellow, and the acoustic energy density in black. The two right-most columns: The same as before by for a pure aluminum hard-wall-hard-lid device.

The thick-lidded hard-wall-hard-lid device in the top-right corner of Fig. 3 behaves almost as an ideal halfwave device: The resonance frequency is 1.70 MHz, only 0.04 MHz below the ideal half-wave frequency, the nodal line of the pressure is along the vertical center line, the radiation force focuses towards this center line, and the streaming velocity exhibits the characteristic  $2 \times 2$  counter-flowing Rayleigh vortices that have been observed both theoretically and experimentally in conventional systems [4]. This situation persists as the lid is thinned down to 100  $\mu\text{m}$ , and only for the thinnest 20  $\mu\text{m}$  lid does the asymmetric actuation become visible in the pressure and streaming pattern. This behaviour is in stark contrast to the hard-wall-soft-lid device shown in the left-most two columns of Fig. 3. For all three lid thickness does the acoustic response appear asymmetric. In particular, only one strong and one weak vortex are visible in the streaming pattern. We also note that the acoustic energy density in the hard-wall-hard-lid device is typically one to two orders of magnitude larger than in the corresponding hard-wall-soft-lid device. It may be argued that the soft-lid suppresses the streaming, in the sense that only two of the expected four flow rolls appear. It is an obvious generalization to state that if one soft lid effectively removes half of streaming vortices, then a combination where both the lid and the floor are soft materials would remove all four flow rolls. The experimental and numerical results that we present in Ref. [1] do seem to support this prediction.

### Conclusion

Our numerical analysis of the hard-wall-soft-lid device reveals that the acoustic response in the water channel is weaker than in the conventional hard-wall-hard-lid device, and that it is more sensitive to the specific actuation method. All the resulting fields are asymmetric as a consequence of the asymmetric actuation. Our analysis also emphasize that a more systematic use of soft walls may lead enhanced control over the resulting streaming fields, and may even suppress the streaming altogether. A much more complete numerical and experimental study of soft walls is needed to fully understand the nature of streaming in such systems.

### References

- [1] L Jiang, W Qiu, WN Bodé, N Peng, A Lenshof, H Bruus, T Laurell, *Procs. Acoustofluidics 2019*, submitted (2019).
- [2] NR Skov, JS Bach, BG Winckelmann, and H Bruus, *AIMS Mathematics* **4**, 99-111 (2019).
- [3] RP Moiseyenko and H Bruus, *Phys Rev Appl* **11**, 014014 1-14 (2019).
- [4] PB Muller, M Rossi, AG Marin, R Barnkob, P Augustsson, T Laurell, CJ Kähler, H Bruus, *Phys Rev E* **88**, 023006 (2013).



# The role of device properties in thermoacoustic heating

Jonas H. Jørgensen and Henrik Bruus

Department of Physics, Technical University of Denmark, Kongens Lyngby, Denmark  
E-mail: [jonashj@fysik.dtu.dk](mailto:jonashj@fysik.dtu.dk), URL: <http://www.fysik.dtu.dk/microfluidics>

## Introduction

Temperature variations in acoustofluidic devices are often not measured, and in many cases drift or fluctuations in the temperature is suppressed by controlled cooling. However, if it can be controlled, the temperature might play a more active role in acoustofluidics. The first step in this direction would of course be to monitor the local temperature in the device, and as been done recently by Ohlin *et al.* [1] in an acoustofluidic glass chip with embedded electrodes acting as heaters and thermometers. This work has inspired us to begin a theoretical study of acoustofluidic devices.

Here, we study numerically the heating induced by the acoustic field in the fluid inside an acoustofluidic device run at the usual standing half-wave resonance. The starting point for our analysis is the work by Muller and Bruus [2], which however included only the fluid domain. We extend their model by including the thermal properties of the surrounding solid. For a typical acoustic energy density of 20 Pa, the acoustic field increase the temperature of the water by 0.17 mK, when the channel walls are kept fixed at the ambient temperature. When part of the boundary is replaced by thermal insulators, the temperature increases three orders of magnitude to 150 mK. We show that silicon walls may be used to keep the wall temperature constant, while glass behaves more like an thermal insulator, albeit imperfectly. The heat is shown to flow from the oscillating walls, where the local temperature drops, to the stationary walls, where the temperature is increased.

## Model and governing equations

Applying thermoacoustic perturbation theory as in Ref. [2], we find that the relevant field to study, is the second-order time-average temperature field  $T_2(\mathbf{r})$  which may contribute to a (quasi-)steady temperature change, whereas the harmonically oscillating first-order temperature field  $T_1$  averages to zero. In terms of the first-order pressure  $p_1$ , density  $\rho_1$ , velocity  $\mathbf{v}_1$ , and temperature  $T_1$ , the governing equations for the corresponding second-order fields (with subscript 2) time-averaged over one oscillation period (angled brackets) is,

$$\nabla \cdot [\rho_0 \mathbf{v}_2 + \langle \rho_1 \mathbf{v}_1 \rangle] = 0, \quad (1a)$$

$$\nabla \cdot [\boldsymbol{\tau}_2 - p_2 \mathbf{1} - \rho_0 \langle \mathbf{v}_1 \mathbf{v}_1 \rangle] = \mathbf{0}, \quad (1b)$$

$$\nabla \cdot \left[ \langle \mathbf{v}_1 \cdot \boldsymbol{\tau}_1 \rangle + k_0^{\text{th}} \nabla T_2 + \langle k_1^{\text{th}} \nabla T_1 \rangle - p_0 \mathbf{v}_2 - \langle p_1 \mathbf{v}_1 \rangle - \rho_0 T_0 \langle s_1 \mathbf{v}_1 \rangle - \frac{p_0}{\rho_0} \langle \rho_1 \mathbf{v}_1 \rangle \right] = 0, \quad (1c)$$

$$\boldsymbol{\tau}_2 = \eta_0 \left[ \nabla \mathbf{v}_2 + (\nabla \mathbf{v}_2)^{\text{T}} \right] + \left[ \eta_0^{\text{b}} - \frac{2}{3} \eta_0 \right] (\nabla \cdot \mathbf{v}_2) \mathbf{1} + \left\langle \eta_1 \left[ \nabla \mathbf{v}_1 + (\nabla \mathbf{v}_1)^{\text{T}} \right] \right\rangle + \left\langle \left[ \eta_1^{\text{b}} - \frac{2}{3} \eta_1 \right] (\nabla \cdot \mathbf{v}_1) \mathbf{1} \right\rangle. \quad (1d)$$

Here,  $\boldsymbol{\tau}_2$  is the stress tensor given in terms of the dynamic viscosity  $\eta = \eta_0 + \eta_1(T)$  and the bulk viscosity  $\eta^{\text{b}} = \eta_0^{\text{b}} + \eta_1^{\text{b}}(T)$ . Using the COMSOL Multiphysics implementation presented in Ref. [1], We reproduce in Fig. 1(a) their result for a  $400 \mu\text{m} \times 150 \mu\text{m}$  idealized hard-wall water domain with fixed temperature on all four walls (dark green). The arrows (cyan) represent the heat flux  $J_2$ . (b) The same as in panel (a) except the thermal boundary condition on the horizontal top and bottom walls (purple) are perfect insulators with zero normal heat flux,  $\mathbf{n} \cdot \mathbf{J} = 0$ , and as a result  $T_2$  is now between 0 (gray) to 151 mK (red). The vertical side walls of the water domain oscillate at the horizontal half-wave resonance frequency 1.967 MHz as in Ref. [2].

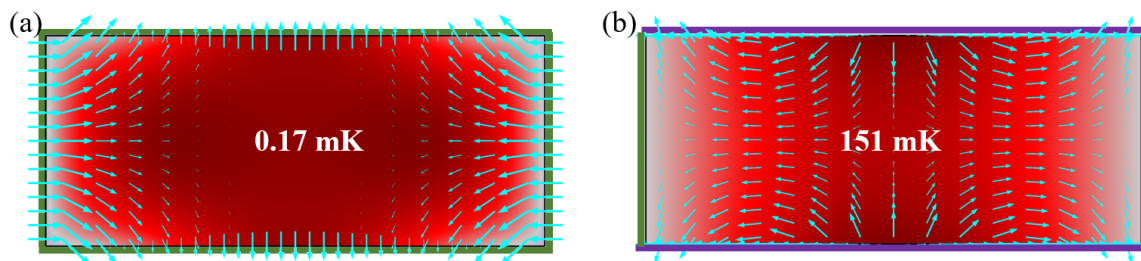


**Figure 1:** (a) Symmetrized color plot from negative (blue), over zero (gray), to positive (red) of the time-averaged temperature change  $T_2$  from  $-0.02$  (gray) to  $0.17$  mK (red) in the hard-walled water domain with side walls oscillating at  $1.97$  MHz and stationary top and bottom walls, while the temperature is fixed to be  $T = 25$  °C on all four walls (dark green). The arrows (cyan) represent the heat flux  $J_2$ . (b) The same as in panel (a) except the thermal boundary condition on the horizontal top and bottom walls (purple) are perfect insulators with zero normal heat flux,  $\mathbf{n} \cdot \mathbf{J} = 0$ , and as a result  $T_2$  is now between  $0$  (gray) to  $151$  mK (red). The vertical side walls of the water domain oscillate at the horizontal half-wave resonance frequency  $1.967$  MHz as in Ref. [2].

We see how in the case of isothermal walls, the temperature change is minute, namely 0.17 mK as noted by Muller and Bruus [2]. Interestingly, the addition of thermally insulating walls raises the temperature change by three orders of magnitude to 151 mK.

### Adding heat-conducting solid walls

To investigate how close to the ideal setup in Fig. 1 we can come in experiment, we add 500  $\mu\text{m}$ -thick heat-conducting solid walls around the water domain. As materials we use Pyrex as in the experiments in Ref. [1], and a Pyrex-silicon-Pyrex layered structure as in Ref. [3]. For water, Pyrex, and silicon, the heat conductivity  $k_{\text{th}}$  is  $k_{\text{th}}^{\text{wa}} = 0.61 \text{ W}/(\text{Km})$ ,  $k_{\text{th}}^{\text{py}} = 1.14 \text{ W}/(\text{Km})$ , and  $k_{\text{th}}^{\text{si}} = 149 \text{ W}/(\text{Km})$ , while the thermal diffusivity  $D_{\text{th}}$  is  $D_{\text{th}}^{\text{wa}} = 1.45 \times 10^{-7} \text{ m}^2/\text{s}$ ,  $D_{\text{th}}^{\text{py}} = 6.34 \times 10^{-7} \text{ m}^2/\text{s}$ , and  $D_{\text{th}}^{\text{si}} = 8.35 \times 10^{-5} \text{ m}^2/\text{s}$ . Compared to water, silicon appears an almost perfect heat conductor with its 100-times bigger thermal coefficients. In contrast, Pyrex is similar to water and thus appears as a (rather poor) thermal insulator. The resulting simulation results for  $T_2$  is shown in Fig. 2 for various combinations of solids and heat-insulating/isothermal boundary conditions on the outer walls, while the vertical side walls of the water channels are oscillating as in Fig. 1.

For the pure Pyrex-system in Figs. 2(a) and 2(b), we note three aspects: (1) The oscillating side walls of the water domain are cooled as heat is transported towards the top and bottom of the center of the channel. (2) The temperature rise of 33 mK is 200 times that of Fig. 1(a) and only 5 times lower than that of Fig. 1(b). In this sense, Pyrex acts as an (imperfect) thermal insulator. The change of the outer boundary conditions from Figs. 2(a) to 2(b) has only a minor effect, but clearly outside the water domain, the 0-isothermal line for  $T_2$  is bending away from the insulating top and bottom wall.

The thermal field in the pure silicon-system in Fig. 2(c) has the same appearance the Pyrex system Fig. 2(a), but the amplitude of 0.5 mK is 70 times smaller, and very close to the ideal isothermal-boundary case of Fig. 1(a). In this sense, silicon appears as a nearly perfect heat conductor. This point is further emphasized by the layered Si-Pyrex-Si structure of Ref. [3] used in Fig. 2(d). The silicon layer (almost) keeps the fixed boundary temperature, while the Pyrex heats up almost as in Figs. 2(a) and (b).

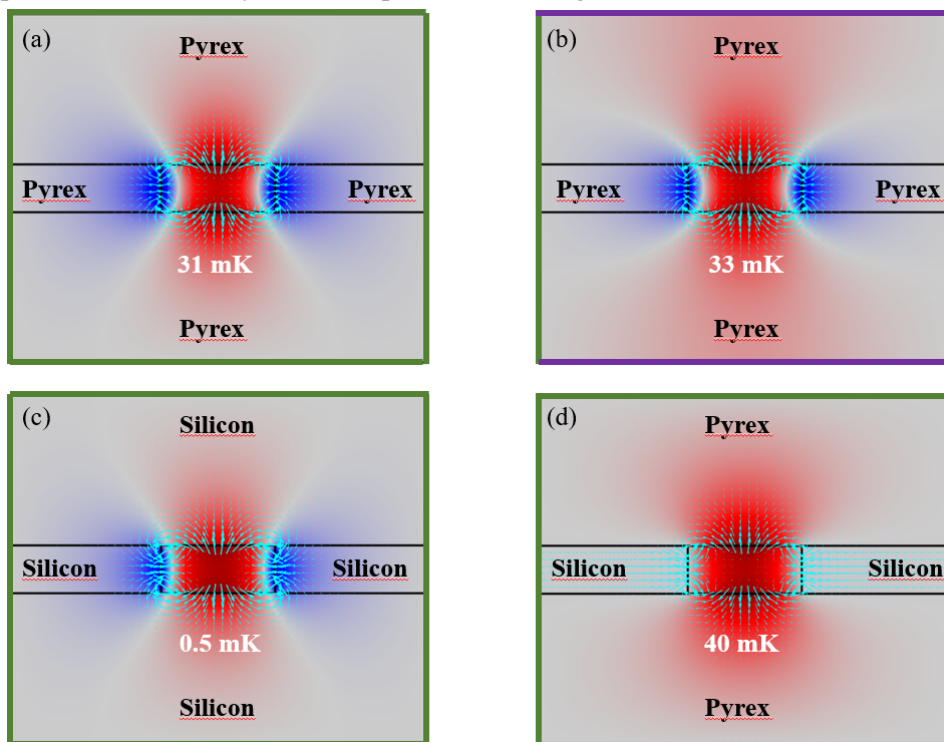


**Figure 2:** (a) A pure Pyrex system with isothermal (dark green) boundary conditions. (b) Same as in (a), but with the top and bottom walls now being ideal thermal insulators (purple). (c) A pure silicon system with isothermal (dark green) boundary conditions. A layered Si-Pyrex-Si system with isothermal (dark green) boundary conditions. The vertical side walls of the water domain oscillate at the horizontal half-wave resonance frequency 1.967 MHz as in Ref. [2].

### Conclusion

Our numerical analysis show the possibilities of shaping the thermal fields in acoustofluidics by choosing the proper materials surrounding the water domain. We also note that in the case of partially insulating Pyrex walls, the temperature rise in a typical acoustofluidic case is as high as 40 mK, which is 200 times higher than the idealized estimate given in Ref. [2], and which thus may give rise to interesting thermoacoustic effects.

### References

- [1] M Ohlin, M Andersson, L Klintberg, K Hjort, M Tenje, *Procs. Acoustofluidics 2017, San Diego*, p. 70-71 (2017).
- [2] PB Muller and H Bruus, *Phys Rev E* **90**, 043016 1-12 (2014).
- [3] R Barnkob, I Iranmanesh, M Wiklund, and H Bruus. *Lab Chip* **12**, 2337-2344 (2012).



## Motility and aerotaxis in *Sinorhizobium meliloti*, a soil bacterium

Julien Bouvard<sup>1</sup>, Harold Auradou<sup>1</sup>, and Frédéric Moisy<sup>1</sup>

<sup>1</sup>Laboratoire FAST, Université Paris-Sud, CNRS, Université Paris-Saclay, Paris, France  
E-mail: [julien.bouvard@u-psud.fr](mailto:julien.bouvard@u-psud.fr), URL: <http://www.fast.u-psud.fr/~bouvard/>

### Introduction

Chemotaxis, the biased migration of a motile cell towards the source of a chemical gradient, is an ubiquitous phenomenon in nature. Yet, our understanding of the basic physical (and more specifically hydrodynamical) mechanisms behind the chemotaxis of swimming cells in a liquid environment is still limited. Here, we are interested in the chemotaxis of a motile nitrogen-fixing bacterium naturally presents in the soil, *Sinorhizobium meliloti*, which forms a symbiosis with some legume plants such as Alfalfa [1]. Although the infection itself is well documented, the fluid dynamics of the pre-infection approach phase, when bacteria swim towards the root in a water-saturated soil, is still an open problem. Among various chemoattractants, aerobic bacteria (including *S. meliloti*) are sensitive to the oxygen content of the medium - a specific chemotaxis referred to as aerotaxis. Most previous experiments based on chemotactic/aerotactic assays for *S. meliloti* are qualitative [2], and cannot characterise in detail the biased swimming towards the chemoattractant and the possible existence of chemokinesis [3]. We address here this problem using microfluidics and image processing methods. We designed two experiments to quantitatively characterise aerotaxis: a simple one with unstationary oxygen gradient, and a second one using a microfluidic device with stationary oxygen gradient.

### Methods

*S. meliloti* are grown in liquid culture media, showing a doubling time  $t_{1/2}$  of 2.3 h at 28 °C in rich media such as Yeb and Ty [4]. Under usual conditions, *S. meliloti* population is composed of both non-motile and motile bacteria with a mean velocity ranging from 0 to 60  $\mu\text{m s}^{-1}$ . Bacteria motion is observed using high-speed imaging under phase-contrast or bright-field microscopy, and their trajectories are analysed using *ImageJ* with the *TrackMate* plug-in.

A preliminary experiment is designed to determine the dioxygen consumption rate of motile *S. meliloti*: We observe the evolution of the motility of a small volume of bacteria suspension enclosed in a sealed chamber. After a certain time, we observe a sharp decay of motility, starting from the center of the chamber and reaching the edge. From this extinction time  $t_{ext}$  measured for various bacteria concentration  $c_{bact}$ , we determine the consumption rate  $k$  of dioxygen assuming  $\partial c_{O_2}/\partial t = -kc_{bact}$ : we have  $t_{ext} = \beta/c_{bact}$  where  $\beta = s_{O_2}N_A/(kM_{O_2})$ , with  $N_A$  the Avogadro number,  $M_{O_2}$  the molar mass of dioxygen, and  $s_{O_2}$  the solubility of dioxygen in water. Our data give  $k \simeq (4.5 \pm 1) \times 10^4$  dioxygen molecules per bacterium per second, a value close to *E. coli* [5].

### Aerotaxis near an air bubble

A first experiment is designed to illustrate the aerotactic behaviour of *S. meliloti*. We trap an air bubble in the middle of a sealed chamber filled with bacteria suspension, and measure the spatial distribution of motile and non-motile bacteria around the bubble (Fig. 1). The concentration of motile bacteria decreases with the distance from the air bubble, reaching zero at a distance of  $\simeq 800 \mu\text{m}$ , whereas the concentration of non-motile bacteria remains constant. Interestingly, the mean velocity of the bacteria remains nearly constant, at least not too far from the bubble, in spite of the change in bacteria concentration (and hence oxygen concentration). This clearly shows that an aerotactic flux takes place towards the bubble, characterized by a nearly constant velocity but a biased orientation process towards the source of oxygen.

### Aerotactic band in a microfluidic channel

A drawback of the previous experiment is the non-stationary oxygen concentration in the bubble. We therefore developed a second experiment with steady boundary conditions in a microfluidic device. This device, based on Cheng *et al.* [6], is composed of three channels machined in plexiglass, an air-proof material, put on an agar layer itself stuck on a glass slide. The middle channel is filled with a bacterial suspension of *S. meliloti*, and water (containing soluble oxygen) is flowed from right to left in the two external channels at a fixed flowrate. Oxygen diffuses from the lateral channels into the central channel containing the bacteria through the agar layer. A strong accumulation of motile bacteria is observed at the right end of the central channel, forming a well defined band of width  $\simeq 200 \mu\text{m}$  (Fig. 2). The band is localised close to the maximum supply of fresh oxygen from the lateral channels. This band is formed only at large overall bacteria concentration, when an oxygen gradient along the channel is generated from the balance between the oxygen consumption by bacteria and the

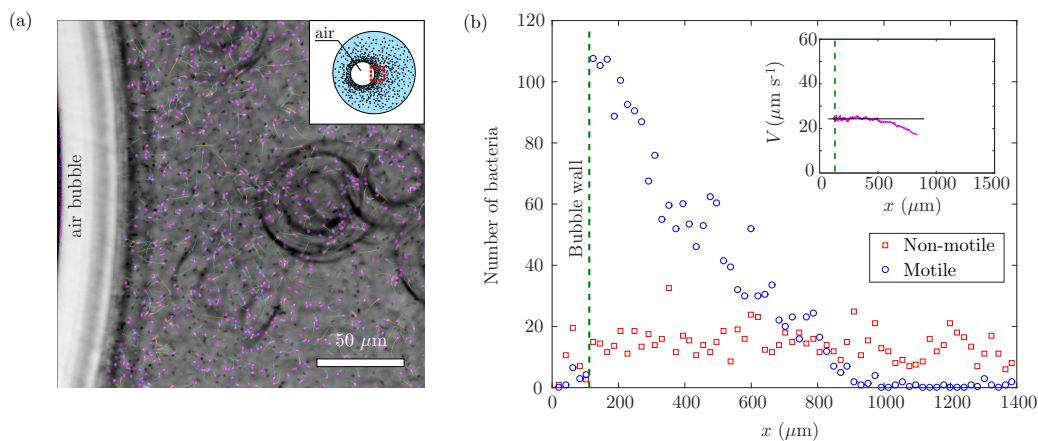


**Figure 1** – (a) Bacteria trajectories around an air bubble trapped in a sealed chamber (63X magnification). Each pink spot is a detected bacteria and the color of the tracks corresponds to its mean horizontal velocity  $V$  (blue being 0 and red  $55 \mu\text{m s}^{-1}$ ). (b) Number of bacteria as a function of the distance from the air interface. Motile and non-motile bacteria are discriminated using a threshold of  $V = 6 \mu\text{m s}^{-1}$ . The inset shows the mean bacteria velocity  $V$  as a function of  $x$ .

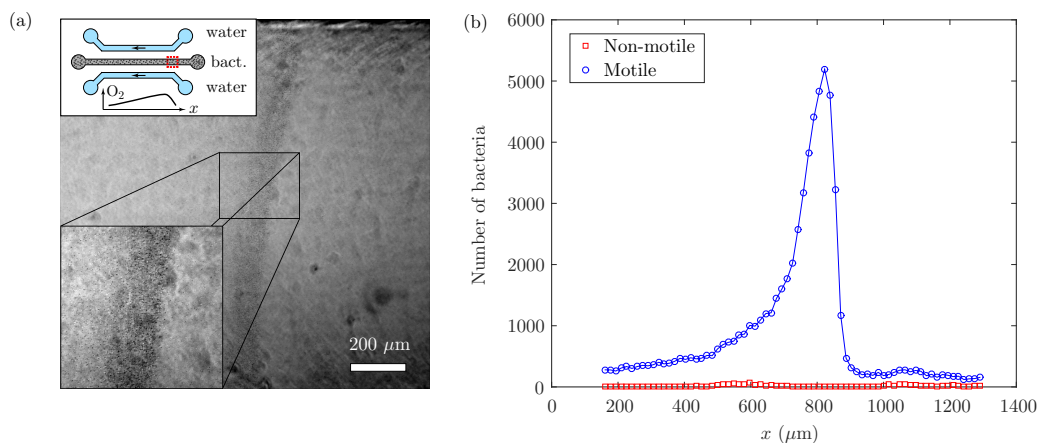


**Figure 2** – (a) Formation of a bacteria band in the middle channel of the microfluidic device sketched in the inset (10X magnification). Bacteria accumulate at the end of the channel, where oxygen diffusion from the upper and lower channel is maximum. (b) Number of bacteria as a function of  $x$ .

oxygen supply from the lateral channels. The concentration profile is very similar to the one observed by Saragosti *et al.* [7] with *E. coli*. Once this band is created, it can be moved towards or away from one of the channels by varying the flowrates, with a typical latency time of 10 min.

## Conclusion

The microfluidic device designed here to characterise aerotaxis in *S. meliloti* has a great potential for quantitative investigation of chemotaxis/aerotaxis in motile bacteria. From the main properties of the band (concentration, width), it is possible to determine the chemotactic/aerotactic flux and its dependence with chemical concentration and other biologically relevant parameters.

## Acknowledgements

We are grateful to N. Buset and P. Mergaert for providing the bacterial strain and helping in culture preparations. This work was supported by the LabeX PALM, project "Symbiose".

## References

- [1] J. Raina, V. Fernandez, B. Lambert, R. Stocker and J. Seymour. Nat. Rev. Microbiol. **17**, 284-294 (2019)
- [2] R. Götz, N. Limmer, K. Ober and R. Schmitt. Microbiology, **128**(4), 789-798 (1982)
- [3] I. B. Zhulin, A. F. Lois, B. L. Taylor. FEBS letters, **367**(2), 180-182 (1995)
- [4] X. Dai, Z. Shen, Y. Wang and M. Zhu. mSphere **3**(6), e00567-18 (2018)
- [5] C. Douarche, A. Buguin, H. Salman and A. Libchaber. Physical Review Letters **102**, 198101 (2009)
- [6] S. Cheng, S. Heilman, M. Wasserman, S. Archer, M. Shuler and M. Wu. Lab on a Chip, **7**(6), 763-769 (2007)
- [7] J. Saragosti, V. Calvez, N. Bournaveas, B. Perthame, A. Buguin and P. Silberzan. Proceedings of the National Academy of Sciences, **108**(39), 16235-16240 (2011)



# Nucleation of Plasmonic Bubbles in Binary Liquids; the role of Dissolved Gas and Latent Heat of Vaporization

Marvin Detert<sup>1,2</sup>, Binglin Zeng<sup>1,3</sup>, Yuliang Wang<sup>3</sup>, Harold J. W. Zandvliet<sup>2</sup> and Detlef Lohse<sup>1</sup>

<sup>1</sup>Physics of Fluids, University of Twente, Enschede, The Netherlands

E-mail: m.w.detert@utwente.nl

<sup>2</sup>Physics of Interfaces and Nanomaterials, University of Twente, Enschede, The Netherlands

<sup>3</sup>Robotics Institute, School of Mechanical Engineering and Automation, Beihang University, Beijing, P.R. China

## Introduction

When a noble metal nanoparticle or film is immersed in a liquid and irradiated with a laser, it heats rapidly and a vapor bubble nucleates. Consequently, bubbles generated this way are called plasmonic bubbles. They have garnered a lot of attention in recent years, in particular due to their variety of applications. These range from more effective solar harvesting, over pumps on microfluidic chips to drug delivery to a single cell [1-4].

However, the nucleation and growth of these bubbles are not completely understood yet. In fact, Wang et al. discovered in 2018 the nucleation of an initial giant vapor bubble via ultrahigh-speed imaging [5]. While they have shown that the dissolved gas influences the time of nucleation, the role of other parameters has not been investigated. Therefore, we want to disentangle the various parameters, such as boiling temperature, heat conductivity, latent heat of vaporization etc., with further measurements. A perfect candidate for measurements are binary liquids, because their parameters can be tuned by their composition.

## Delayed Nucleation

We have investigated the time between the onset of laser irradiation and the bubble nucleation for various binary liquids and laser powers  $P$ . We call the time by which the nucleation is delayed delay time  $\tau$ . The mixtures used are water with ethanol, acetone or 1-propanol and ethanol with acetone, 2-propanol or 1-butanol. For the mixtures with water, we observe a decrease in delay time with decreasing water concentration regardless of the organic liquid chosen. In contrast, for the mixtures with ethanol, the change in delay time depends on the second organic liquid. Increasing the acetone concentration reduces the delay time, increasing the 2-propanol concentration does not affect the delay time significantly and increasing the 1-butanol concentration increases the delay time. If we assume that all liquids are saturated with gas in the beginning and mix ideally then this can be explained by the amount of dissolved gas in the liquid. The solubility of nitrogen and oxygen is an order of magnitude smaller in water compared to the organic liquids. While the solubilities in ethanol are almost identical to 2-propanol, the ones in acetone are higher and the ones in 1-butanol lower. Hence, in Fig. 1 the delay time of the binary liquids is shown as a function of the dissolved gas for various laser powers. In each case the relation between the delay time and the gas concentration fits well to a power law and the exponent seems to increase linearly with the laser power.

The reduction in delay time with increasing amount of gas is probably caused by a reduction in the nucleation temperature. For  $\text{CO}_2$  in organic liquids Mori et al. have shown that the dissolved gas reduces the nucleation temperature [6]. To find the nucleation temperature in our experiment, we fit the data with a temperature field gained by the Fourier equation for heat conduction [5]. In the water cases the nucleation temperature decreases with decreasing water concentration. However, for the organic liquids the change in nucleation temperature is not very pronounced, which might be due to the smaller differences in solubilities. The dissolved gas could act as a nucleation site and thereby facilitate nucleation, which in turn would reduce the necessary temperature [5].

## Bubble Volume

Another aspect we investigated was the maximum volume of the initial bubble. Because the bubble volume depends on the available energy, it is treated as a function of the energy deposited by the laser  $E_d = P \cdot \tau$  [5,7]. We observe that the maximum volume of the bubble is similar for water, ethanol and 2-propanol at a given laser power. However, the volume is larger for acetone, smaller for 1-propanol and the smallest for 1-butanol. Comparing this with the latent heat of vaporization ( $H_{vap}$ ) at boiling we see that the volume seems to be inversely proportional to  $H_{vap}$ . If we assume the ideal gas law to determine the heat necessary to form a bubble, we find indeed that the volume should be inversely proportional to  $H_{vap}$  for a given energy [5,7].

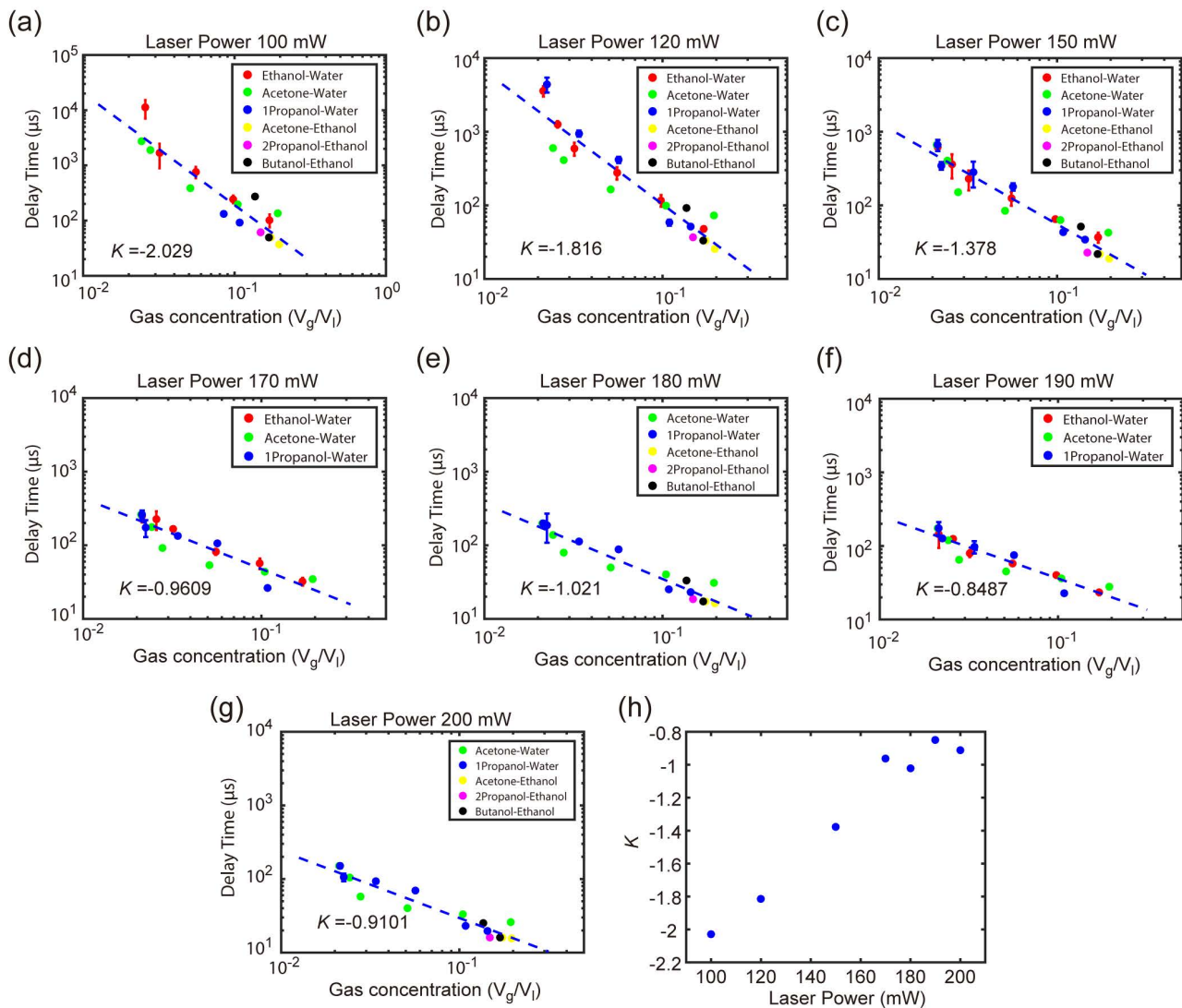


**Figure 1:** a) - g) Delay time as a function of the amount of dissolved gas in the mixtures for various laser powers from 100 mW to 200 mW. The dashed blue line represent a power law fit with the exponent  $K$ . h) Shows these exponents as a function of the laser power.

## Conclusion

We have shown that the delay time for the nucleation of a plasmonic bubble is not only influenced but dominated by the amount of dissolved gas present in the liquid. In contrast, the volume of the bubble does not appear to depend on the dissolved gas and instead depends mainly on the latent heat of vaporization of the liquid. We are looking forward to presenting our results at the summer school *Complex Motion in Fluids 2019*.

## References

- [1] Y. Xie and C. Zhao. *Nanoscale* **9**, 6622-6631 (2017).
- [2] O. Neumann, A.S. Urban, J. Day, S. Lal, P. Nordlander and N.J. Halas. *ACS Nano* **7**, 42-49 (2013).
- [3] K. Zhang, A. Jian, X. Zhang, Y. Wang, Z. Li and H. Tam. *Lab Chip* **11**, 1389-1395 (2011).
- [4] Q. Fan, W. Hu and A.T. Ohta. *Lab Chip* **14**, 1572-1578 (2014).
- [5] Y. Wang, M.E. Zaytsev, G. Lajoinie, H.L. The, J.C.T. Eijkel, A. van den Berg, M. Versluis, B.M. Weckhuysen, X. Zhang, H.J.W. Zandvliet and D. Lohse. *PNAS* **115**, 7676-7681 (2018).
- [6] Y. Mori, K. Hijikata and T. Nagatani. *Int. J. Heat Mass Transf.* **19**, 1153-1159 (1976).
- [7] M.E. Zaytsev, G. Lajoinie, Y. Wang, D. Lohse, H.J.W. Zandvliet and X. Zhang. *J. Phys. Chem. C.* **122**, 28375-28381 (2018).



# Numerical study of evaporating sessile droplets and corrosion

C. Lalanne<sup>1,2</sup>, J.M. Fullana<sup>1</sup>, and F. Lequien<sup>2</sup>

<sup>1</sup>Sorbonne Université, CNRS, UMR 7190, Institut Jean Le Rond d'Alembert, Paris, France  
E-mail: cecile.lalanne@dalembert.upmc.fr

<sup>2</sup>Den-SERVICE de la Corrosion et du Comportement des Matériaux dans leur Environnement (SCCME), CEA, Université Paris-Saclay, F-91191 Gif-sur-Yvette, France

## Introduction

In France, some of nuclear wastes are packaged in stainless steel containers and stored in above-ground storage facilities. These waste packages are likely to remain in interim storage for a period of several decades before being moved to an underground facility for permanent disposal. During the interim period of storage, atmospheric aerosols will deposit on the container surfaces, in particular in marine atmosphere, where sprayed droplets are carried by the wind from the sea. The droplet deposits on the exposed surface and becomes saline sessile droplet. This creates an electrolyte of finite size that can react with the metallic surface, leading to an atmospheric corrosion phenomenon. Moreover, the day/night cycles induce a variation of the relative humidity and the temperature: this leads to a constant repetition of evaporation and condensation phases which can increase the corrosion phenomena [1].

The aim of the study is to develop a numerical analysis of the corrosion under droplet, so as to accurately predict its impact on the lifetime of the materials. Because of the complexity of the problem, the model is developed step by step. At first we are interested in the evaporation of sessile droplets of pure water deposited on non-corrodable substrat in order to understand the dynamics of evaporation on a simple case. Then, we will propose a numerical model of evaporation dynamics of salty sessile drops, built with Basilisk, a free software [2].

## Evaporation and fluid dynamics of a sessile drop

A droplet deposited onto a solid substrate has axial symmetry [3]. Due to minimum surface energy, the droplet usually takes spherical shape with a contact angle,  $\theta$ .

We consider here a sessile droplet surrounded by an atmospheric environment (Figure 1). In the numerical simulations, the relative humidity varies between 0 and 80% and the temperature is around 23 °C. Therefore, three different phases are present : liquid, solid and vapor. The intersection of the three interfaces, at the edge of the droplet, is called the Triple Contact Line (TCL).

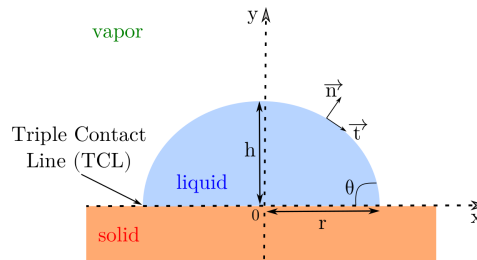


**Figure 1:** Sessile droplet with a radius  $r$ , a height  $h$  and a contact angle  $\theta$ .

The evaporation of a sessile droplet involves various evaporation modes [4-6] which may succeed one another: the constant radius mode, where the TCL is pinned to the substrate and the drop radius remains constant whereas the contact angle decreases; the constant contact angle mode where the radius decreases as the TCL is moving; finally, a third mode called "stick and slide", usually short as the radius and contact angle are varying simultaneously.

In the case of a sessile droplet, the evaporation flux at the interface,  $J$ , is non-uniform because of the presence of the substrat (except for hemispherical cases): the flux is then more important at the TCL. It is generally considered that the non-uniformity of  $J$  has no influence on the ambient air and that the air velocity is zero. Thus, the droplet evaporation can be totally modeled by the following pure diffusion equation of water vapor in air phase:

$$\frac{\partial c}{\partial t} = D\Delta c \quad (1)$$

where  $D$  is the vapor diffusivity and  $c$  is the local water vapor mass concentration.

This approach has been implemented using a software called Basilisk [7]: it allows to solve partial differential equations with finite volume methods. The diffusion equation is discretized on an adaptative mesh (Figure 2) and a VOF (Volume-Of-Fluid) method is implemented to track the droplet interface [8]. A function evaluates the local gradient of the diffusive tracer, the vapor here, in order to compute the phase change velocity. In this first study case, the droplet is deposited on a non-corrodable substrate. This pure diffusive method and the mesh level used to discretized our equations have been validated through the comparison of the radius evolution (Figure 2) with the following theoretical law (so-called  $d^2$  law [9]) depending on the level mesh refinement:

$$r^2(t) = r_0 - 2 \frac{D(c_0 - c_\infty)}{\rho} t \quad (2)$$

with  $r_0$ , the initial radius,  $c_0$  and  $c_\infty$  the vapor concentration at the interface and far from the droplet,  $\rho$ , the density and  $t$ , the time.

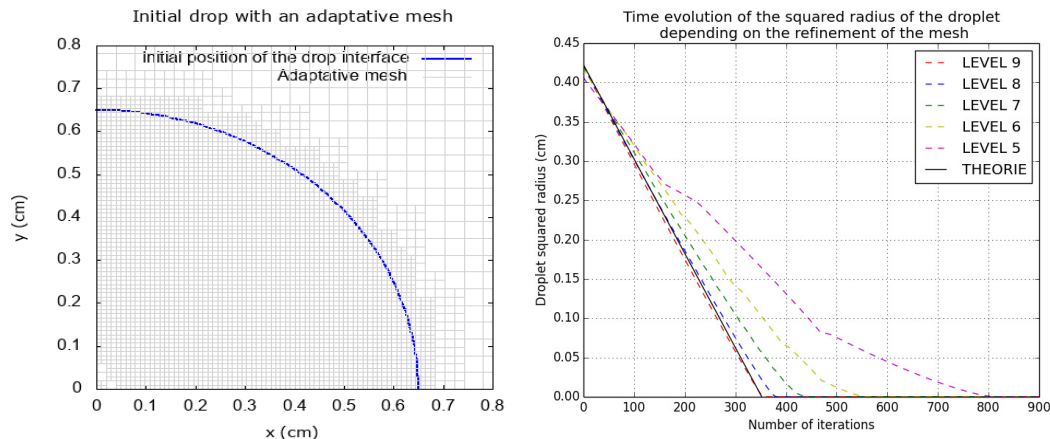


**Figure 2:** Test case of a pure water sessile droplet ( $r=6.5\text{mm}$ ;  $\theta=90^\circ$  with a relative humidity of 40% at ambient temperature). *On the left* : Adaptive mesh. *On the right* :  $d^2$  law depending on the mesh level.

### Influence of the non-uniformity of the evaporation flux

In this work, we considered that the non-uniformity of  $J$  can have an influence on the ambient air and that the air velocity,  $u$ , is not zero. In this way, a convective term has to be added in the pure diffusion equation (1) for the water vapor:

$$\frac{\partial c}{\partial t} + u \nabla c = D \Delta c \quad (3)$$

Navier-Stokes equations are also added in both phases. Air currents can have an influence on the droplet interface, mainly near the TCL.

### Conclusion

This work is still in progress, results about the different flow mechanisms inside and outside the droplet are expected. Because of the non-uniformity of  $J$  along the droplet interface, a capillary flow from the center of the drop to the TCL will be set up in order to balance the important loss of liquid at the TCL [10]. The capillary flow maintains the spherical shape of the droplet. Then, in a second step, saline sessile droplets will be studied. A transport equation for the salt concentration will be added in the liquid phase in order to identify the sites of salt deposits and then the potential sites of corrosion appearance. In this case, the Marangoni flow will be studied.

### References

- [1] R.D. Deegan et al. Nature **389**, 827-829 (1997).
- [2] S. Popinet. Journal of Computational Physics **228**, 5838-5866. (2009).
- [3] H. Hu. Langmuir **21(9)**, 3972-3980 (2005).
- [4] D. Zang. Physics Reports **804**, 1-56 (2019).
- [5] R.G. Picknett and R. Bexon. Journal of Colloid and Interface Science **61(2)**, 336-350 (1977).
- [6] A. Amini and G M. Homsy. Physical Review Fluids **2(4)**, (2017).
- [7] <http://basilisk.fr/>
- [8] S. Popinet and S. Zaleski. International Journal for Numerical Methods in Fluids **30(6)**, 775-793 (1999).
- [9] G.A.E. Godsave. Symposium (International) on Combustion **4(1)**, 818-830 (1953).
- [10] F. Boulogne et al. Journal of Physics : Condensed Matter **29(7)**, (2017).



## Evaporation of dilute sodium dodecyl sulfate droplets on a hydrophobic substrate

Wojciech Kwieciński<sup>1</sup>, Tim Segers<sup>2</sup>, Sjoerd van der Werf<sup>1</sup>, Arie van Houselt<sup>1</sup>, Detlef Lohse<sup>2</sup>, Harold Zandvliet<sup>1</sup>, Stefan Kooij<sup>1</sup>

<sup>1</sup>Physics of Interfaces and Nanomaterials, University of Twente, Enschede, Netherlands  
E-mail: [w.kwiecinski@utwente.nl](mailto:w.kwiecinski@utwente.nl), URL: <https://www.utwente.nl/en/tnw/pin>

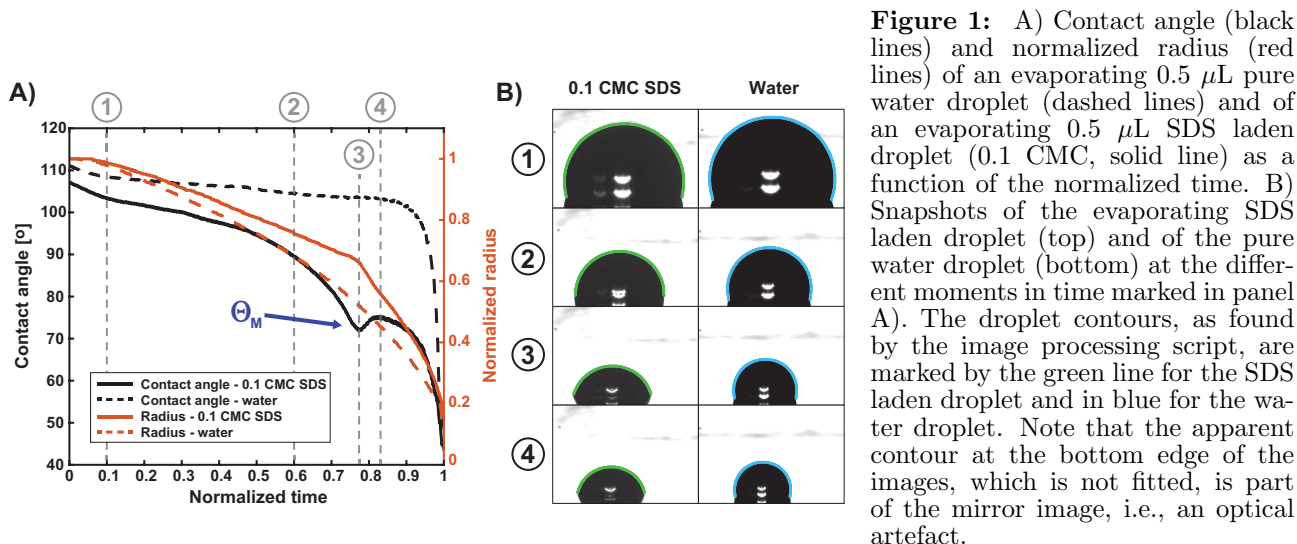
<sup>2</sup>Physics of Fluids, University of Twente, Enschede, Netherlands

### Introduction

Evaporation of surfactant laden sessile droplets is omnipresent in nature and industrial applications such as inkjet printing. Soluble surfactants start to form micelles in an aqueous solution for surfactant concentrations exceeding the critical micelle concentration (CMC). Here, the evaporation of aqueous sodium dodecyl sulfate (SDS) sessile droplets on hydrophobic surfaces was experimentally investigated for SDS concentrations ranging from 0.025 to 1 CMC.

### Research motivation

When a soluble surfactant is added to a liquid, its surface tension decreases with increasing surfactant concentration until a threshold value is reached, i.e. the critical micelle concentration (CMC), beyond which the surface tension is not affected any further. The decrease in surface tension caused by surfactants typically results in a lower contact angle. Next to surfactant behavior in the liquid bulk and at the liquid-gas interface, the evaporation process is potentially further complicated by surfactant adsorption at the solid substrate which can lead to dramatic changes in substrate wettability and therewith to phenomena such as superspreading [1] or auto-phobing [2]. The surfactant adsorption process, the conformation of the adsorbed molecules, and their effect on droplet evaporation are still poorly understood since they proved to be challenging to study. The main difficulty arises from the fact that the adsorbing surfactant layers are usually only a few nanometers in thickness and the adsorption process occurs in a liquid, which limits the available experimental techniques [3,4]. Furthermore, surfactant adsorption is highly specific for the surfactant-substrate combination and their chemical and physical properties resulting in a huge parameter space. Dynamically changing conditions and a moving contact line, present in the case of an evaporating droplet are complicating the problem even further. Therefore, extensively studied surfactant sodium dodecyl sulfate (SDS), an anionic surfactant commonly used in industry and research, was used to probe the influence of surfactant structures forming on a hydrophobic substrate on the evaporation process of dilute SDS aqueous solutions.



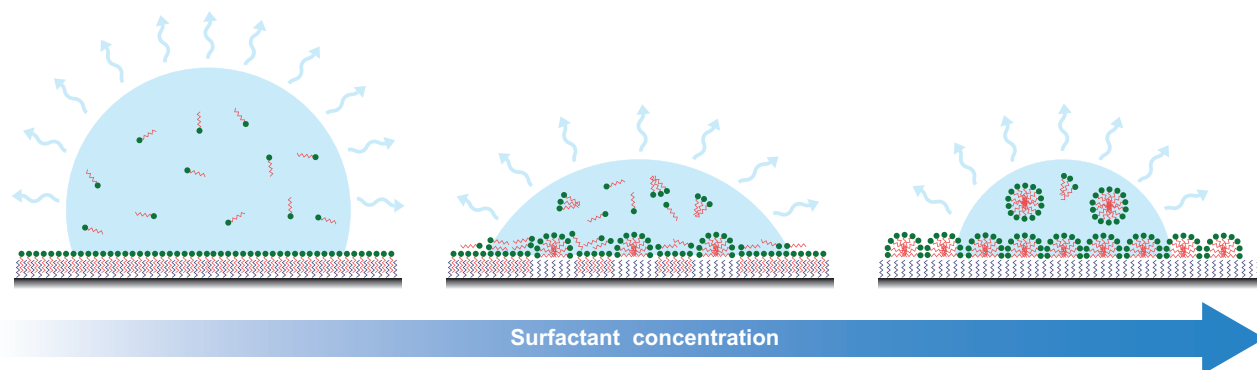


**Figure 2:** The schematic representation of the evaporation of droplet of a dilute aqueous SDS solution. Note that the contact angle of the droplet in the middle is smaller than the droplet on the right, which is in a later stage of the evaporation process.

## Results

Figure 1A shows the evaporation behaviour of pure water droplet (dashed lines) and 0.1 CMC SDS solution (solid lines). In contrast to the constant contact angle of an evaporating sessile water droplet, we observed that, at the same surface the contact angle of an SDS laden droplet first decreases, then increases, and finally decreases resulting in a local contact angle minimum ( $\Theta_M$  in Figure 1A). Surprisingly, the minimum contact angle was found to be substantially lower than the static receding contact angle and it decreased with decreasing initial SDS concentration. Furthermore, the bulk SDS concentration at the local contact angle minimum was found to decrease with a decrease in the initial SDS concentration. The location of the observed contact angle minimum relative to the normalized evaporation time and its minimum value proved to be independent of both the relative humidity and the droplet volume and thus, of the total evaporation time. We discuss the observed contact angle dynamics in terms of the formation of a disordered layer of SDS molecules on the substrate at concentrations below 0.5 CMC. The formation of the surfactant layers on a hydrophobic substrate during the evaporation of dilute aqueous SDS solution and its influence on the evaporation process is schematically shown in Figure 2. The disorder was caused by the dynamically changing surfactant concentration during the evaporation process and the presence of the contact line. Disorder in a surfactant layer leads to non-uniform wetting properties of the surface and thus, promotes the contact line pinning.

## Conclusion

We have found that formation of surfactant structures can influence the evaporation process of dilute aqueous SDS solutions. Furthermore, the observed behaviour was incredibly robust and repeatable. The present work highlights the complexity of the evaporation sessile liquid-surfactant droplets and the influence of surfactant-substrate interactions on the evaporation process. We are looking forward to presenting at the summer school *Complex Motion in Fluids 2019* at Kysthusene, near Gilleleje, Denmark, on 18 - 24 August 2019.

## References

- [1] S. Rafa et. al. *Langmuir* **18**, 10486-10488 (2002).
- [2] B. Bera et. al. *Soft Matter* **12**, 4562-4571 (2016).
- [3] S. Mane, H.E. Gaub et. al. *Science* **270**, 1480-1482 (1995).
- [4] M. Duan et. al. *Journal of Colloid and Interface Science* **417**, 285-292 (2014).



# Pinning Free Evaporation of Sessile Droplets of Water from Solid Surfaces

Steven Armstrong, Glen McHale, Rodrigo Ledesma-Aguilar and Gary G. Wells

Smart Materials & Surfaces Laboratory, Northumbria University, Newcastle upon Tyne, UK  
E-mail: steven2.armstrong@northumbria.ac.uk

## Introduction

Young's law is the starting point for many studies of sessile droplets but is an idealization that is rarely correct for real surfaces due to contact line pinning. Contact line pinning is a fundamental limitation to the motion of contact lines on solid surfaces and is a contributing factor to contact angle hysteresis. In diffusion-limited evaporation, contact angle hysteresis causes the sessile drop contact line to pin and de-pin. Without contact angle hysteresis, a quasi-equilibrium should occur with a constant contact angle and steady decrease in the contact area during evaporation. Contact line pinning can be overcome using Slippery Liquid Infused Porous Surfaces (SLIPS) which at their most slippery provide a completely lubricant coated surface.[1, 2] Previously we have shown droplet evaporation on a SLIP surface can give a mobile apparent contact line with a constant apparent contact angle.[3] However, since the droplet rests on a lubricant layer, there is no true droplet-solid contact line. Here we report constant contact angle evaporation of droplets of water on a solid surface consisting of a smooth flat glass substrate coated with a slippery omniphobic covalently attached liquid-like (SOCAL) layer (Figure 1). SOCAL repels water using liquid-like PDMS chains whose molecular mobility allow sessile droplets to move freely.[4] For a droplet evaporating at constant contact angle, the contact area of a droplet decreases linearly with time. We then analyze the constant contact angle evaporation mode for a range of relative humidity environments and show it can be used to accurately determine diffusion coefficient,  $D_E$ , of water vapour in air within 2% of the value reported in literature, thus validating the constant-contact angle mode of diffusion limited evaporation model (Figure 3).[5] Finally, we discuss how these slippery surfaces can be used in other situations, such as electrowetting[6], where contact angle hysteresis and contact line pinning is inherent.

## Constant Contact Angle Mode Evaporation

When a droplet is in contact with a solid surface, and at thermodynamic equilibrium, the contact angle that the droplet makes with the surface,  $\theta_e$ , is, in principle, determined by the interfacial tensions of the three interfaces as described by Young's law. When a droplet is small compared to its capillary length, it adopts an axisymmetric spherical cap shape when the surface is flat and smooth with no contact-line pinning. However, in practice contact-line pinning has always been observed to some extent. Geometrically this shape can be defined by its contact angle  $\theta$ , and its contact radius  $r$ . Knowing these two parameters, the volume of the spherical cap can be calculated. The surface underneath the droplet influences the space in which vapour from the evaporation can diffuse. Picknett and Bexon considered sessile droplet evaporation and provided an exact closed-form solution for its diffusion-limited evaporation  $f_{PB}(\theta)$ . [7] Their analysis includes two ideal modes of evaporation. The first corresponds to a Constant Contact Radius (CCR) mode, where the apparent contact angle decreases during evaporation. Since the CCR mode of evaporation requires complete pinning of the contact line, it can be achieved experimentally and has been widely studied.[8] The second mode is a constant contact angle (CCA) mode evaporation, where the contact angle is expected to retain a constant value approximating the contact angle predicted by Young's law whilst the contact area of the droplet decreases linearly in time (Figure 1).

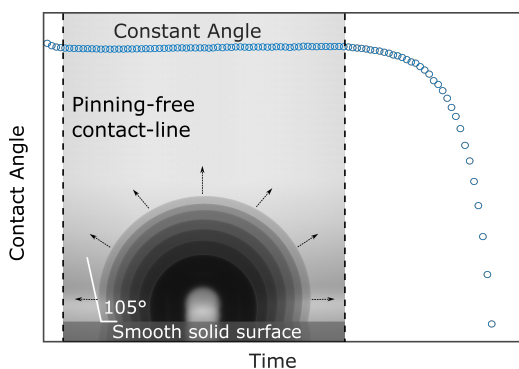


**Figure 1:** A sessile droplet of water placed on a Slippery Omniphobic Covalently Attached Liquid (SOCAL) surface, evaporates at a constant contact angle for the majority of the droplet's lifetime.

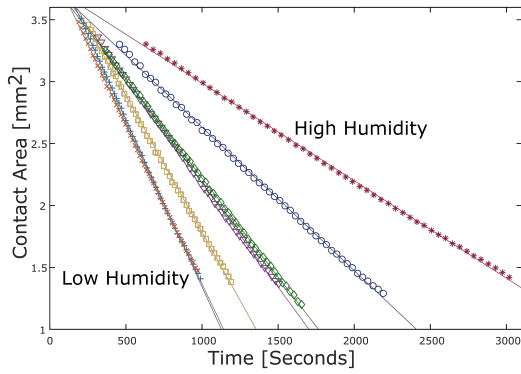


**Figure 2:** Contact area as a function of time for a broad range of humidities

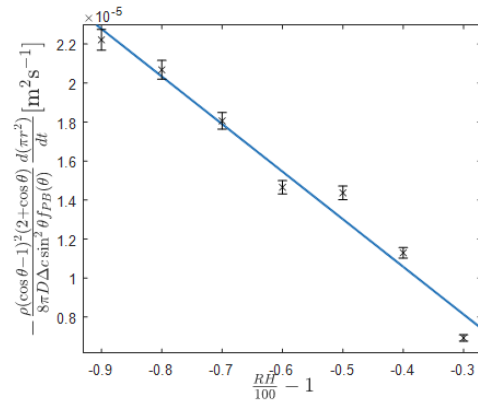


**Figure 3:**  $d\pi r^2/dt$  as a function of relative humidity. The slope of the plot gives the calculated diffusion coefficient  $D_E$

### Linear Change in Contact Angle and Calculation of Diffusion Coefficient

The rate of change in the contact area as a sessile droplet evaporates at constant contact area mode evaporation is given by,

$$\frac{d(\pi r^2)}{dt} = \frac{8\pi D\Delta c \sin^2\theta f_{PB}(\theta)}{\rho(\cos\theta - 1)^2(2 + \cos\theta)} \quad (1)$$

where  $D$  is the diffusion coefficient of water vapour in air,  $\Delta c$  is the difference between the vapour concentration close to the droplet and far away and  $\rho$  is the density of the liquid. Figure 2. provides confidence that we have observed constant contact angle mode evaporation, which is diffusion-limited. Since the diffusion coefficient should not depend on the relative humidity, rearranging eq. (1) and relating the relative humidity RH to vapor concentration by  $\Delta c = c_0((RH/100) - 1)$ , allows a single estimated diffusion coefficient,  $D_E$ , to be calculated using all experiments across the range of relative humidity 10%-70%,

$$\frac{\rho(\cos\theta - 1)^2(2 + \cos\theta)}{8\pi\Delta c \sin^2\theta f_{PB}(\theta)} \frac{d(\pi r^2)}{dt} = D_E \left( \frac{RH}{100} - 1 \right) \quad (2)$$

Figure 3 shows data from Figure 2 plotted using eq.(2) and the slope from this gives an estimate of the diffusion coefficient of  $D_E = (2.44 \pm 0.48) \times 10^{-5} m^2 s^{-1}$ , which is an improved estimate compared to the single relative humidity estimates and which is within 2% of the literature value.

### Conclusion

In this work, we have shown it is possible to observe the constant contact angle evaporation mode on a flat smooth (non-textured) solid surface by creating Slippery Omni-phobic Covalently Attached Liquid-like (SOCAL) coated surfaces with extremely low contact angle hysteresis. This differs from previous attempts to observe the CCA mode, which have relied on the use of textured solid surfaces, or a lubricant oil that removes all contact with a solid surface. Quantitative analysis of the sessile droplet evaporation sequences provides accurate measurements of the diffusion constant of the evaporating liquid. Hence, this methodology can provide a simple and reliable way to characterize the volatility of a wide range of other liquids.

### References

- [1] T.-S. Wong, S. H. Kang, S. K. Y. Tang, E. J. Smythe, B. D. Hatton, A. Grinthal, J. Aizenberg, *Nature* **2011**, *477*, 443–447.
- [2] J. D. Smith, R. Dhiman, S. Anand, E. Reza-Garduno, R. E. Cohen, G. H. McKinley, K. K. Varanasi, *Soft Matter* **2013**, *9*, 1772–1780.
- [3] J. H. Guan, G. G. Wells, B. Xu, G. McHale, D. Wood, J. Martin, S. Stuart-Cole, *Langmuir* **2015**, *31*, 11781–11789.
- [4] L. Wang, T. J. McCarthy, *Angewandte Chemie - International Edition* **2016**, *55*, 244–248.
- [5] S. Armstrong, G. McHale, R. A. Ledesma-Aguilar, G. G. Wells, *Langmuir* **2019**, *35*, 2989–2996.
- [6] Z. Brabcova, G. McHale, G. G. Wells, C. V. Brown, M. I. Newton, *Applied Physics Letters* **2017**, *110*, 121603.
- [7] R. G. Picknett, R. Bexon, *Journal of Colloid And Interface Science* **1977**, *61*, 336–350.
- [8] H. Y. Erbil, Evaporation of pure liquid sessile and spherical suspended drops: A review, **2012**.



## Contact Line Relaxation and Hysteresis Measurements on SOCAL Surfaces

Hernán Barrio-Zhang<sup>1</sup>, Élfego Ruiz-Gutierrez<sup>1</sup>, Gary G. Wells<sup>1</sup> and Rodrigo Ledesma-Aguilar<sup>1</sup>

<sup>1</sup>Smart Materials and Surfaces Laboratory, Northumbria University, Newcastle Upon Tyne, United Kingdom

E-mail: hernan.barrio-zhang@northumbria.ac.uk

### Introduction

Solids are not uniform and exhibit roughness at small scales. The chemical and physical imperfections that cause roughness affect the interaction between a liquid-gas interface and the solid, namely on its apparent contact angle and pinning behaviour. This is the reason why surface topography has become a promising variable for controlling wettability, adhesion, mobility and liquid transport [1] which underlines the importance of studying different surface configurations. Ultra-smooth surfaces, particularly Slippery Omniphobic Covalently Attached Liquid (SOCAL) surfaces, are well known to permit a liquid droplet to exhibit very low static friction [1-3]. However, measuring a low static friction force becomes difficult using classical methods. This work aims to show the complexity of characterizing such surfaces and study the interaction of pure water droplets on SOCAL surfaces.

### SOCAL, Contact Angle Hysteresis and Contact Line Relaxation

SOCAL surfaces are produced through acid-catalyzed graft polycondensation of dimethyldimethoxysilane and it is an interesting procedure due to its relative simplicity and the resulting liquid-like behaviour of the solid surface [2]. Contact Angle Hysteresis (CAH), the static friction exerted by a solid surface on a liquid droplet, is a quantity used to characterize surface attributes, such as smoothness and mobility. The lower this value is, the smoother the surface is believed to be [3]. CAH is defined as the difference of the instances prior to the movement of the contact line, defined as the advancing angle ( $\theta_a$ ) and the receding contact angle ( $\theta_r$ ), hence  $CAH = \theta_a - \theta_r$ . Classically, CAH is measured by inflating and deflating a droplet of liquid sitting on a substrate (Fig. 1a). Our results show that when CAH approaches zero, its measurement becomes unclear due to the sensitivity, scale and subjectivity of the measurement. Hence, we develop a method to measure CAH by analysing the behaviour of the contact line during the slow relaxation of the liquid-gas interface on a SOCAL surface (Fig. 1b and c). By analysing the asymptotic behaviour of the contact line, we are able to quantify CAH more precisely.

Even though the contact angle does relax to a constant value after pumping out, it was observed that the contact line continued to move. SOCAL has been reported to exhibit Constant Contact Angle (CCA) evaporation due to its remarkably low CAH [4] which could explain this residual motion. This has implications on the possible additional effects that Relative Humidity (RH) may have on the contact line and must be taken into consideration if one wants to have an accurate measurement of CAH. Hence, a study on the effect of relative humidity was conducted by measuring CAH at 92%, 80%, 50% and 30% RH and observing the behaviour of the relaxing contact line.

Our results show a clear improvement on the accuracy of contact angle measurements, particularly in high relative humidity environments where the contact line is most stable. Our study on RH shows that evaporation adds dynamic effects on the relaxing contact line and the contact angle. During the evaporation of a droplet, its contact lines are continuously receding, therefore the contact angle never reaches the stationary angle  $\theta_r$ . This shows the RH can bias the measurements of CAH on ultra-smooth surfaces, reinforcing the assertion that the only meaningful CAH measurement can only be done at higher RH where the droplet is close to phase coexistence.

### Conclusion

In conclusion, we have developed a method which quantitatively measures the values for  $\theta_a$  and  $\theta_r$ , increasing the precision of the measurement of CAH significantly. We also report the observed effects that evaporation creates due to changes in the RH of the environment. These effects include a continued motion of the contact line even after the mechanical perturbation of the droplet, which changes the apparent value of  $\theta_r$ . This points to the necessity of measuring CAH hysteresis in stable configurations for ultra-smooth surfaces such as SOCAL.

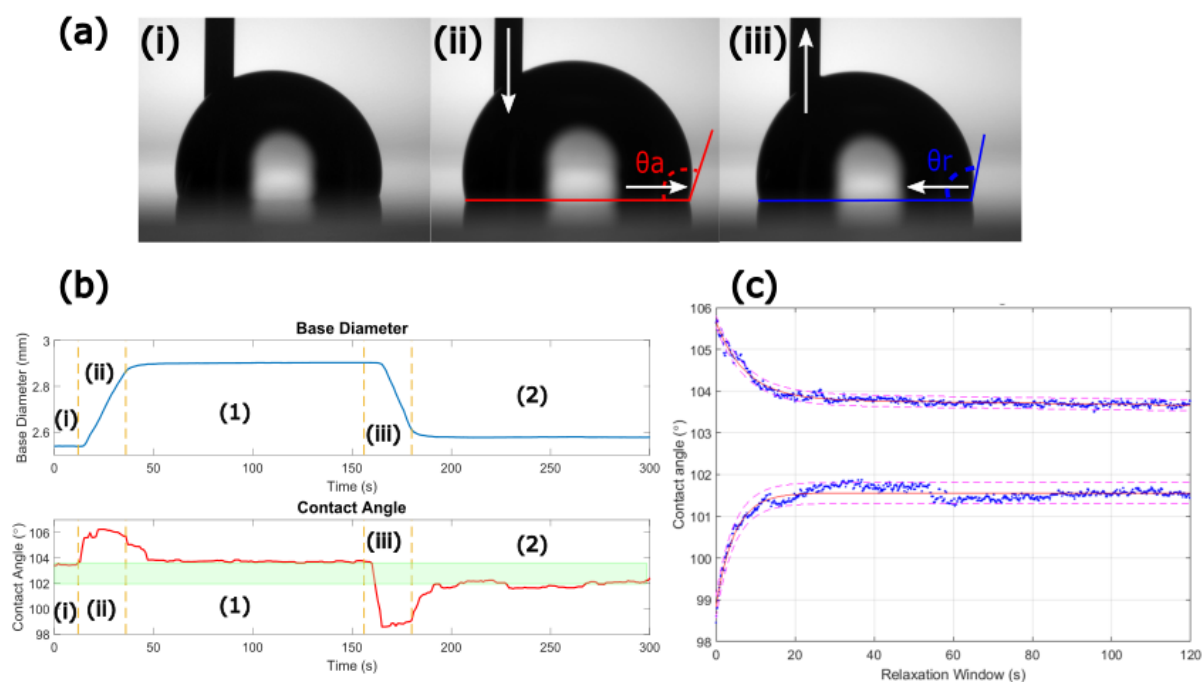


**Figure 1:** (a) Shows a schematic of the experimental methodology of increasing/decreasing the volume of the droplet: (i) Static regime, (ii) first dynamic regime (pumping in) and (iii) Second dynamic regime (pumping out). (b) Graphs showing the evolution of the base diameter of the droplet and the contact angle over time. The yellow markers indicate when pumping in or out is performed during the experiment and the green band is the approximate value of CAH. (c) Graph showing the fit of the contact angle relaxation regimes region 1 and 2.

## References

- [1] X. Yao, Y. Hu, A. Grinthal, L. Mahadevan and J. Aizenberg. *Nature Materials* **12**, 529-534 (2013).
- [2] L. Wang and T. McCarthy. *Angewandte Chemie - International Edition* **55**, 244-248 (2016).
- [3] P.G. De Gennes, F. Brochard-Wyart and D. Quéré. *Capillarity and Wetting phenomena*, Springer (2004).
- [4] S. Armstrong, G. McHale, R. Ledesma-Aguilar, and G. G. Wells. *Langmuir* **35**, 2989–2996 (2019).



## Role of the dynamic contact angle on splashing

Miguel A. Quetzeri-Santiago<sup>1</sup>, Kensuke Yokoi<sup>2</sup>, Alfonso A. Castrejón-Pita<sup>3</sup> and J. Rafael Castrejón-Pita<sup>1</sup>

<sup>1</sup>School of Engineering and Materials Science, Queen Mary University of London, London, United Kingdom

E-mail: m.a.quetzerisantiago@qmul.ac.uk

<sup>2</sup> School of Engineering, Cardiff University, Cardiff, United Kingdom

<sup>3</sup> Department of Engineering Science, University of Oxford, United Kingdom

### Introduction

Droplet impact phenomena on solid surfaces has been studied since the works of Worthington in the 19th century [1], and is still captivating scientists for its wide number of applications and parameters governing the process. Upon impact a droplet can spread, bounce off the substrate or splash depending on the liquid characteristics -viscosity  $\mu$ , surface tension  $\sigma$  and density  $\rho$ -, the droplet diameter  $D_0$ , the solid properties -wettability and surface roughness-, the impact speed  $U_0$  and the ambient pressure [2-4]. Droplet impact phenomena are traditionally characterised through the Weber ( $We = \frac{\rho D_0 U_0^2}{\sigma}$ ) and Reynolds ( $Re = \frac{\rho D_0 U_0}{\mu}$ ) numbers. Upon impact, droplet deposition typically occurs at low Weber and Reynolds numbers. In contrast at sufficiently high Weber and Reynolds numbers the droplet will make a splash, i.e. will break into secondary droplets [1]. Many studies have been devoted to find the underlying physics and parameters that can predict the splashing threshold for different liquid-substrate combinations, however these parameters have remain elusive [2-6].

In this work we study the influence of the wettability on the dynamic contact angle and splashing. The experiments consists of the visualisation, by high speed imaging, of the impact of ethanol, water and aqueous glycerol droplets on solid substrates ranging from wetting to non-wetting. From the experimental setup we measure the dynamic contact angle as a function of the contact line velocity. We observed that the dynamic advancing contact angle reaches an asymptotic value ( $\theta_{max}$ ) and that for every liquid-solid combination this angle is larger than 87 degrees. Finally, we show that a scaling parameter containing the air viscosity, the impact velocity and the liquid drop properties in terms of the asymptotic dynamic contact angle adequately separates the splashing behaviour.

### Experimental Method

Liquid drops were generated by dripping and were accelerated by gravity downwards to impact a dry solid substrate perpendicularly. The liquids used in the experiment were ethanol, water and an aqueous glycerol solution, and the solids used were glass slides, cast acrylic, perfluorinated glass slides and glaco coated glass slides. Our set up allows us to extract the dynamic contact angle of the different liquid/substrate combinations in the deposition case. The dynamic contact angle ( $\theta_D$ ) at each frame was measured with a costume Matlab code to asses the substrate wettability. We also varied the impact speed around the critical splashing velocity for each liquid/substrate combination. Splashing events were directly identified from the images, where splashing refers to a droplet breaking and ejecting at least one secondary droplet during spreading. All the experiments were recorded with a Phantom V710 or a Phantom V2512 high-speed camera coupled with a microscope lens and illuminated by a LED array and a diffuser.

### Results and Discussion

We found that there are three main types of contact angle dynamics as a function of the contact line speed  $u_{CL}$  depending if the surface is hydrophilic, hydrophobic or superhydrophobic. In the hydrophilic surfaces there is no receding phase as the contact line remains pinned at the maximum spreading diameter. For the hydrophobic ones we observe an almost constant advancing and receding contact angles and the contact angle hysteresis is observed at  $u_{CL} = 0$ . For the superhydrophobic substrates we observe an almost constant dynamic contact angle of  $\theta_D \approx 140$  degrees during spreading and receding phases, only to vary when the droplet is about to bounce off the substrate. We observed that for all of the surfaces and liquids the dynamic advancing contact angle reached an asymptotic value.

Here, for future analysis, we define  $\theta_{max}$  as the advancing asymptotic value of the dynamic advancing contact angle. In this study  $\theta_{max}$  is  $> 87 \pm 4$  degrees for all the liquid/substrate combinations. Our results also show that commonly used parameters to characterise splashing such as the splashing parameter  $K = We^{1/2}Re^{1/4}$  and the capillary number  $Ca = \frac{\mu U_0}{\sigma}$ , are not appropriate to characterise the splashing behaviour. In figure 2, we show that the splashing is favoured by high impact speeds and by large maximum contact angles  $\theta_{max}$  and is effectively characterised for all the liquid/solid combinations by the splashing parameter  $\beta$  [6],

$$\beta = \frac{3.85\mu_g^{1/2}(\rho D_0 U_0^5)^{1/6}}{\sigma^{2/3}}, \quad (1)$$

where  $\mu_g$  is the surrounding air viscosity.

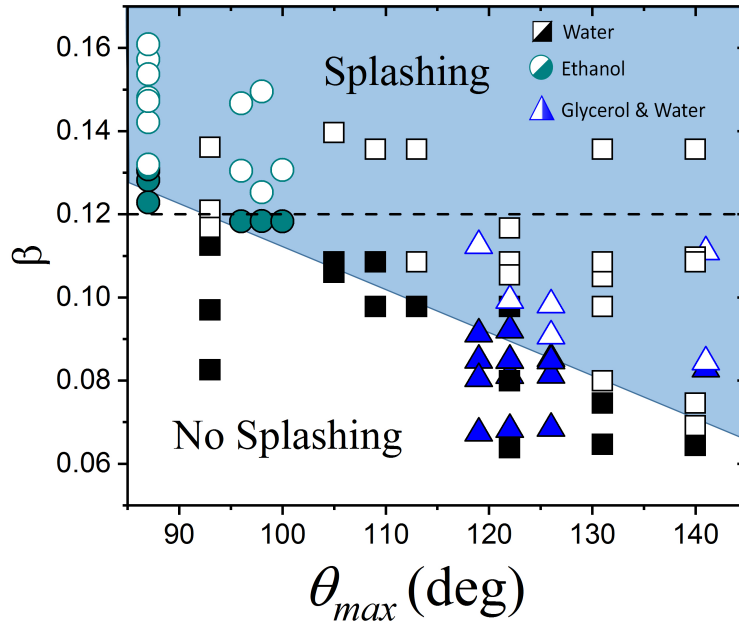


**Figure 1:** Water drop impacting with a Weber number  $We = 462$  on a hydrophilic substrate (no splash) and a superhydrophobic substrate (splashing). Splashing in terms of  $\theta_{max}$  and the splashing parameter  $\beta$ . Open symbols represent splashing while solid ones stand for no splashing. The dashed line is from de Goede et. al (2017).

## Conclusion

We have shown that droplet splashing depends not only on the liquid properties but also on wettability, especially on  $\theta_{max}$ . We have also found that within our experimental range  $\theta_{max}$  is greater than  $87 \pm 4$  degrees for all the liquid/substrate combinations. Finally, our results show that the splashing behaviour can be parametrised by the maximum dynamic contact angle  $\theta_{max}$  and the splashing parameter  $\beta$ . These findings have strong repercussions in several industrial environments such as in liquid dispensing, liquid coating, sprays, drug delivery and any other application where splashing can affect coating performance or compromise cleanliness (contamination).

## References

- [1] Arthur Mason, Worthington, Vol. 27125. Society for Promoting Christian Knowledge, 1895.
- [2] Michelle M. Driscoll and Sidney R. Nagel, Physical review letters, 107, 154502, Oct 2011.
- [3] Christophe Josserand and Sigurdur T Thoroddsen, Annual Review of Fluid Mechanics, 48, 365-391, 2016.
- [4] Ilia V. Roisman, Andreas Lembach, and Cameron Tropea, Advances in Colloid and Interface Science, 222, 615-621, 2015.
- [5] James C Bird, Scott SH Tsai, and Howard A Stone, New Journal of Physics, 11(6) 063017, 2009.
- [6] Guillaume Riboux and José Manuel Gordillo, Physical review letters, 113(2), 024507, 2014.



## Spreading Laws on Infused Materials

Saurabh Nath<sup>1</sup> and David Quéré<sup>1,2</sup>

<sup>1</sup> Physique et Mécanique des Milieux Hétérogènes, UMR 7636 du CNRS, ESPCI, 75005 Paris, France.  
E-mail: saurabh.nath@espci.fr, URL: <http://www.fysik.dtu.dk/CMiF2019>

<sup>2</sup> LadHyX, UMR 7646 du CNRS, École polytechnique, 91128 Palaiseau, France.

When a droplet first touches a solid surface, a bridge of liquid forms and grows, which leads to a sharp change in curvature. The gradient of this curvature drives the initial spreading of the droplet at speeds as high as 1m/s. However, the spreading speed is not constant but rather follows a (kind of) diffusive law resulting from a balance of inertia with surface forces. If  $r$  is the bridge width, this can be written:

$$r^2 \sim Dt$$

with  $D = (\gamma R/\rho)^{1/2}$ , denoting  $\gamma$  as the surface tension,  $\rho$  as the liquid density and  $R$  as the drop radius [1]. This law has been shown to hold at small time scales for wetting, partially wetting, chemically patterned, soft, and complex surfaces. Thus it appears to be extremely robust and insensitive to the properties of the substrate, as long this substrate is flat [2, 3]. Here we revisit this classical problem on a solid textured and infused with a liquid [4, 5]. Such surfaces are special because the liquid layer trapped in the texture lends them liquid-like properties. For example, these materials exhibit very little adhesion and they may also engender slip. Figure 1 shows how a millimetric water droplet spreads on a surface infused by silicone oil and comes to its equilibrium radius after a few milliseconds.

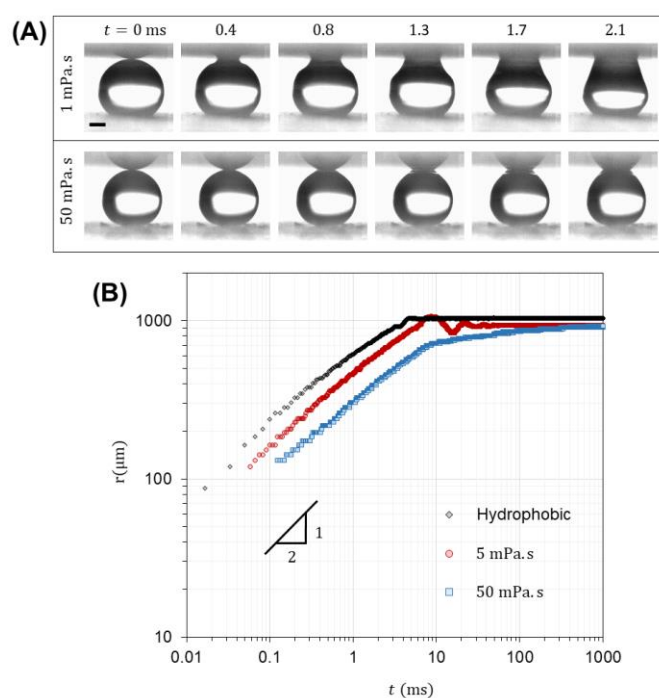


**Figure 1:** (A) Snapshots of a 4  $\mu\text{L}$  water droplet, initially resting on a superhydrophobic surface, after its top contacts a liquid-infused material, which leads to the formation of a liquid bridge and to its spreading. The oil used for infusion is a silicone oil with viscosity  $\eta = 1\text{mPa}\cdot\text{s}$  (top panel) or  $50\text{mPa}\cdot\text{s}$  (bottom panel). We observe that the water drop spreads slower on the more viscous surface, even at sort time scales. (B) The contact line radius plotted against time for a water droplet spreading on a bare hydrophobic surface, and on two liquid-infused surfaces with  $\eta = 5\text{mPa}\cdot\text{s}$  and  $\eta = 50\text{mPa}\cdot\text{s}$  infusions. The plots show that the radius initially grows as  $t^{1/2}$  and then equilibrates to its final radius  $\sim 1\text{mm}$ .

We observe that the initial stage of spreading follows a diffusion-type law in any case, yet with an effective diffusivity  $D$  that depends on the existence and nature of the oil used for infusion. The more viscous the oil, the smaller the value of  $D$ , which is found for instance to be half of that on a flat solid for the lowest viscosity we used (oil with viscosity comparable to that of water). In this work, we try to understand how the scaling law of spreading remains the same despite viscous dissipation, and more generally what fixes the kinetics of spreading on such materials.

### References

- [1] A.L. Biance, C. Clanet & D. Quéré, *Physical Review E* **69**, 016301 (2004).
- [2] A. Eddi, K. G. Winkels & J. H. Snoeijer, *Physics of Fluids* **25**, 013102 (2013).
- [3] B.B.J. Stapelbroek, H.P. Jansen, E.S. Kooij, J.H. Snoeijer & A. Eddi, *Soft Matter* **10**, 2641 (2014).
- [4] A. Lafuma, & D. Quéré, *EPL* **96**, 56001 (2011).
- [5] T.S. Wong, S.H. Kang, S.K. Tang, E.J. Smythe, B.D. Hatton, A. Grinthal & J. Aizenberg, *Nature* **477**, 443 (2011).



## Viscous Bouncing Drops

Aditya Jha, Pierre Chantelot and David Quéré

<sup>1</sup>PMMH, ESPCI Paris, 75005 Paris, France

<sup>2</sup>LadHyX, Ecole Polytechnique, 91128 Palaiseau, France

E-mail: david.quere@espci.fr

### Introduction

Water drops impacting on a water-repellent material undergo bouncing. Earlier work done by Richard *et al.* [1] showed that the coefficient of restitution  $\varepsilon$  of the bouncing water drop, that is the ratio of the take-off velocity to the impact velocity, can be as high as 0.91. Furthermore, Richard *et al.* [2] found that the contact time  $\tau_0$  results from a balance between inertia and surface tension and scales as  $\tau_0 \propto \sqrt{\rho R^3 / \gamma}$  where  $\rho$  and  $\gamma$  represent the density and surface tension of water respectively and  $R$  is the radius of the drop. Specifically exploring the impact phase, Laan *et al.* [3] have studied the effect of viscosity on spreading of a drop. Complementary research by Bartolo *et al.* [4] looked at the transition of the retraction velocity over increasing viscosity and Ohnesorge number was found to control the switch-over from inertial to viscous regimes. In this experimental study, we investigate the effect of increasing viscosity of drops impacting a water-repellent solid using water-glycerol mixtures to vary the viscosity while keeping the drop size fixed at  $R = 1$  mm.

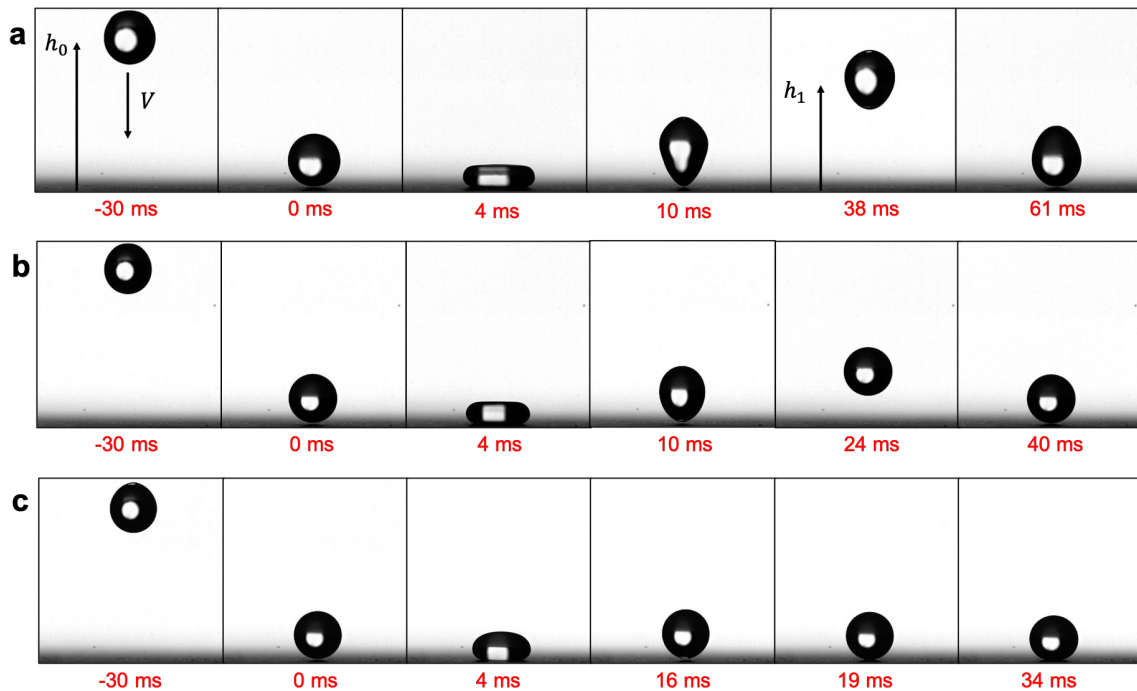


**Figure 1:** (a) Water drop ( $\eta = 1$  mPa.s) impacting on super-hydrophobic substrate, (b) Water/glycerol drop ( $\eta = 80$  mPa.s) impacting on the same substrate and (c) Water/glycerol drop ( $\eta = 200$  mPa.s) impacting on the same substrate. The radius and impact velocity of the drops remain the same at  $R = 1$  mm and  $V = 0.3$  m/s, respectively.

Figure 1a shows the behavior of millimetric water drop impacting on a super-hydrophobic surface and its rebound. Remarkably, even when the viscosity is increased 80 times to that of water (Figure 1b), the drop still bounces off from the surface. Furthermore, the time of contact  $\tau_0$  remains nearly the same though the effect of viscosity is clearly visible in the reduction of the maximum height  $h_1$  achieved after rebound. Further increasing the viscosity to 200 mPa.s leads to a near complete suppression of rebound, although the drop still recoils after the spreading, which defines the limiting bouncing viscosity for this family of drops.

## Conclusion

In previous studies, the bouncing of a drop on super hydrophobic surfaces has been modeled using a spring-mass system where the stiffness of the spring scales with the surface tension  $\gamma$ . To take into account the bulk viscous effects, we add a damper to this system whose damping coefficient  $c$  scales as  $\eta R$ . Upon simplifying the resulting spring-mass-damper system, we obtain the contact time of the impacting drop taking into account the viscous effects. This contact time goes to infinity as the Ohnesorge number  $Oh = \eta/\sqrt{\rho R \gamma}$  becomes of order unity leading to deposition of the drop on the surface as seen experimentally. Furthermore, we can discuss how the value of  $Oh$  controls the elasticity of the rebound.

## References

- [1] D. Richard and D. Quere, *Europhysics Letters* **50**, 769-775 (2000).
- [2] D. Richard, C. Clanet and D. Quere, *Nature* **417**, 811-811 (2002).
- [3] N. Laan, K.G. de Bruin, D. Bartolo, C. Josserand and D. Bonn, *Physical Review Applied* **2**, 1-7 (2014).
- [4] D. Bartolo, C. Josserand and D. Bonn, *Journal of Fluid Mechanics* **545**, 329-338 (2005).



## Charging of drops impacting on superhydrophobic surfaces

Diego Díaz<sup>1</sup>, Michael Kappl<sup>1</sup>, and Hans-Jürgen Butt<sup>1</sup>

<sup>1</sup>Max Planck Institute for Polymer Research, Mainz, Germany  
E-mail: diaz@mpip-mainz.mpg.de

### Introduction

Charge separation from water drops has been relevant in energy harvesting applications that involves drop impact on hydrophobic polymers [1,2]. Although drop impact have been studied in more than one hundred years, there are still some questions about the physical mechanisms of this phenomenon. One of the main questions is the water drop electrification. Some studies have shown the possibility to charge water drops due to the electrification resulting by the interaction with superhydrophobic surfaces e.g. sliding and jumping droplets [2,3]. Electrification has been explained by the formation and subsequent disruption of an electrical double layer (EDL) at the surface-droplet interface. It has been seen in these studies that the absorption of hydroxyl ions from water by polymer surfaces before the EDL disruption is responsible for the charge left on the surface. This phenomenon has gained a lot of interest considering the possible applications in energy harvesting in small scale devices for monitoring environmental and medical processes, considering the real possibility to convert kinetic energy in electric energy from drops [4,5].

In this work, we measure and collect the charge of droplets after bouncing a superhydrophobic surface. An electric field is applied during the bouncing process to track the motion of drops and detect the deflection due to the presence of the electric charge. Since the charge separation can be associated with the time scale of the impact and the formation of the EDL, the retracting speed of contact line would be a factor of interest for a better understanding of the process.

### Experimental section

Superhydrophobic glass slides with silicone nanofilaments are used as drop impact targets. For the preparation of samples, glass slides of 26mm x 76mm x 1mm were coated using trichloromethylsilane (TCMS) based the method detailed by Artus et al. (2006) to form nanofilaments [6]. Figure 1 illustrates the setup used for water drop impact experiments.

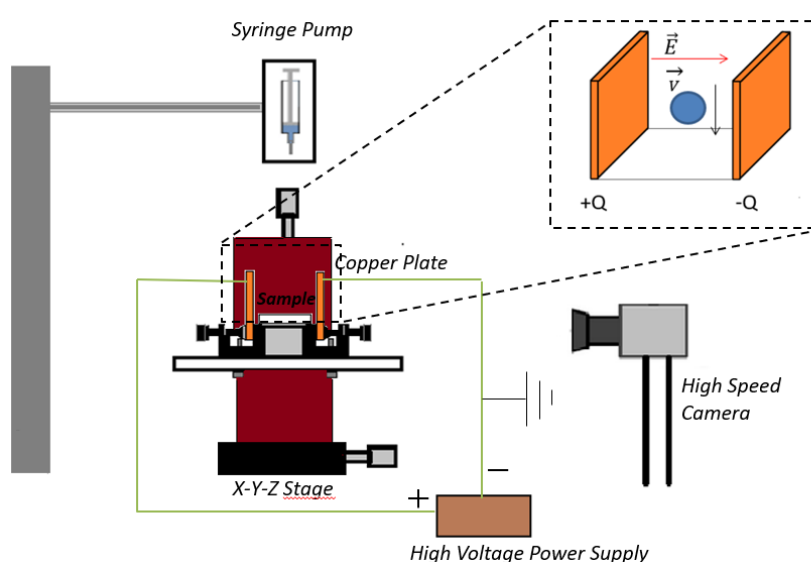
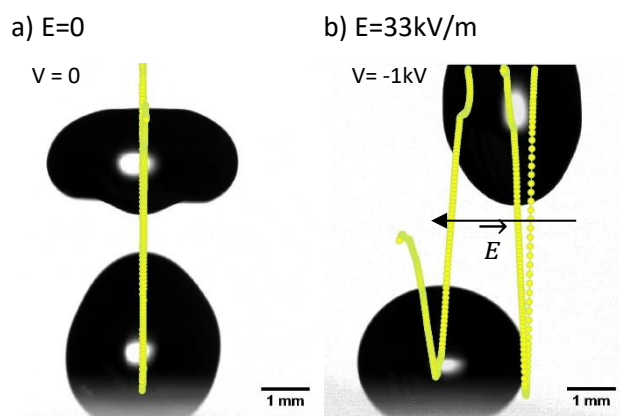


**Figure 1:** Sketch of the experimental setup. A motorized syringe pump dispenses water drops. To generate the electric field, a potential difference is applied using two copper plates separated 3 cm. A high-speed camera is used to register the droplet motion.

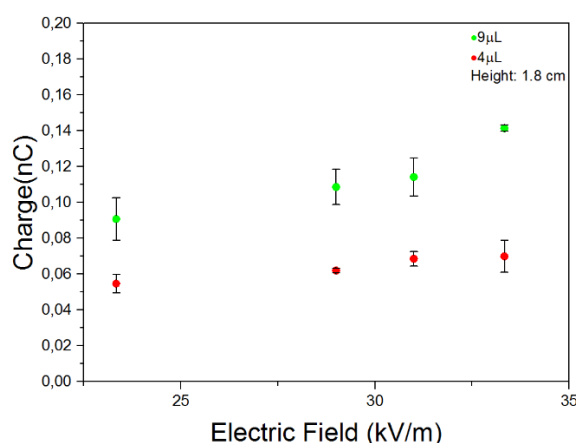
### First results

Figure 2 shows the behavior of a 4 $\mu$ L drop when an electric field is applied during the bouncing process. After bouncing on the nanofilaments surface, the droplets show a parabolic motion (Figure 2(b)) in the direction of the electric field. The trajectory is tracked and thus, we estimate the charge that drops carry by relating the horizontal displacement, the volume and magnitude of the electric field. We measure a maximum amount of charge in the order of 0.06-0.14 nC for drops of 4 $\mu$ L and 10 $\mu$ L respectively (Figure 3). If the charge accumulation in bouncing drops is associated with the formation of the EDL at the drop-surface interface as

well as in sliding and jumping drops [2,3], the interfacial contact area would be an interesting factor to study in detail.



**Figure 2:** Motion of a 4uL drop bouncing on a superhydrophobic surface due to the presence of an electric field. (a) Bounce without an electric field. (b) Uniform electric field (33kV/m) applied. The water drop displaces to the same direction of the electric field. The yellow markers represent the motion of the water drop mass center.



**Figure 3:** Charge measured for different electric fields for droplets of 4uL (red) and 9 uL (green).

## Conclusion

We are able to measure charge generation during drop impact and rebound on superhydrophobic surfaces from the deflection of the droplet trajectory in an electric field. Since the impact could transfer charge into the surface, we aim to test different parameters such as size of drops, type of surface, impact speed and salinity of drops for a better understanding of the charging mechanism. Although the amount of charge that we found means a low efficiency for electric energy generation, it may be useful for energy harvesting in small scale devices.

## References

- [1] Helseth, L. E. (2016). Electrical energy harvesting from water droplets passing a hydrophobic polymer with a metal film on its back side. *Journal of Electrostatics*, 81, 64-70
- [2] Lin, Z. H., Cheng, G., Lee, S., Pradel, K. C., & Wang, Z. L. (2014). Harvesting water drop energy by a sequential contact-electrification and electrostatic-induction process. *Advanced Materials*, 26(27), 4690-4696.
- [3] Miljkovic, N., Preston, D. J., Enright, R., & Wang, E. N. (2014). Jumping-droplet electrostatic energy harvesting. *Applied Physics Letters*, 105(1), 013111.
- [4] Tom Krupenkin and J. Ashley Taylor. Reverse electrowetting as a new approach to highpower energy harvesting. *Nature Communications*, 2:448, 2011
- [5] Zhaochu Yang, Einar Halvorsen, and Tao Dong. Power generation from conductive droplet sliding on electret film. *Appl. Phys. Lett.*, 100:213905, 2012.
- [6] Artus, G. R., Jung, S., Zimmermann, J., Gautschi, H. P., Marquardt, K., & Seeger, S. (2006). Silicone nanofilaments and their application as superhydrophobic coatings. *Advanced Materials*, 18(20), 2758-2762.



## Transitional Marangoni instability in sessile droplets with PBS

A. Darras<sup>1,2,3</sup>, N. Vandewalle<sup>1</sup>, and G. Lumay<sup>1</sup>

<sup>1</sup>GRASP, CESAM - Physics Department, University of Liège, B-4000 Liège; Belgium; <http://www.grasp-lab.org>

<sup>2</sup>F.R.S.-FRNS; B-1000 Bruxelles; Belgium

<sup>3</sup>Experimental Physics, Saarland University; D-66123 Saarbrücken, Germany

### Introduction

Evaporation of sessile droplets is a method to organize suspended particles on solid substrates. Many studies have demonstrated that Marangoni flows caused by surface adsorbed molecules or temperature gradients can strongly affect the dried deposit [1–4]. In the present work [5], we show experimentally how transitional Marangoni instability can be triggered by bulk-diluted tensio-active ions (more specifically, PBS). Thanks to Particle Image Velocimetry (PIV) analysis, we identify four different flow stages. The transition between them can be understood by considering the competition between the Marangoni flow and the mass conservation flow, usually responsible for the coffee-ring pattern. We also demonstrate that the initial ionic concentration can select a coffee-ring pattern or a more homogeneous dried deposit.

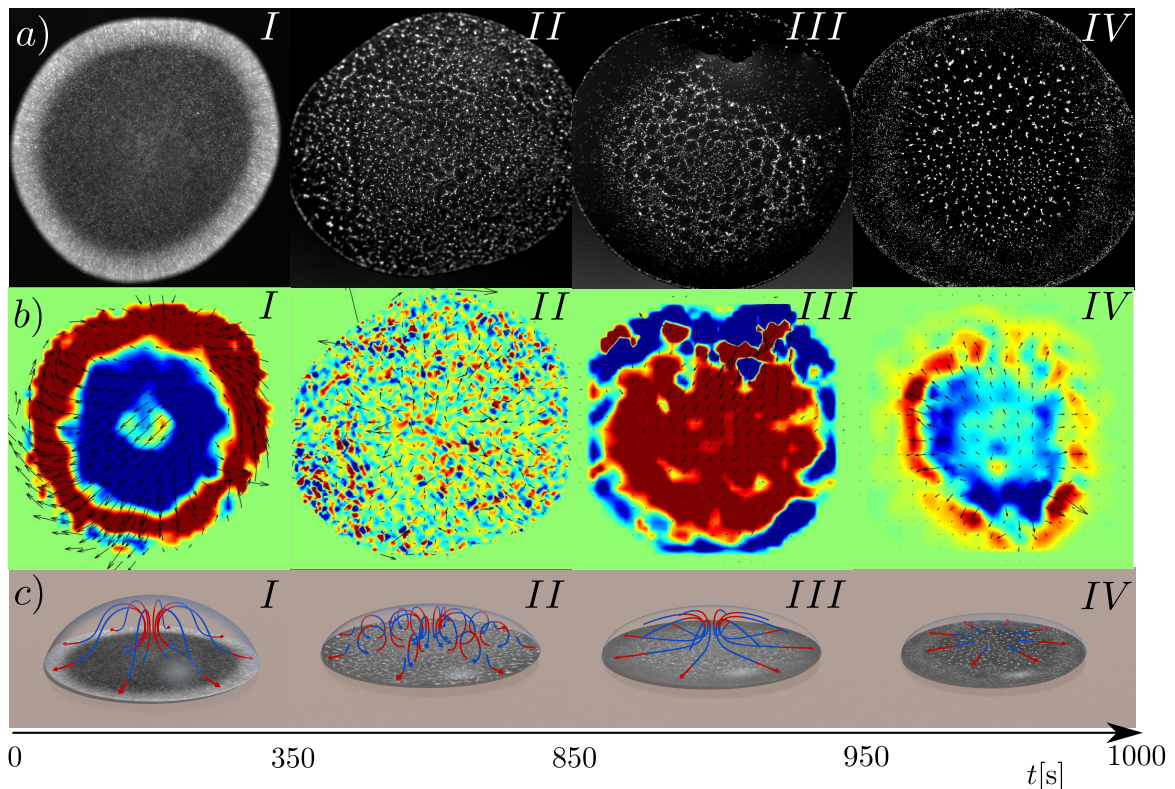


**Figure 1:** Main results from PIV measurements. The pictures in row *a*) are obtained experimentally with focus near the top of the droplet. The pictures for different times are then taken from different focus height. Row *b*) shows the computed 2D velocity field  $\vec{v}(\vec{r})$  corresponding to the upper pictures. The colors correspond to the velocity's 2D divergence  $\vec{\nabla} \cdot \vec{v}(\vec{r})$ , with blue being the positive values corresponding to areas from where the particles diverge and red being the negative values corresponding to areas of convergence. The green areas correspond to a zero divergence. Row *c*) depicts a 3D scheme of the streamlines based on the cumulative observations of the different heights, the colors of the arrows qualitatively matching the colors of the computed divergence. The approximate time of the transition between the different stages is indicated below in seconds with a typical precision of 20 s. Stage *I* corresponds to an outward flow. During stage *II*, a honeycomb-like pattern is observed near the surface of the droplet due to Marangoni instability. This pattern is then somehow collapsing on itself near the center of the drop during stage *III*. An outward flow, which tends to destabilize the previous structure, is observed during the final stage *IV*.

## Dynamic observations

We prepared three different suspensions, each of them with various concentrations of PBS but with the same colloidal volume fraction of  $\phi = 50 \cdot 10^{-5}$  for the M1-070 and  $\phi = 2 \cdot 10^{-5}$  for the F1-100XC. The PBS was diluted in volume fraction as  $6 \cdot 10^{-3}$ ,  $10 \cdot 10^{-3}$  and  $50 \cdot 10^{-3}$  of the respective final suspensions. To perform the observations, a  $2 \mu\text{l}$  droplet of the suspension is placed on a microscope cover glass. A custom airtight evaporative chamber is placed upon it. We were able to determine four different stages during the evaporation process, observed for every tested concentration of PBS and illustrated in Fig. 1. We showed [5] that the transition between the different stages can be understood mainly by considering a competition between the mass conservation flow, usually responsible for the coffee-ring effect, [3] and a solutal Marangoni instability. [6, 7]

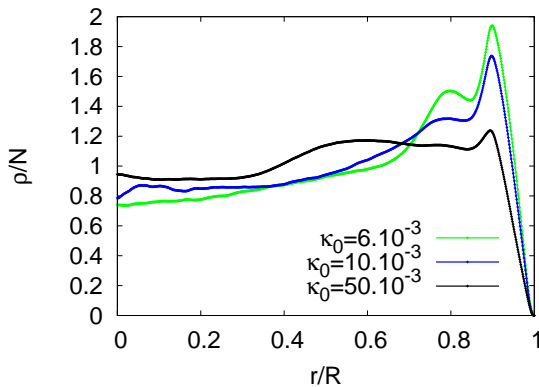


**Figure 2:** Mean surface density of the dried agglomerates normalized by the number of particles (so that the integral of the curve is equal to one) as a function of the radial distance, for the various PBS concentration. For high PBS concentration the coffee ring effect is mainly countered, since the averaged density of the deposited particles is mainly uniform along the droplet's radius. Error bars are not shown in order to avoid overloading of the curves, however maximal standard deviation is below 10% of the curve value.

## Dried deposits

Those flows have a strong influence on the eventually dried deposit of the droplet. Indeed, high initial PBS concentration  $\kappa_0$  maintains the honeycomb-like structure created by the Marangoni recirculation even in the dried deposit, contrary to the low PBS concentration. The presence of this structure is then able to decrease and mainly prevent the coffee-ring effect. A quantitative analysis of the deposits can be performed by computing the mean surface density  $\rho$  of the deposit. We computed this quantity as a function of the relative distance from the centre  $r$  of the deposit, normalized by the radius  $R$  of the deposit. We then normalized it by its integral  $N = \int_0^1 \rho(\delta) d\delta$ , where  $\delta = \frac{r}{R}$ . This normalization enhances the relative variation values and ensures that no difference in lightening are taken into account. Resulting curves are presented in Fig. 2. As it can be concluded from those curves, the initial PBS concentration  $\kappa_0$  is a parameter which allows to switch continually from a classical coffee-ring deposit (see  $\kappa_0 = 6 \cdot 10^{-3}$  curve in Fig. 2) to a much more homogeneous deposit where the density of particles in the center and at the edge are comparable (see  $\kappa_0 = 50 \cdot 10^{-3}$  curve in Fig. 2).

## Conclusion

Our experiments evidenced the different flow steps induced by a solutal Marangoni flow in a sessile droplet by using PIV on various height of the droplet. Moreover, we were able to model most of the transitions and enhanced how the initial concentration of PBS influences the flow mechanisms by using simple dimension analysis. This analysis shows the key mechanism to understand the flow behavior is the competition between solutal Marangoni and mass conservation flow. We are looking forward to present those results at the summer school *Complex Motion in Fluids 2019* at Kysthusene, near Gilleleje, Denmark, on 18 - 24 August 2019.

## References

- [1] H. Hu and R. G. Larson, *Langmuir* **21**, 3972 (2005).
- [2] R. Bennacer and K. Sefiane, *Journal of Fluid Mechanics* **749**, 649 (2014).
- [3] J. R. Christy, Y. Hamamoto, and K. Sefiane, *Physical review letters* **106**, 205701 (2011).
- [4] T. Still, P. J. Yunker, and A. G. Yodh, *Langmuir* **28**, 4984 (2012).
- [5] A. Darras, N. Vandewalle, and G. Lumay, *Physical Review E* **98**, 062609 (2018).
- [6] X. Fanton and A. Cazabat, *Langmuir* **14**, 2554 (1998).
- [7] H. Hu and R. G. Larson, *The Journal of Physical Chemistry B* **110**, 7090 (2006).



# Drying of colloidal suspension droplets: from flowers to buckling crusts

Paul Lilin<sup>1</sup>, Philippe Bourriane<sup>1</sup>, Guillaume Sintès<sup>1</sup> and Irmgard Bischofberger<sup>1</sup>

<sup>1</sup>Department of Mechanical Engineering, Massachusetts Institute of Technology, Cambridge, USA  
E-mail: [plilin@mit.edu](mailto:plilin@mit.edu), URL: <https://www.mitfluidslab.com/>

## Introduction

Colloidal suspensions are ubiquitous in daily life, from coffee and milk to cosmetics and paints. Once dried, these colloidal systems form coatings that are prone to failure, as evidenced by the formation of craquelures in ancient paintings. Similarly, drying droplets of colloidal suspensions exhibit a variety of regimes depending on the amount of suspended particles; from the well-known coffee-ring effect in dilute suspensions to homogeneous coatings at larger colloid concentrations. The wetting property of the substrate is another key parameter controlling the morphology of the final dry state. Here, we investigate the drying of aqueous suspensions of silica nanoparticles on both hydrophilic and hydrophobic substrates for a large range of particle volume fractions. As water evaporates, the volume fraction increases leading to a stress build up in the solid deposit which eventually induces mechanical instabilities [1]. We discuss the contact line dynamics observed in the hydrophobic regime and the mechanical deformation of the deposit occurring in the hydrophilic case.

## Droplets drying on hydrophobic surfaces

We investigate the temporal evolution of a drying droplet deposited on a hydrophobic surface, a silanized glass slide, as shown in figure 1. When the contact angle reaches its receding value  $\theta = \theta_R$ , the contact line moves inward. Surprisingly though, when the radius reaches a critical value, the contact line re-pins. As convective flows transporting the particles to the interface are faster than Brownian diffusion of the colloids, a crust builds up. Later, this crust buckles and eventually fractures under capillary pressure [2]. We study the influence of the initial volume fraction on the pinning transition and observe that it occurs at an apparent critical volume fraction. By controlling the relative humidity we find that the radius at pinning is independent of the drying speed.

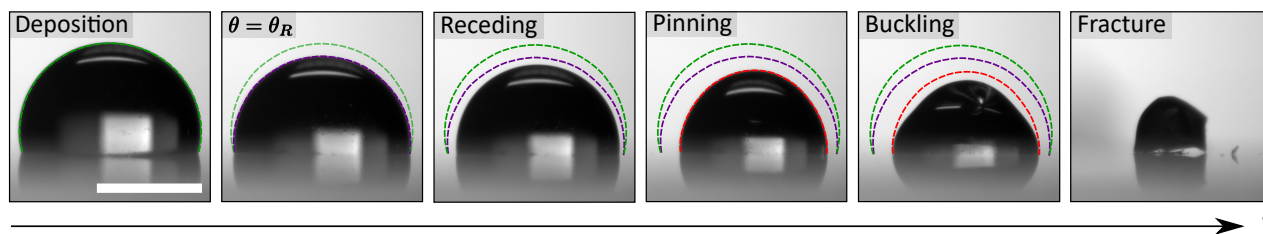


**Figure 1:** Temporal evolution of a 2  $\mu\text{L}$  drop with an initial particle volume fraction of 0.12, drying on a hydrophobic substrate ( $\theta_R = 95^\circ$ ) at  $T = 22^\circ\text{C}$  and relative humidity of 16 %. Dashed lines denote the shape at deposition (green), at  $\theta = \theta_R$  (purple) and at the moment of re-pinning (red). The total time of drying is 11 minutes. The scale bar represents 1 mm.

## Droplets drying on hydrophilic surfaces

When deposited on a hydrophilic substrate, a droplet of a colloidal suspension deposits a thin ( $\sim 10\text{--}50\ \mu\text{m}$ ) solid layer of close-packed particles (figures 2a, 2e). As the edge of the drop dries faster, a central liquid cap recedes (2a-d). Evaporation-induced stresses eventually generate radial cracks which propagate by avalanche, leading to the formation of petals (2d). We show that the distance between cracks is set by the deposit thickness, which we can tune by changing the volume fraction. The petals bend out of plane, forming a blooming flower (2e). We use interfero-microscopy to image the thin layer of air that forms under the deposit when the petals bend (2f). The interference fringes allow us to measure the shape of the petals during bending (2g). We find that the petals exhibit a quadratic shape, in agreement with a recent poroelastic theory [1] which describes the balance between elasticity and evaporation induced pore pressure. Systematically varying either the initial volume fraction or the relative humidity, we can independently vary the thickness of the deposit governing the elastic properties and the drying speed governing the pore pressure.

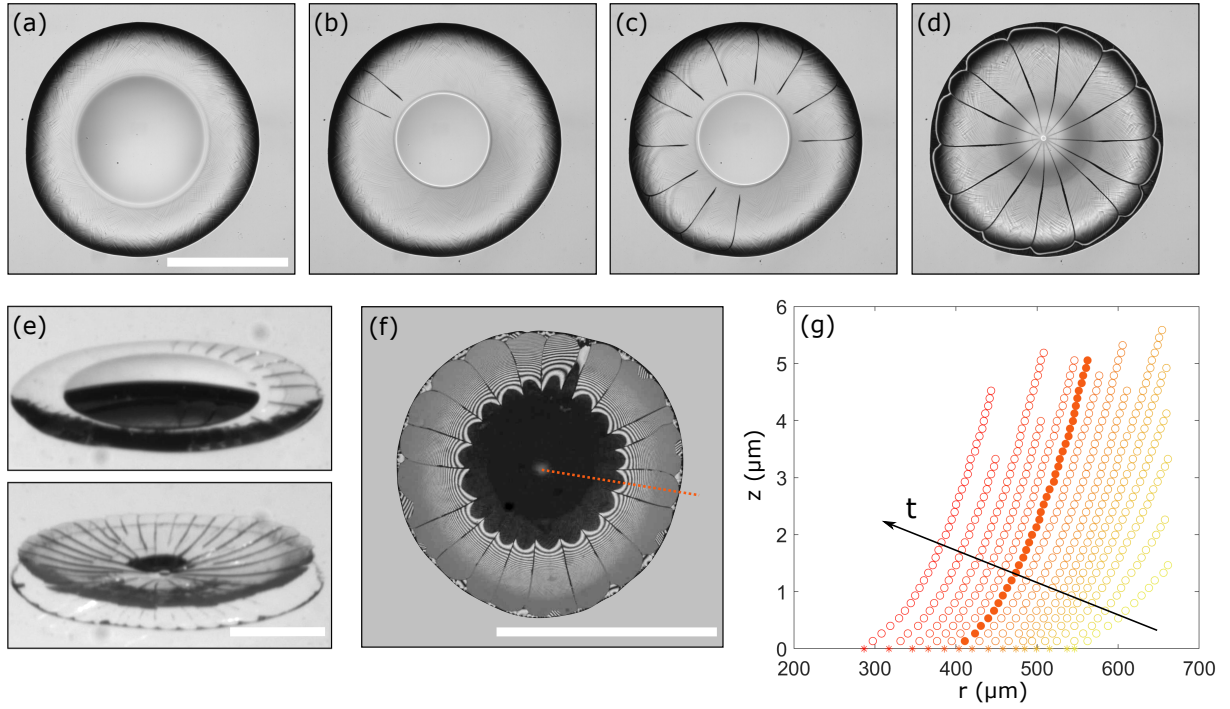


**Figure 2:** Structural features of a droplet deposited on a hydrophilic substrate. **(a-d)** Successive photographs of a  $0.3 \mu\text{L}$  drop with an initial particle volume fraction of 0.18. Note the receding water cap and the formation of radial cracks creating petals by an avalanche-like dynamics. **(e)** Side-view of a  $2 \mu\text{L}$  drop of the same volume fraction. The petals bend into a flower-like shape. **(f)** Interfero-microscopy image of a  $0.3 \mu\text{L}$  drop of the same volume fraction. The distance between two bright fringes denotes a height increment of  $\lambda/2 = 267.5 \text{ nm}$ . The orange dashed line indicates the petal analyzed in **(g)**. **(g)** Reconstructed profiles of one petal as a function of time. The peeling front propagates towards the drop center. The shape is quadratic throughout most of the bending process. The data denoted by the filled symbols corresponds to the dashed line in **(f)**. The scale bars represent  $1 \text{ mm}$ .

## Conclusion

The variety of patterns and mechanical instabilities observed in our experiments emphasize the influence of wettability on the drying of colloidal suspension droplets. The transition from radial crack formation and bending on a hydrophilic substrate to buckling and fracture on a hydrophobic substrate raises questions regarding the role of contact line pinning for the drying mechanism, which we are currently addressing.

## References

- [1] Giorgiutti-Dauphiné, F., and L. Pauchard. "Drying drops." *The European Physical Journal E* 41.3 : 32 (2018).
- [2] Bansal, Lalit, Ankur Miglani, and Saptarshi Basu. "Universal buckling kinetics in drying nanoparticle-laden droplets on a hydrophobic substrate." *Physical Review E* 92.4 : 042304 (2015).



## Evaporation-triggered ouzo effect in a confined environment

Ricardo Arturo Lopez de la Cruz<sup>1</sup>, Noor Schilder<sup>1</sup>, Xuehua Zhang<sup>1,2</sup>, and Detlef Lohse<sup>1,3</sup>

<sup>1</sup>Physics of Fluids Group, Faculty of Science and Technology, Mesa+ Institute, and J. M. Burgers Centre for Fluid Dynamics, University of Twente, 7500 AE Enschede, The Netherlands

E-mail: r.a.lopezdelacruz@utwente.nl, URL: <https://pof.tnw.utwente.nl/>

<sup>2</sup>Department of Chemical & Materials Engineering, University of Alberta, T6G1H9 Edmonton, Alberta, Canada

<sup>3</sup>Max Planck Institute for Dynamics and Self-Organization, 37077 Goettingen, Germany

### Introduction

The ouzo effect, named after the homonymous Greek liquor, is a phenomenon in a ternary mixture where a micro emulsion is formed spontaneously. This is the result of the different solubilities between the three components. Particularly, two of them have a very low mutual solubility while both are miscible with the third component. This effect has become of interest to the chemical science and industry due to its potential in applications like micro-particle formation [1], encapsulation of drugs [2], insecticide production [3], between others.

On the other side, understanding the effects that the droplet formation has on the flow around them and how this in turn affects the dynamics of the droplets has raised the interest of the physics community. Examples of previous studies include the evaporation and dissolution of ouzo droplets [4,5], solvent exchange in microfluidic channels [6] or co-flows in capillaries [7], where a very rich variety of phenomena has been observed.

Lu et. al. [8] studied the ouzo effect in a Hele-Shaw cell initially filled with a ternary mixture. In their case, oversaturation would be reached by diffusion of water from one side of the cell. Unexpectedly, this resulted in the formation of surface droplets, whose nucleation sites would form branch-like patterns, despite the different conditions tested.

In this work we have studied a similar system, where oversaturation was reached by evaporating the good solvent in the mixture. We have observed the process for different initial mass fractions of the components in the mixture, extending the results by Lu et. al. Surprisingly, we didn't observe the branch patterns for all cases, instead different phenomena going from clouds of droplets to bulk separation was obtained.

### Materials and methods

A mixture of ethanol, water and trans-anethole was used as our system. For this particular combination of liquids, a one phase homogeneous solution is obtained as long as the amount of ethanol is sufficiently

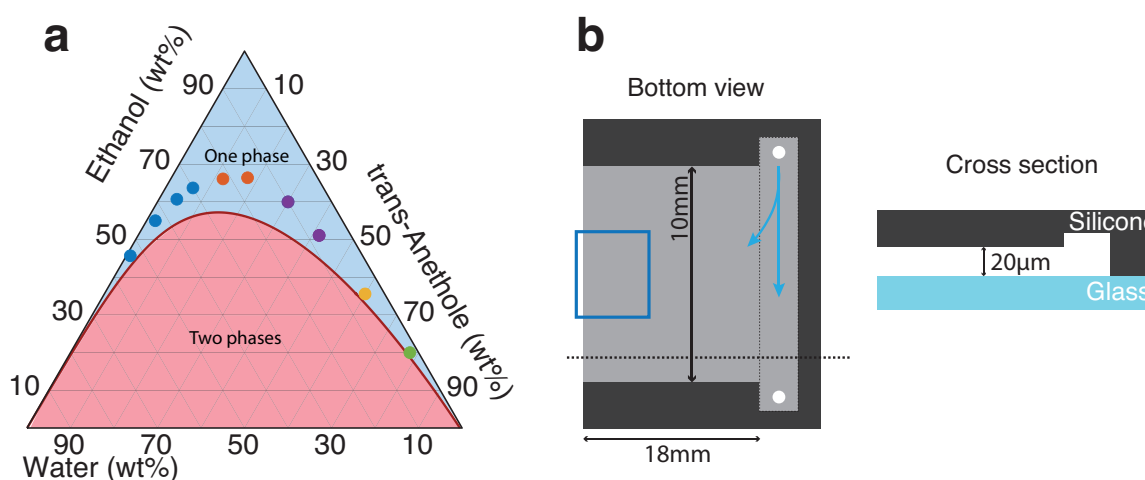


**Figure 1:** **a** Ternary diagram of the ethanol, water, trans-anethole mixture, showing the regions of one and two phases. The points represent, the different initial weight fractions tested. **b** Sketch of the Hele-Shaw cell used for our experiments, showing both a bottom view and a cross section (marked in the bottom view by a horizontal dashed line). The cell was made of one plate of silicone and another of glass to allow for observation. The gap between the plates was of  $20\ \mu\text{m}$ . A channel at the right was used to fill the Hele-Shaw cell while the edge at the left was expose to air to allow ethanol to evaporate. The arrows in the bottom view depict the flow in the cell when filling it and the blue square the field of view during our experiments.

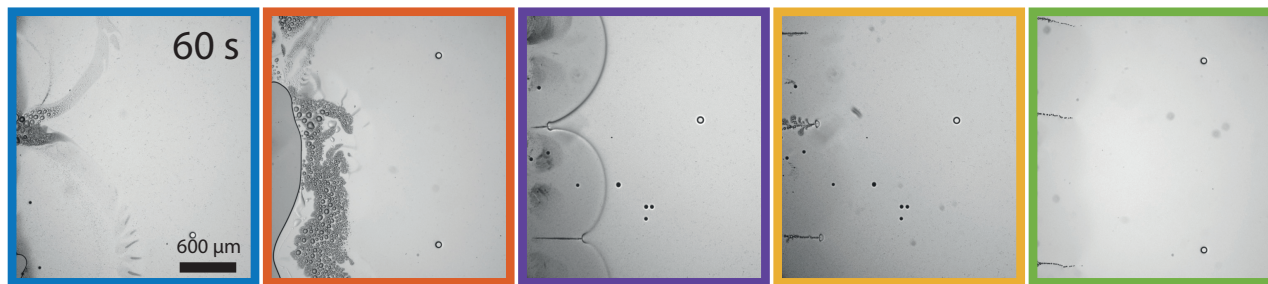


**Figure 2:** Snapshots of the evaporation process at the edge of the Hele-Shaw cell for 5 different initial concentration (from left to right: 2, 12, 41.6, 59.8 and 78 wt% of trans-anethole). The colors of the margin correspond with the colors in the ternary diagram of Figure 1. the snapshots were taken 60 seconds after the evaporation process started.

large, while for low amounts of ethanol the mixture separates in two phases. A ternary diagram showing for which mass fraction the mixture is in one or two phases is shown in Figure 1.a.

We have looked at the nucleation process close to the edge of a Hele-Shaw cell filled with this mixture as depicted in Figure 1.b. Since the edge is exposed to air, ethanol can evaporate causing the system to reach the two phases region in the ternary diagram. This results either in the formation of droplets or in bulk separation depending on the initial mass fraction of the mixture. We tested 10 different initial concentrations which are shown in the ternary diagram of Figure 1.a.

## Results

We separated the different experiments into 5 groups depending on the phenomena observed. Representative examples of each group are shown in Figure 2 (from left to right: 2, 12, 41.6, 59.8 and 78 wt% of trans-anethole). The snapshots were taken 60s after the evaporation process has started. The left edge of the snapshots corresponds to the open edge of the cell as depicted in Figure 1.b.

As can be seen, the ouzo effect takes place mainly for the first two groups, but for the second one a big agglomeration of oil is visible too. On the other side, bulk separation happens for the last three groups. In the fifth group, rows of water droplets nucleate instead of oil droplets, which corresponds with the "inverse" ouzo effect. The differences between the third and fourth group become clearer at later times. While in the third group a sharp interface is formed, in the fourth group the interface appears and disappears continuously.

We found out that the grow of the phase separation front initially goes as  $\sim \sqrt{t}$ , but eventually it slows down dramatically. This slow down occurs once the dome-like shapes (see first and third snapshot in Figure 2) merge together and cover the whole edge.

## Conclusion

Clearly in this case the droplet nucleation does not always result in branch-like patterns as in the case of Lu et. al. where they saw the patterns for many different conditions. We attribute this difference to the solutal Marangoni stresses at the air-liquid interface which result in strong flows close to the edge. This enhances the mixing of the solution and prevents the branch-like patterns in many cases. Additionally, depending on the initial mass fraction of the solution, different phenomena is observed, going from droplet nucleation to bulk phase separation and in some cases rows of droplets.

## References

- [1] S. Schubert, J. T. Delaney, and U. S. Schubert. *Soft Matter* **7**, 1581-1588 (2011).
- [2] S. J. Chiu, C. Y. Lin, H. C. Chou, and T. M. Hu. *Langmuir* **32**, 211-220 (2016).
- [3] A. Lucia, P. G. Argudo, E. Guzmán, R. G. Rubio, and F. Ortega. *Colloids Surfaces A Physicochem. Eng. Asp.* **521**, 133-140 (2017).
- [4] H. Tan, C. Diddens, P. Lv, J. G. M. Kuerten, X. Zhang, and D. Lohse. *Proc. Natl. Acad. Sci.* **113**, 8642-8647 (2016).
- [5] H. Tan, C. Diddens, M. Versluis, H. J. Butt, D. Lohse, and X. Zhang. *Soft Matter* **13**, 2749-2759 (2017).
- [6] R. Hajian and S. Hardt. *Microfluid Nanofluid.* **19**, 1281-1296 (2015).
- [7] Z. Lu, M. H. Klein Schaarsberg, X. Zhu, L. Y. Yeo, D. Lohse, X. Zhang. *Proc. Natl. Acad. Sci.* **114**, 10332-10337 (2017).



# CONTRTOLLING SELF-LUBRICATION AND SUPRA-PARTICLE FORMATION IN COLLOIDAL OUZO DROPLET

Lijun Thayyil Raju<sup>1</sup>, Olga Koshkina<sup>2</sup>, Huanshu Tan<sup>3</sup>, Hans-Jürgen Butt<sup>2</sup>, Katharina Landfester<sup>2</sup>, Xuehua Zhang<sup>4</sup>, and Detlef Lohse<sup>1,5</sup>

<sup>1</sup>Physics of Fluids Group, Max-Planck-Center Twente for Complex Fluid Dynamics, Faculty of Science and Technology, University of Twente, Enschede, The Netherlands

E-mail: [lijuntraju@gmail.com](mailto:lijuntraju@gmail.com), URL: <https://pof.tnw.utwente.nl>

<sup>2</sup>Max Planck Institute for Polymer Research, Mainz, Germany

<sup>3</sup>University of California, Santa Barbara, California, United States

<sup>4</sup>Department of Chemical and Materials Engineering, University of Alberta, Alberta, Canada

<sup>5</sup>Max Planck Institute for Dynamics and Self-Organization, Göttingen, Germany

## Introduction

Self-assembly of particles in an evaporating colloidal droplet attracts a lot of attention among researchers, owing to the rich physics involved in the deposition formation [1]. The particle assembly depends on a wide range of parameters such as particle size, particle shape, ambient conditions, substrate, pH of solution, surface charge on the particles etc [1].

Recently, it was shown that if we employ a ternary (water, ethanol and anise-oil) droplet as the dispersion medium, the dispersed colloidal particles can be assembled into a supra-particle by utilizing the “self-lubricating” effect. The self-lubricating effect helps to avoid pinning of the contact line and hence avoids the consequent formation of a flat and wide deposit on the substrate [2]. The self-lubrication phenomenon occurs due to the phase separation of anise-oil (by microdroplet nucleation, or Ouzo effect) and consequent formation of an “oil-ring” at the contact line of the droplet [2]. In this experimental study, we explore the role of the properties of colloidal particles in “self-lubrication” and consequent “supra-particle formation”. We show that size and surface texture of particles are important parameters affecting the supra-particle formation.

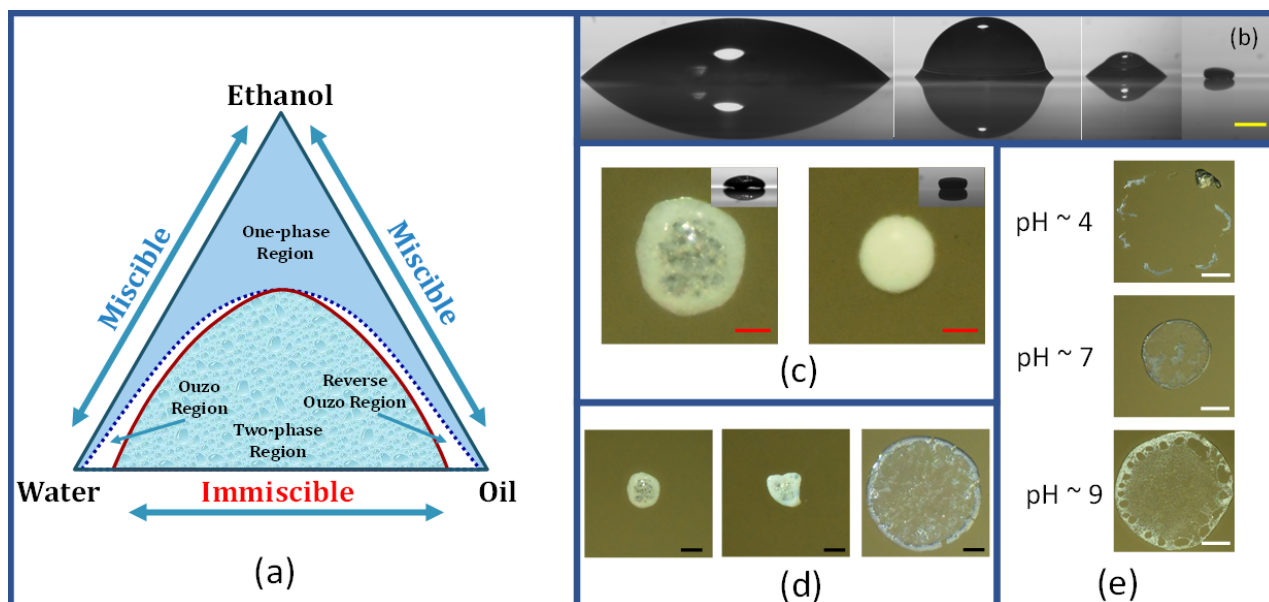


**Figure 1:** (a) Schematic ternary phase diagram of water-ethanol-oil; (b) Side view images showing different instances of evaporation of sessile colloidal Ouzo droplet, sitting on a hydrophobic surface. The rightmost image shows the shape of the final supra-particle, after all solvent has evaporated. Yellow scale bar : 0.2mm; (c) Top view images of the final deposit for different particle sizes : 100nm (left) and 600nm (right). Inset shows the side-view images for the same respective cases. Red scale bar : 0.1mm; (d) Top-view images of the final deposits using different surface modifications on silica particles : (left) amorphous silica particles, (middle) smooth mesoporous silica particles, (right) rough mesoporous silica particles. Black scale bar : 0.2 mm; (e) Top view images showing final deposits using rough mesoporous silica particles : effect of pH. White scale bar : 0.4 mm.

## Method and Results

Figure 1(a) shows the ternary phase diagram of water-ethanol-oil mixture. We disperse silica particles in a mixture of water-ethanol-transanethole, such that the dispersion composition is in the one-phase region. A drop of this mixture, of volume  $1\mu\text{L}$ , is deposited on a hydrophobic surface (Figure 1(b)). As the liquids evaporate, the differential rates of evaporation leads to an enrichment of water content in the drop (ethanol evaporates much faster than water; oil evaporates the slowest). This enrichment of water content causes the composition to shift to the Ouzo Region (Figure 1(a)) where nucleation of oil microdroplets (Ouzo effect) occurs. These oil microdroplets coalesce, leading to formation of oil ring at the contact line of the drop (Figure 1(b)). Once all the solvents have evaporated, the silica particles are left behind, forming either a supra-particle or some other deposit pattern on the substrate (Figure 1(b)).

Our experiments show that properties like particle-size, particle surface-texture and pH of the dispersion medium can greatly vary the final deposit pattern. Figure 1(c) shows that bigger sized particles form better supra-particles. Figure 1(d) shows the effect of surface texture of the silica particles on the particle assembly. It is observed that rough mesoporous particles show a coffee-ring like deposit. Finally, Figure 1(e) shows the effect of changing the pH of the dispersion medium (in case the rough mesoporous silica particles) on the deposition pattern. We observe that even after altering the pH, we cannot achieve supra-particle formation with rough mesoporous silica particles. However, the deposits show remarkable variations with changes in pH.

## Conclusion

The morphology of the final deposit obtained by the evaporation of a sessile colloidal ouzo droplet depends on the properties of the colloidal particles as well as the composition of the droplet. We are performing systematic study to investigate these effects and their role in the supra-particle formation.

## References

- [1] Maryam Parsa, Souad Harmand, and Khellil Sefiane. *Advances in Colloid and Interface Science*. 254, 22-47 (2018).
- [2] Huanshu Tan, Sanghyuk Wooh, Hans-Jürgen Butt, Xuehua Zhang, and Detlef Lohse. *Nature Communications* **10**, 478 (2019).



## Sliding droplets: influence of substrate's stiffness on pearling instability

Mathieu Oléron<sup>1</sup>, Matthieu Roché<sup>1</sup>, Julien Dervaux<sup>1</sup> and Laurent Limat<sup>1</sup>

<sup>1</sup>Laboratoire Matière et Systèmes Complexes (MSC), Université Paris Diderot, Paris, France  
E-mail: [mathieu.oleron@univ-paris-diderot.fr](mailto:mathieu.oleron@univ-paris-diderot.fr), URL: <http://www.fysik.dtu.dk/CMiF2019>

**Keywords:** Dynamical elastowetting, pearling instability, viscoelasticity.

If you pay attention to the motion of raindrops on a windowpane, you will quickly observe that droplets exhibit a wide variety of behaviors. Some fall down with a shape ranging from spherical to highly stretched, while others remains stuck to the glass. Sometimes the drop can even extend to the point where the liquid tail breaks into smaller droplets (see Fig 1).

This pearling instability, observable in such a common situation, actually find applications in every process that involves liquid runoff. It includes for instance surface coating [1], dew collection [2] or even inkjet printing.

In the past, this pearling instability has been widely studied in the case of a rigid substrate both theoretically and experimentally [3,4]. Inter alia, they have established that pearling is a self-similar instability. In other terms, no characteristic lengthscale governs its occurrence. Although studies involving sliding droplets on soft surfaces have highlighted additionnal viscous dissipation inside the substrate slows down the motion [5], they didn't focused on how the instability is influenced.

However, including the softness of the substrate as an additionnal ingredient to pearling precisely presents a fundamental interest from a scientific point of view. Indeed, a characteristic lengthscale intrinsic to the substrate, the elastocapillary length, is introduced in a self-similar instability. This lengthscale stands for the length below which deformation of the substrate are governed by surface tension forces (physical parameter characterizing the energy for creating a surface between two media by a slicing process) rather than elasticity. Thus, we may expect a size-dependent effect on pearling, given the forces applying at a moving triple line won't be the same depending on the scale we are looking at.

In this context, we are currently investigating experimentally how the pearling instability is impacted when the substrate becomes softer and softer.

### Experimental observations

Here we deposit glycerol droplets onto inclined soft PDMS substrates, whose stiffness can be tuned from 1 to 1000 kPa by mixing adequately two commercial solutions. A camera records a top view. As in the solid case, we recover the pearling instability when the relevant nondimensionnal parameter of the flow, here the capillary number, i.e. the ratio between viscous and capillary effects, increases beyond a critical value (see Fig 1).

Detecting the position of the droplet with time, we have very recently observed a more complex dynamics than expected. Indeed, small (compared to capillary length) droplets starts to slow down and eventually stops after tens of thousands seconds (see Fig 2). Thus, we cannot affect a single capillary number per experiment because of the strong variations of the drop velocity  $U$ . This slowdown at long timescales contrasts with observations in the case of an infinitely stiff substrate.

### Experimental prospectives

Based on the aforementioned observations, we aim at tackling two different aspects of the topic.

On the one hand, we would like to see what happens when viscous dissipation mainly occurs in either the drop or the substrate. Particularly, we would like to investigate, in the former configuration, potential differences between infinitely rigid and a soft substrate.

On the other hand, we would like to characterize the conditions under which the droplet slows down during motion and seek for the corresponding mechanism (pinning, dissipation, etc ...)

We are looking forward to present contributions to some of these prospects during *Complex Motion in Fluids 2019*, on 18 - 24 August 2019.

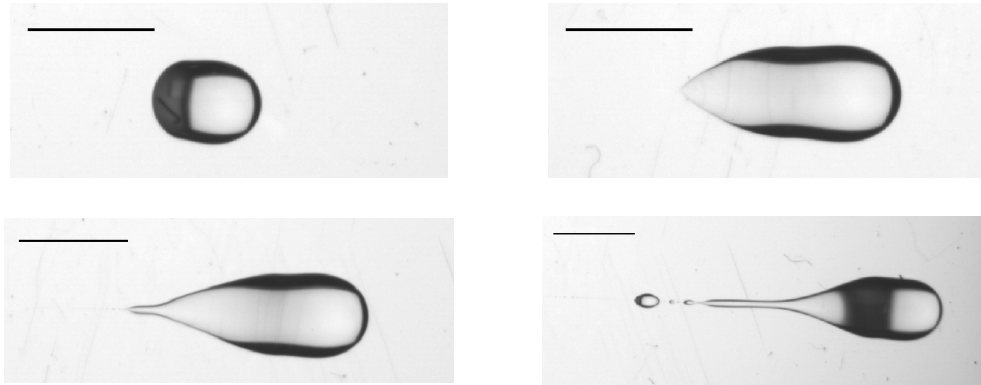


**Figure 1:** Adaptation of drop shape with an increase in capillary number  $Ca$ : from round to pearling instability. As  $Ca$  increases, the drop extends and its back narrows, forming a tail. Beyond a critical value, the tail becomes unstable and eventually breaks into smaller pearls. Scalebars always corresponds to 5 mm.

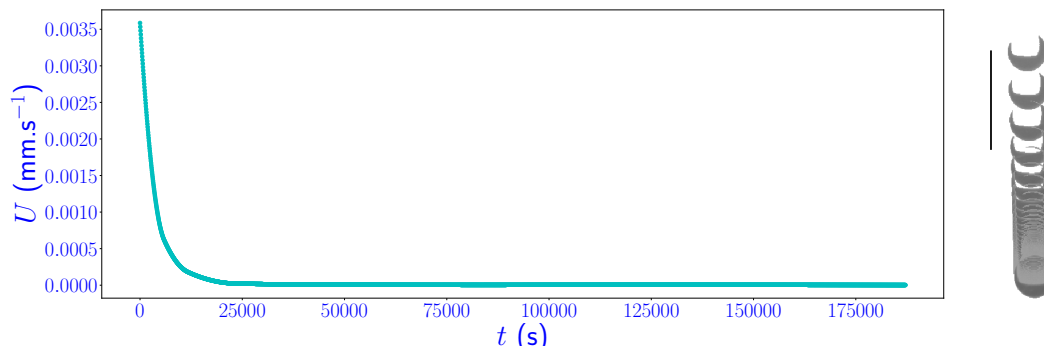


**Figure 2:** Motion of a  $4 \mu\text{L}$  droplet on a soft (shear modulus  $\mu = 1 \text{ kPa}$ ) substrate. The inclination angle is equal to  $41^\circ$ . On the left, its position  $x$  is plotted versus time. On the right, we display topviews of the droplet recorded each 720 s. The scalebar corresponds to 5 mm. We can notice the droplet drastically slows down and nearly stops after roughly 10000 s.

## References

- [1] T. D. Blake and K. J. Ruschak. *Nature* **282**, 489–491 (1979).
- [2] T. Nilsson *Solar Energy Materials and Solar Cells* **40**, 23-32 (1996).
- [3] J. Snoeijer, E. Rio, N. Le Grand and L. Limat. *Physics of Fluids* **17**, 072101 (2005).
- [4] T. Podgorski, J.-M. Flesselles, and L. Limat. *Phys. Rev. Lett.* **87**, 036102 (2001).
- [5] A. Carré and M. Shanahan. *Langmuir* 2001 **17**, 10, 2982-2985.



# Simulation of 2D Double Diffusive Convection in the Diffusive Regime

Rui Yang<sup>1</sup>, Steven Chong<sup>1</sup>, Richard Stevens<sup>1</sup> and Detlef Lohse<sup>1,2</sup>

<sup>1</sup>Physics of Fluids Group and Max Planck Center Twente for Complex Fluid Dynamics, MESA+ Institute and J.M. Burgers Center for Fluid Dynamics, University of Twente, P.O. Box 217, 7500AE Enschede, The Netherlands.

<sup>2</sup>Max Planck Institute for Dynamics and Self-Organization, 37077 Göttingen, Germany

## Introduction

Double diffusive convection in the diffusive regime is studied numerically in 2D as a model to investigate the convection flow driven by heat and salinity, which is relevant to the ocean environment in polar region[1]. A subcritical behavior based on the initial condition is explored within certain region. We also show the results of flow response such as heat transfer and flow velocity with different heat and salinity strength. A new flow structure is found with coexistence of convection and static region, which we refer to confined regime. The bistability and discovery of confined regime in double diffusive convection open up new avenues for studying heat transfer and potential layering mechanism in ocean [2,3].

## Explored parameter space

The main control parameters for double diffusive convection system are Rayleigh numbers for both heat and salinity, which are defined as  $Ra_T = \frac{g\beta_T L^3 \Delta_T}{\kappa_T \nu}$ ,  $Ra_S = \frac{g\beta_S L^3 \Delta_S}{\kappa_S \nu}$  and Prandtl numbers for thermal and salinity, which are defined as  $Pr_T = \frac{\nu}{\kappa_T}$ ,  $Pr_S = \frac{\nu}{\kappa_S}$ , respectively. The relative strength of the buoyancy force induced by temperature difference compared to that induced by salinity difference is measured by density ratio defined as  $R_\rho = (\beta_S \Delta_S) / (\beta_T \Delta_T) = Ra_S Pr_T Ra_T^{-1} Pr_S^{-1}$ , where  $\beta_T$  and  $\beta_S$  are the temperature and salinity expansion coefficient,  $\kappa_S, \kappa_T$  are the diffusivity for thermal and salinity,  $\Delta_T, \Delta_S$  are the temperature and salinity difference between top and bottom plates, respectively.

All explored simulation parameters are shown in Figure 1(a). Based on the flow morphology and flow response characteristics, three different regimes can be distinguished, which we refer to as the quasi-RB regime, subcritical regime, and confined regime. There are three groups of simulations with same  $Ra_T$  but different  $R_\rho$ .

For small  $R_\rho$ , the flow is dominated by the large scale circulation(LSC), which is similar to the pure Rayleigh-Bénard convection and referred to quasi-RB regime. When  $R_\rho$  becomes larger than 2, the flow becomes fully quiescent with initial linear temperature and salinity profiles while a LSC flow structure can be maintained with an initial LSC flow. We refer to this parameter range as subcritical regime because of the appearance of subcritical behavior. As  $R_\rho$  increases further, the suppression from salinity field is so strong that the flow can only be active in bulk region and dead zone occurs close to the boundary without any flow, which looks like that the flow is confined to the bulk region, see Figure 2. We refer it to the confined regime.

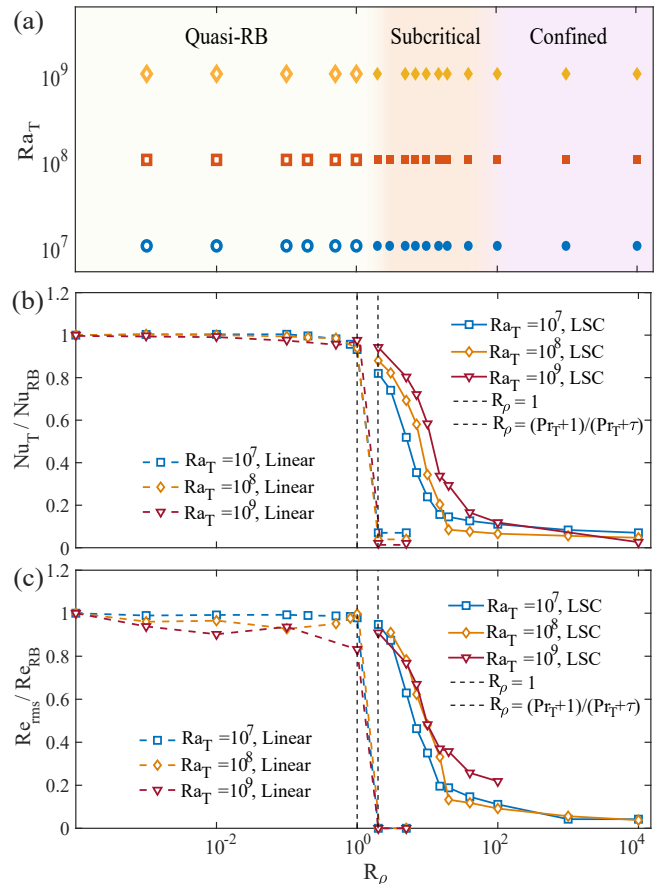


**Figure 1:** (a) Explored phase space and illustration of different regimes. Hollow points represent cases with linear initial condition. Solid points represent cases with LSC initial condition. Three flow regimes can be identified and indicated by different colors: the quasi-RB regime (yellow), the subcritical regime (orange), and the confined regime (purple). (b) Normalized thermal Nusselt number and (c) Normalized Reynolds number  $Re_{rms}$  versus density ratio  $R_\rho$  at  $Ra_T = 10^7, 10^8, 10^9$  with linear and LSC initial conditions. Solid lines represent cases with LSC initial condition. Dashed lines represent cases with linear initial condition.

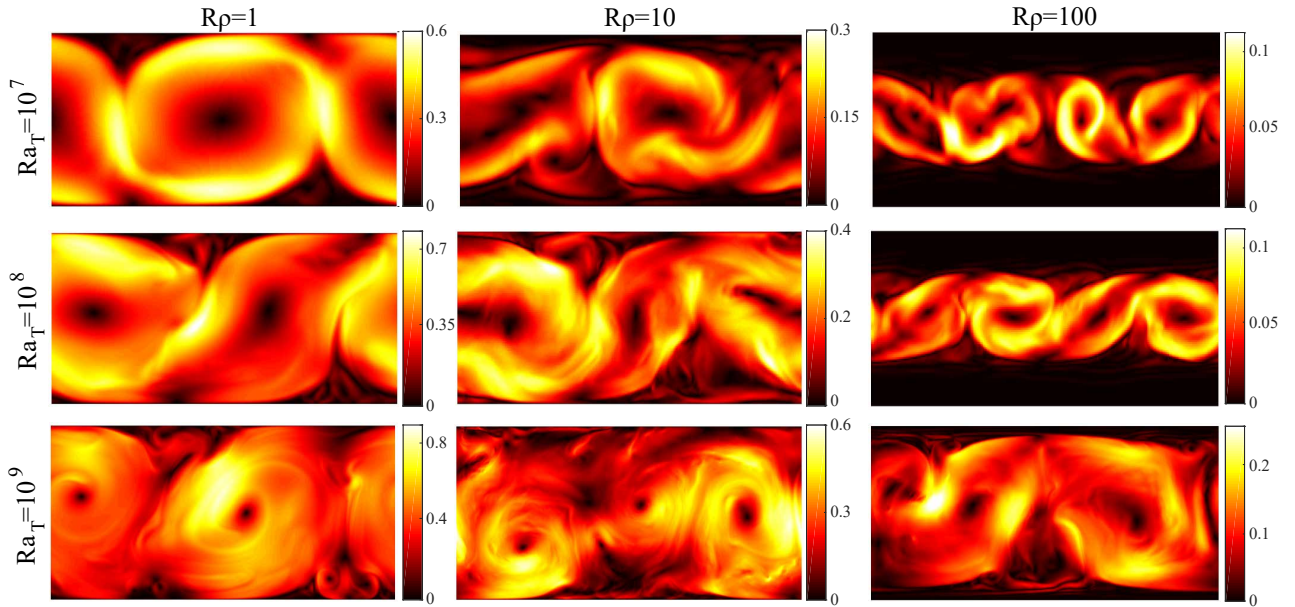


**Figure 2:** Snapshots of the amplitude of  $\mathbf{u}^2$  for  $Ra_T = 10^7, 10^8, 10^9$  and  $R_\rho = 1, 10, 100$

### Flow responses versus density ratio

The two most important global responses are the thermal flux and the flow velocity, which are usually measured by the Nusselt number  $Nu_T = \sqrt{Ra_T Pr_T} \langle u_z \theta \rangle_{A,t} + 1$  and Reynolds number  $Re = u_{rms} L / \nu$ . The variations of  $Nu_T$  and  $Re_{rms}$  normalized by the values of corresponding Rayleigh-Bénard flow at the same  $Ra_T$  and  $Pr_T$  as a function of  $R_\rho$  are shown in Figure 1(b)(c). The dashed lines represent the simulations with linear initial condition with different  $R_\rho$  and  $Ra_T$ , and the solid lines represent the simulations with LSC initial condition. The right vertical dash line represents the upper limit  $R_\rho = (Pr_T + 1) / (Pr_T + \tau)$ ,  $\tau = Pr_T / Pr_S$  based on the linear stability [4], above which there is no flow. From Figure 1(b)(c), as  $R_\rho$  increases and exceeds 2, the fluid is static with linear initial condition, which corresponds to the linear stability analysis well. While for LSC initial condition, the LSC still exists without damping out. As  $R_\rho$  increases further, the normalized  $Nu_T$  and  $Re_{rms}$  start to decrease smoothly and finally drop to the values of pure conductive case.

### Confined regime

Now we have a look at the confined regime shown in the phase space. The coexistence of convection flow in the bulk and static region near boundary at high  $R_\rho$  is discovered for the first time, which is revealed by the amplitude of flow  $\mathbf{u}^2$  plotted in Figure 2. In Figure 2, The large scale circulation is active in the whole field at  $R_\rho = 1$ . As  $R_\rho$  increases to 10, the flow intensity decreases and dark region occurs close to the boundary at  $Ra_T = 10^7$ . As  $R_\rho$  increases further to 100, the flow is still active but only in the bulk region because the suppression of salinity is so strong that the plumes can not reach the opposite plates, and the fluid near the boundary arrives the stable state, where the dead zone forms. Such a bulk active structure can also be regarded as a layering condition, with stable stratified region near the top and bottom plates and well-mixed region in the bulk.

### Conclusion

In summary, we conducted 2D simulation of the double diffusive convection in diffusive regime. The existence of subcritical behavior based on two different initial conditions is presented. The flow structure is observed to change with different density ratios and can be divided into three different flow states over the parameter space  $Ra_T = 10^7, 10^8, 10^9$  and  $R_\rho = 0 - 10^4$ .  $Nu_T$  and  $Re_{rms}$  changes versus density ratio  $R_\rho$  are presented, which can be related to the competition between stabilizing salinity and destabilizing heat at the thermal boundary layer height. The vertical confinement of flow in the bulk region at high  $R_\rho$  ( $R_\rho > 100$ ) is another interesting phenomenon which is worthy of further study.

### References

- [1] Kelley, D. E., et al. Prog. Oceanogr., 56.3-4 (2003): 461-481.
- [2] Yang, Y, Verzico, R., and Lohse, D. Proc. Natl. Acad. Sci. U.S.A., 113.1 (2016): 69-73.
- [3] Sommer, T., Carpenter, J. R., and Wüest, A. Geophys. Res. Lett., 41.14 (2014): 5114-5121.
- [4] Kato, S. Publ. Astron. Soc. Jpn., 18 (1966): 374.



## Three-dimensional full-loop simulation of cold gas-solid flow in a pilot-scale dual fluidized bed system - a preliminary study

Frederik Zafiryadis<sup>1</sup>, Anker Degn Jensen<sup>1</sup>, Martin Høj<sup>1</sup>, Yashasvi Laxminarayan<sup>1</sup>, Elisabeth Akoh Hove<sup>2</sup>, Morten Boberg Larsen<sup>2</sup>, and Hao Wu<sup>1</sup>

<sup>1</sup>Department of Chemical Engineering, Technical University of Denmark, 2800 Kgs. Lyngby, Denmark  
E-mail: [fza@kt.dtu.dk](mailto:fza@kt.dtu.dk), URL: <http://www.kt.dtu.dk>

<sup>2</sup>Haldor Topsøe, 2800 Kgs. Lyngby, Denmark

### Introduction

Catalytic cracking of sugars in a circulating fluidized bed (CFB) system is a novel technology for producing intermediary oxygenate products that can be further converted to a variety of bio-based chemicals. The technology has the potential to enable economically and environmentally sustainable production of bio-based chemicals.

The hydrodynamics of such CFB system are very complex and play a critical role in successful operation of the plant. Hence, to support the design of the plant as well as the development and scaling-up of the technology, an in-depth understanding of the hydrodynamics is needed. Computational fluid dynamics (CFD) modeling enables prediction of the hydrodynamic behavior of the gas-solid system and bridging between pilot- and commercial-scale.

### Modeling of system hydrodynamics

Cracking of sugars is performed in a similar manner as the well known fluid catalytic process in which petroleum crude oils is converted into e.g. gasoline using solid heterogeneous catalysts. In the sugar cracking process an aqueous sugar solution is fed into the reactor and exposed to the solid catalyst particles circulating in the system by a fluidizing gaseous medium to increase mixing and reactivity. The CFB system is of a dual fluidized bed (DFB) configuration, consisting of a reactor and a regenerator loop. Each loop is comprised of a riser, primary- and secondary cyclones, a bubbling bed, and a transfer line for connecting the two loops. A stripper section is located vertically below the regenerator bubbling bed. Accurate prediction of the system behavior under cold-flow, inert conditions, without the presence of sugar feedstock, is an important predecessor to modeling the reactive system in which temperature distributions, yields, conversion rates, regeneration efficiency etc. are of key interest. The high loading of catalyst particles requires accurate modeling of interparticle forces and the interaction between catalytic particles and the fluidizing medium, historically proven a difficult and costly task [1].

Three-dimensional computational particle fluid dynamics (CPFD) simulations are conducted based on the Eulerian-Lagrangian multiphase particle-in-cell (MP-PIC) method to predict the hydrodynamic behavior of a cold-flow pilot-scale CFB system at the Technical University of Denmark. The MP-PIC method is a hybrid Eulerian-Lagrangian approach that adopts an Eulerian description of the fluidizing medium and a Lagrangian description of the catalyst particles.

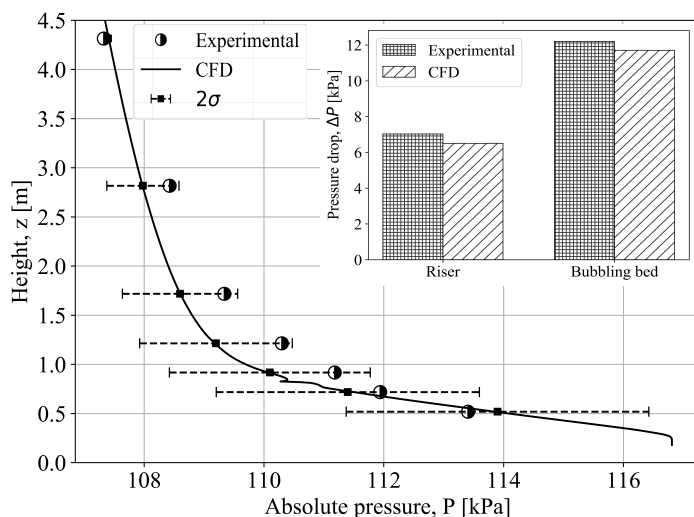


**Figure 1:** Temporally and cross-sectionally averaged absolute pressure  $P$  plotted across the height  $z$  of reactor riser and compared to experimental findings. The bar plot compares the numerically predicted and experimentally observed total pressure drops across the reactor riser and reactor bubbling bed.

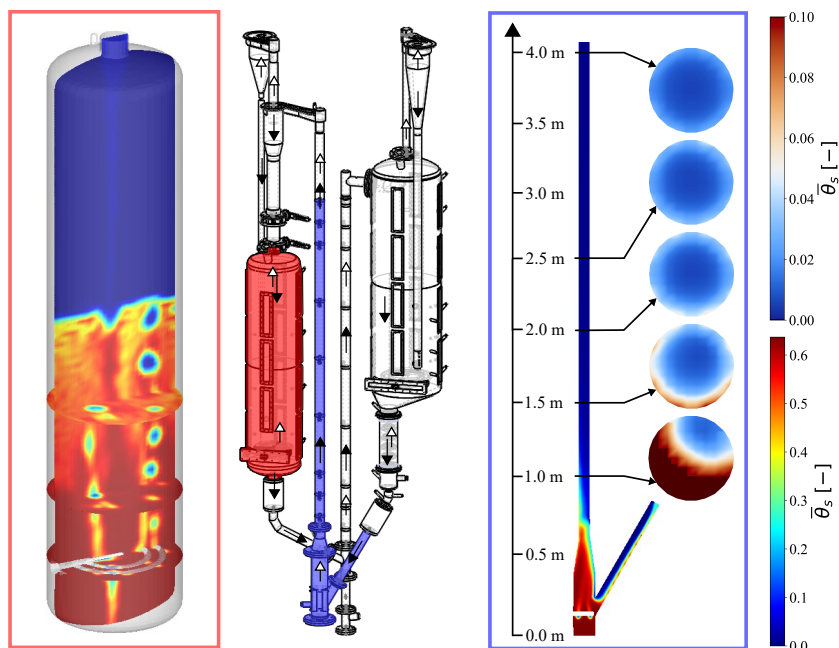


**Figure 2:** Isometric sketch of the pilot-scale DFB system with air and particle flow patterns indicated by empty and filled arrow heads, respectively. Instantaneous solids volume fraction distribution in reactor bubbling bed (red subsystem) and temporally averaged solids volume fraction distribution in reactor riser (blue subsystem) is shown on vertical planes through the geometric centers and horizontal planes at different heights.

Detailed information on the hydrodynamic behavior of the system in terms of particle velocities, residence times, as well as voidage and pressure distributions throughout the system are obtained and analyzed using a segregated modeling approach, decoupling the major parts of the system. The segregated method requires several subsystem simulations to be performed for achieving physical inflow conditions at the subsystem boundaries, improving modeling accuracy while reducing overall computational time and demands [2].

Comparison of CPFD predictions with experimental data on the cold-flow gas-solid pilot-scale model is conducted in terms of pressure distributions throughout the system. Fig. 1 compares the numerically estimated and experimentally determined pressure drop across the height of the reactor riser. The results demonstrate a promising ability of the model to capture the overall behavioral trends of the DFB system.

The qualitatively predicted behavior of the riser depicted in Fig. 2 is in line expectations of [3], showing a dense bottom region and a dilute top region. Additionally, the expected core-annulus solids concentration profile in the riser is predicted by the model. In accordance with findings of [4], no down flow of solids near the riser wall is observed in the model, as otherwise expected [3]. Accurate modeling of interphase drag force has proven to salvage this encountered problem [5].

## Conclusion

A preliminary study into the cold gas-solid flow in a pilot-scale dual fluidized bed system is conducted using a CFD model that incorporates an Eulerian-Lagrangian formulation of the continuum and disperse phase. The segregated modelling approach allows for acceptable prediction of the overall pressure drops of each system, directly related to the fluidization behavior. Additional efforts are needed to capture local behaviors of the physical system.

Short-sighted further work includes modeling optimizations of each subsystem with respect to e.g. tuning of model parameters, drag modeling, grid- and sub-grid discretization. Longer-term extensions of the model are to include a third (liquid) phase to simulate atomization and evaporation of the aqueous sugar solution required for ensuing introduction of chemical reactions.

## References

- [1] M. Shah, R. Utikar, G. Evans, M. Tade, and V. Pareek. *Chemical Engineering Research and Design* **111**, 403-448 (2016).
- [2] M. Wang, Y. Wu, X. Shi, X. Lan, C. Wang, and J. Gao. *Processes* **7**(5), 306 (2019).
- [3] F. Berruti, J. Chaouki, L. Godfroy, T. Pugsley, and G. Patience. *The Canadian Journal of Chemical Engineering* **73**, 579-602 (1995).
- [4] S. Rodrigues, A. Forret, F. Montjovet, M. Lance, and T. Gauthier. *Powder Technology* **283**, 519-529 (2015).
- [5] B. Lu, N. Zhang, W. Wang, J. Chiu, and C. Kang. *AIChE* **59**(4), 1108-1117 (2013).



## Flow characterization inside the nozzle of an industrial printhead

Yogesh Jethani<sup>1</sup>, Tim Segers<sup>1</sup>, Marc van den Berg<sup>2</sup>, Hans Reinten<sup>2</sup>, Youri de Loore<sup>2</sup>, Michel Versluis<sup>1</sup>, and Detlef Lohse<sup>1</sup> <sup>1</sup>Physics of Fluids Group and Max Planck Center Twente, MESA+

Institute and J. M. Burgers Centre for Fluid Dynamics, Faculty of Science and Technology, University of Twente, Enschede, Netherlands

E-mail: y.j.jethani@utwente.nl, URL: <https://pof.tnw.utwente.nl>

<sup>2</sup>Océ Technologies B.V., Venlo, Netherlands

### Introduction

Piezo-acoustic inkjet printing remains one of the most prevalent drop-on-demand inkjet printing methods due to its high reproducibility and precision. However, this highly reliable process is sometimes disturbed by entrainment of bubbles in the ink channel. Entrained bubble nuclei diffusively grow within the inkjet channel due to rectified diffusion. At some point, the pressure pulse is completely compensated by the compression-expansion of the bubble, and hence it is not strong enough to jet out the droplets, resulting in acute nozzle failure. In this experimental study, we aim to characterize the flow inside the inkjet nozzle, and focus especially on the changes in the flow leading to the nucleation of bubbles [1,2].

### Motivation to study flow structures inside the nozzle

Earlier experiments have shown that slight modifications of the printhead geometry and actuation pulse lead to more stable jetting. Specifically, it has been found that more stable jetting is achieved via a multi-component actuation pulse as compared to jetting using a trapezoidal pulse. Furthermore, experimental studies have shown that the nozzle geometry highly influences jet stability. This study aims to quantitatively understand the changes in flow structures inside a nozzle for varying nozzle shapes and pulse shapes. From this, qualitative analysis is made to investigate how these altered flow structures alter the probability of the occurrence of bubble nuclei.

### Experimental setup

The experiments employ a micro-particle image velocimetry setup to measure the flow inside the nozzle. The flow field is measured by capturing stroboscopic sequences of image pairs of the microfluidic inkjet nozzle. Thus, the property of high reproducibility of the flow inside the nozzle is exploited here to accurately and reliably measure the fluid field with micrometer spatial resolution and sub-microsecond temporal resolution.

### Acknowledgements

This work is part of the Industrial Partnership Program number i43, of the Foundation for Fundamental Research on Matter (FOM) supported by the Dutch Organization for Scientific Research (NWO). The research was co-financed by Océ Technologies B.V., University of Twente, and Eindhoven University of Technology.

### Conclusion

This work aims to quantitatively understand the stabilization of the jetting process by accurate measurement of the flow inside the nozzle. The results potentially lead to better optimization of the nozzle shape and design of the piezo elements to produce more stable jets, and at the same time provide hints on what leads to the entrainment of air inside the nozzle.

### References

- [1] H. Wijshoff. *Physics Reports* **491**, 77-177 (2010).
- [2] J. de Jong, G. de Bruin, H. Reinten, M. van den Berg, H. Wijshoff, M. Versluis and D. Lohse. *Journal of the Acoustical Society of America* **120**, 1257-1265 (2006).





## Experimental flow visualization of a flow diverting stent in a popliteal aneurysm

L. van de Velde<sup>1,2,3</sup>, M.M.P.J. Reijnen<sup>2,3</sup>, M. Versluis<sup>1</sup>, J. Tessarek<sup>4</sup> and E. Groot Jebbink<sup>2,3</sup>

<sup>1</sup>Physics of Fluids, TechMed Centre, University of Twente, Enschede, The Netherlands

E-mail: [l.vandavelde@utwente.nl](mailto:l.vandavelde@utwente.nl)

<sup>2</sup>M3i Multi-Modality Medical Imaging, TechMed Centre, University of Twente, Enschede, The Netherlands

<sup>3</sup>Department of Surgery, Rijnstate Hospital, Arnhem, The Netherlands

<sup>3</sup>Department of Vascular Surgery, Bonifatius Hospital, Lingen, Germany

### Introduction

An aneurysm is a local dilatation of an artery, which is prone to rupture or thrombosis due to flow disturbances. These blood clots may accumulate, grow and block blood flow through the aneurysm, or they can dislodge and obstruct downstream vessels. A flow diverting stent, a cylindrical dense metallic mesh, can be deployed to redirect blood flow and reduce flow velocities in the aneurysm, promoting thrombosis and shrinkage of the aneurysm. For intracranial aneurysms, where the arterial wall typically bulges out from a confined wall segment, flow diverters have been investigated in experimental and numerical studies and are routinely used in clinical practice [1].

For popliteal aneurysms, however, flow conditions are significantly different and clinical data is limited, with only one pilot performed in 12 patients [2]. The popliteal artery is the artery traversing the knee, and aneurysms in this region are typically circumferential in nature [3]. Second to the circumferential bulge which alters the flow dynamics, blood flow in this region is highly pulsatile with a phase of bulk flow reversal. To investigate the effectiveness of the flow diverter concept in these conditions, flow profiles were investigated in six phantoms of a popliteal aneurysm.

### Materials & Methods

Six transparent silicone elastomer models were created and integrated in an experimental flow set-up that reproduced physiologic pulsatile flow cycles. These models covered two simplified anatomies (Fig. 1) and three stent configurations (no stent, single stent and dual stent lining in the aneurysm). The flow set-up consisted of a pulsatile piston pump connected to the inlet and a resistive and compliant element at the outlet, which were tuned to pump a Newtonian blood mimicking fluid at physiologic flow rates and pressures through the phantoms (mean inlet  $Re=55$ , max  $Re=400$ ).

Flow in a plane covering the aneurysm was captured at 2000 frames per second, after which the unsteady flow patterns were extracted with particle image velocimetry. Flow velocities, shear rate and wall shear stress in an aneurysm area outside of the flow diverter stent were compared between the different models, as these affect the thrombosis process in the aneurysm.

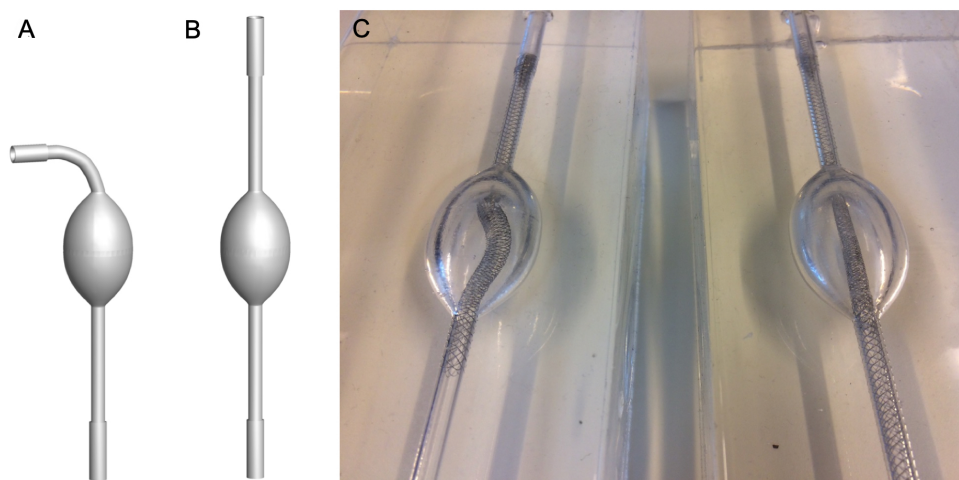


**Figure 1:** The popliteal aneurysm phantoms. (A) Bent inlet trajectory. (B) Straight inlet trajectory. (C) The straight inlet model treated with a single layer stent (left) and a dual layer stent (right), which follow a helical and straight trajectory, respectively.

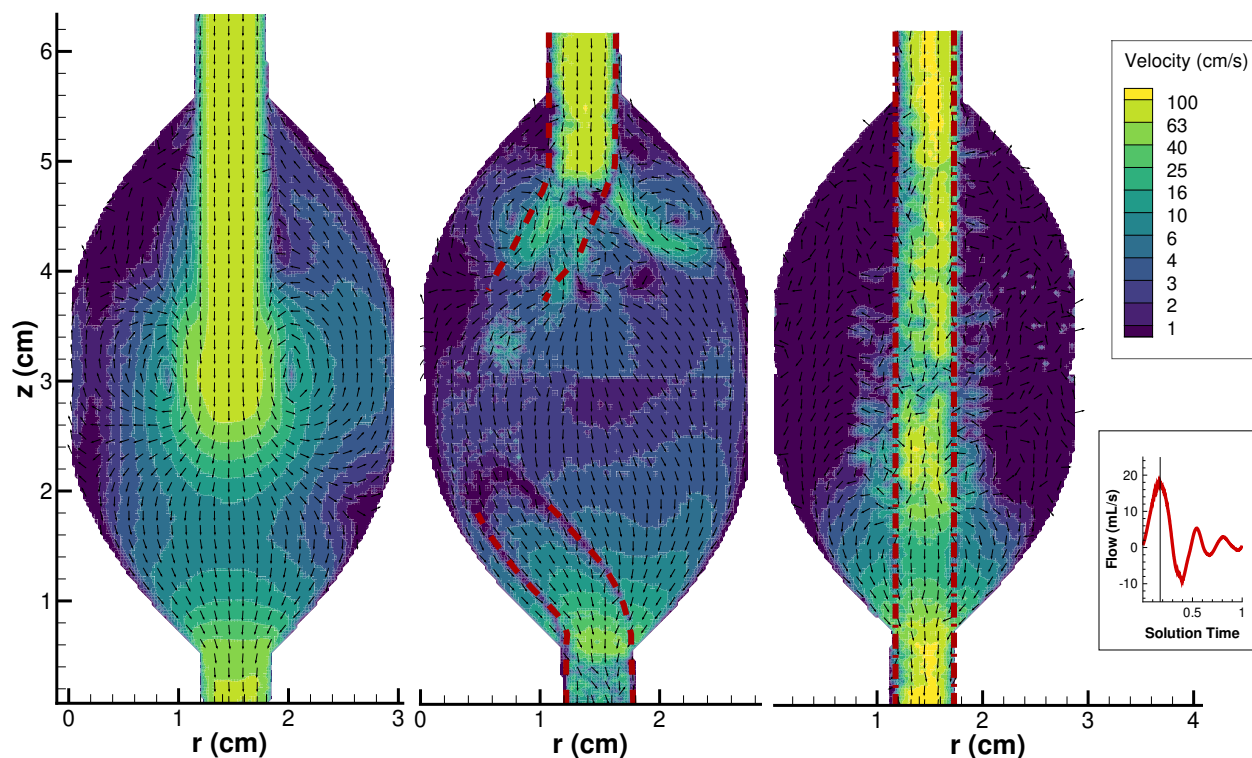


**Figure 2:** Velocity vector and contour plots during peak forward flow in the straight inlet models. From left to right: control, single layer (dashed red line) and double layer (dash-dot red line) stent. The single layer stent is partly out-of-plane due to its helical trajectory.

## Results

The bulk flow reversal of the pulsatile boundary condition led to strong interactions between forward and backward jets in the aneurysm. The forward jet was successfully confined within the flow diverting stents, especially for the double layer stent (Fig. 2). In most models the backward jet, however, was deflected into the aneurysm by the unceasing momentum of the forward jet. In the bent inlet model, a large scale vortex was present in the unstented model, which was continuously fed by the alternating forward and backward jets. This aneurysm-scale vortex was no longer present after the introduction of a flow diverter.

The introduction of a flow diverter stent led to a 2x reduction of aneurysm velocities for single-layer stents, and a 4x reduction for double layer stents, with higher reduction factors for the bent inlet model. Shear rates in the aneurysm were significantly reduced in the bent inlet model by the flow diverters due to breakdown of the large scale vortex. For the straight inlet model, shear rates were less strongly reduced by the flow diverter due to increased shear rates at zones of jet protrusion out of the stent. Wall shear stress of the unstented aneurysm wall was 3-4x lower in the stented models compared to unstented models.

## Conclusion

This experimental study demonstrates that the flow diverter stent is capable of providing a 2-5 times reduction of blood flow velocity in popliteal aneurysms, with the strongest reductions for a double layer stent. Especially forward flow during systole is effectively diverted through the stents, promoting flow stasis in the aneurysm. Backward flow during flow reversal, in contrast, is less successfully diverted, highlighting the importance of the biphasic flow commonly present in popliteal aneurysms. Nonetheless, both flow velocities, shear rates and wall shear stress were strongly reduced by the flow diverter, supporting its clinical use in terms of its fluid mechanical effects.

## References

- [1] Y.J. Alderazi, D. Shastri, T. Kass-Hout, C.J. Prestigiacomo and C.D. Gandhi. *Stroke Research and Treatment* **2014**, 415653 (2014).
- [2] J. Tessarek. *Zentralblatt Chirurgie* **140**, 535-541 (2015).
- [3] R.B. Galland. *Annals of the Royal College of Surgeons of England* **89**, 466-471 (2007).



## Controlled solvent exchange in a porous material: Experiment & theory

Yanshen Li<sup>1</sup>, Steven Chong<sup>1</sup>, Hanieh Bazayr<sup>2</sup>, Rob. G. H. Lammertink<sup>2</sup>, Xuehua Zhang<sup>3,1</sup>, and Detlef Lohse<sup>1,4</sup>

<sup>1</sup>Physics of Fluids group, Max-Planck Center Twente for Complex Fluid Dynamics, University of Twente, Enschede, The Netherlands

E-mail: yanshen.li@utwente.nl

<sup>2</sup>Soft Matter, Fluidics and Interfaces (SFI), University of Twente, Enschede, The Netherlands

<sup>3</sup>Department of Chemical and Materials Engineering, University of Alberta, Edmonton, Canada

<sup>4</sup>Max Planck Institute for Dynamics and Self-Organization, 37077 Göttingen, Germany

### Introduction

Solvent exchange is a bottom up method to generate micro- and nanodroplets by nucleation & growth out of an oversaturated solution [1]. In solvent exchange, a good solvent of the target droplet component is replaced by a poor solvent. A typical example is an oil saturated aqueous ethanol solution being replaced by oil saturated water. Upon contact of the ethanol & water solution, the two solvents start to mix with each other not only by advection but also by diffusion, since the two solvents are mutually miscible. In the mixture in between, the solubility of oil is lowered, and the subsequent oversaturation leads to droplet nucleation and growth [2].

It has been found that for exchange in a microchannel, the average total volume of the droplets nucleated at the wall increases with the Péclet number  $Pe$  as  $\propto h^3 Pe^{3/4}$ , when varying the flow rate [2]. Later it was found that the channel geometry and initial oil concentration also influences the size of the nucleated droplets [3,4].

Here we experimentally and analytically study the solvent exchange in a Hele-Shaw cell type channel with a porous region in the center. For all the porosities tested, it is found that all of the oversaturated oil nucleates into droplets and gets trapped by the porous region, so that the mixture is no longer oversaturated at the end of the porous region. Solvent exchange is performed with various initial oil concentrations and flow rates, and the measured total volume of oil is found to depend on the Péclet number  $Pe$  with a power law exponent about 0.51. To explain this scaling behavior, we develop an analytical solution of the total volume of oil  $V$  by spatially integrating the oil oversaturation, which is found to be in a plug-like shape because of Taylor-Aris dispersion [5].  $V$  is found to increase as  $\propto Pe^{1/2}$ , and the prefactor, which takes into account the initial oil concentration, can collapse the data onto one curve. Our findings will help to further optimize solvent exchange process in confined geometries.

### Experimental setup

Decane – the oil – saturated aqueous ethanol solution (water) serves as the good (poor) solvent. The flow rate, measured by a flowmeter, is varied by changing the driving pressure to change  $Pe$ .

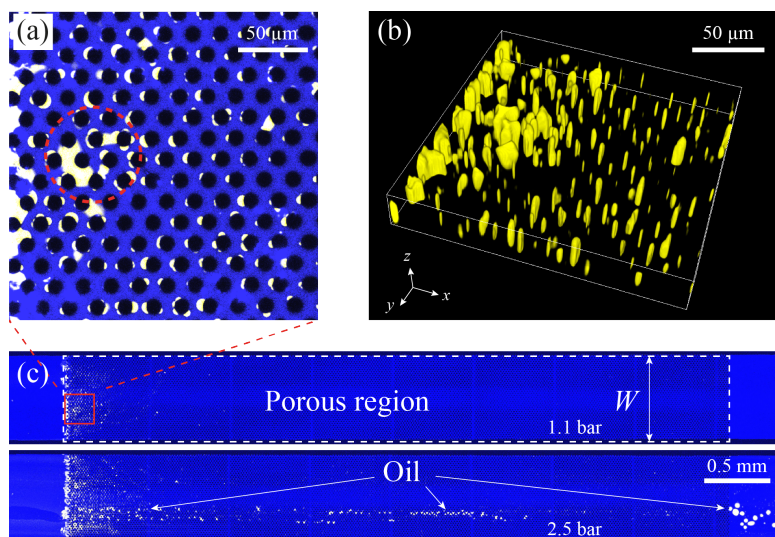


**Figure 1:** Oil morphologies when the solvent exchange is finished (porosity 0.7). (a) Typical oil morphology at the entrance of the porous region at driving pressure 1.10 bar. Yellow signals oil, blue signals water, and black the pillars. Oil nucleates quite randomly on nearly every pillar, but there is more oil near the inlet. Oil droplets can be large enough to fill the gaps between pillars, as highlighted by the red-dotted circle. (b) 3D confocal image of the morphology of oil in the same area, resolution is  $0.43 \times 0.43 \times 1 \mu\text{m}^3$  in the  $x$ ,  $y$  and  $z$  direction. (c) Typical oil morphology in the whole porous region, with driving pressures at 1.10 bar and 2.48 bar.

### Theoretical model

In the mixture between the two solvents, the solubility of oil is a function of space, time, and initial oil concentration  $c_{o,s}(\vec{x}, t, c_{o,A})$ , which is smaller than the actual oil concentration  $c_o(\vec{x}, t, c_{o,A})$ . The total volume of oil  $V$  can be calculated by integrating the oversaturation over the entire channel volume  $\Omega$ , at the time  $t$  just before the oversaturation pulse reaches the porous region:

$$V(t, c_{o,A}) = \frac{1}{\rho_o} \int_{\Omega} [c_o(\vec{x}, t, c_{o,A}) - c_{o,s}(\vec{x}, t, c_{o,A})] d\vec{x} \quad (1)$$

where  $\rho_o = 730 \text{ kg/m}^3$  is the density of oil.

By assuming no ternary diffusion and equal diffusivity of ethanol and oil in the mixture:  $D_e = D_o \equiv D$ , the oversaturation can be expressed as a function of the local ethanol concentration  $c_e$ :

$$c_o(\vec{x}, t, c_{o,A}) - c_{o,s}(\vec{x}, t, c_{o,A}) = c_o[c_e(\vec{x}, t, c_{e,A})] - c_{o,s}[c_e(\vec{x}, t, c_{e,A})] \quad (2)$$

Note that the initial oil concentration  $c_{o,A}$  is also represented by the initial ethanol concentration  $c_{e,A}$ .

From Taylor-Aris dispersion [Fig.2(a)], the ethanol concentration is like a plug, its distribution as a function of space, time and initial solvent concentration  $c_{e,A}$  is obtained:

$$c_e(x, t, c_{e,A}) = \frac{1}{2} [1 + \text{erf}(\kappa x_1)] \cdot c_{e,A} \quad (3)$$

where  $x_1 = x - \bar{u}t$  is the distance to the central position of the plug. Wavenumber  $\kappa = 1/(2\sqrt{kt})$  is inversely proportional to the length of the plug  $L_p$ .  $t = L/\bar{u}$  is the time when the oversaturation plug reaches the porous region, with  $L$  being the length of the channel.  $k = h^2\bar{u}^2/(210D)$  for flow in a thin square channel with height  $h$ .

Substituting Eq.2 and Eq.3 into Eq.1, we obtain:

$$V(c_{e,A}) = s(c_{e,A}) \cdot Wh^{\frac{3}{2}}L^{\frac{1}{2}} \cdot Pe^{\frac{1}{2}} \quad (4)$$

where

$$s(c_{e,A}) = \frac{2}{\sqrt{210}} \frac{1}{\rho_o} \int_{-\infty}^{\infty} [c_o(\kappa x_1, c_{e,A}) - c_{o,s}(\kappa x_1, c_{e,A})] d(\kappa x_1) \quad (5)$$

is a dimensionless prefactor which takes into account the ternary system in use and the influence of the initial solution composition  $c_{e,A}$ .  $W$ ,  $h$ , and  $L$  are the width, height and length of the channel, respectively. Péclet number  $Pe = \bar{u}h/D$ .

### Conclusion

The model fits well with the experimental results: Measured  $V$  increases as  $\propto Pe^{1/2}$ , as shown in Fig.2(b); and the calculated prefactor  $s$  can collapse all the data onto one curve, as shown in Fig.2(c).

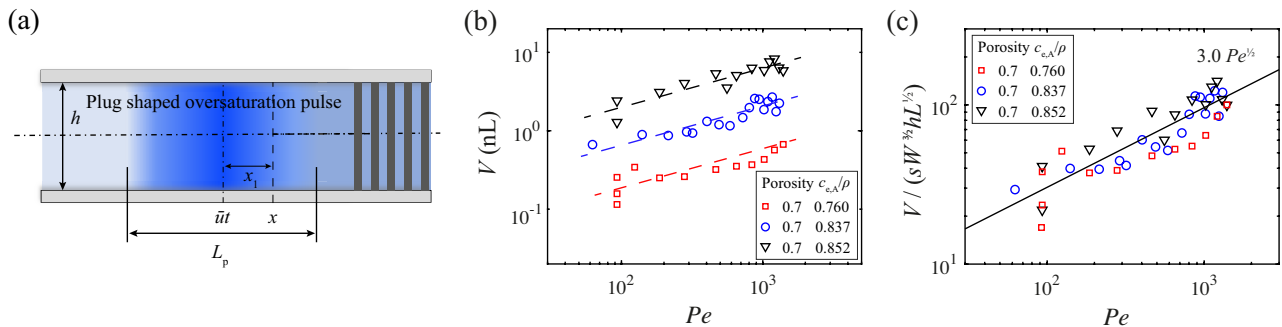


**Figure 2:** (a) Plug shaped oversaturation pulse. (b) Measured  $V$  as a function of  $Pe$ . (c)  $V$  non-dimensionalized by the calculated prefactor  $s$  and channel geometry as a function of  $Pe$ .

### References

- [1] D. Lohse and X. Zhang. *Rev. Mod. Phys.* **87**, 981 (2015).
- [2] X. Zhang, Z. Lu, H. Tan, L. Bao, Y. He, C. Sun and D. Lohse. *Proc. Natl. Acad. Sci. U.S.A.* **112**, 9253-9257 (2015).
- [3] H. Yu, S. Maheshwari, J. Zhu, D. Lohse and X. Zhang. *Lab Chip* **17**, 1496-1504 (2017).
- [4] Z. Lu, S. Peng, X. Zhang. *Langmuir* **32**, 1700-1706 (2016).
- [5] G. I. Taylor. *Proc. R. Soc. London, Ser. A*, 186-203 (1953).



## From zonal flow to convection rolls in two-dimensional Rayleigh-Bénard convection with free-slip plates

Qi Wang<sup>1,2,\*</sup>, Zhen-Hua Wan<sup>2</sup>, De-Jun Sun<sup>2</sup>, Roberto Verzicco<sup>3,4,1</sup>, Detlef Lohse<sup>1,5</sup>, and Richard J. A. M. Stevens<sup>1</sup>

<sup>1</sup>Physics of Fluids Group and Max Planck Center Twente for Complex Fluid Dynamics, MESA+ Institute and J. M. Burgers Centre for Fluid Dynamics, University of Twente, P.O. Box 217, 7500AE Enschede, The Netherlands

<sup>2</sup>Department of Modern Mechanics, University of Science and Technology of China, Hefei 230027, China

<sup>3</sup>Dipartimento di Ingegneria Industriale, University of Rome “Tor Vergata”, Via del Politecnico 1, Roma 00133, Italy

<sup>4</sup>Gran Sasso Science Institute - Viale F. Crispi, 767100 L’Aquila, Italy.

<sup>5</sup>Max Planck Institute for Dynamics and Self-Organization, 37077 Göttingen, Germany

\*E-mail: [q.wang-1@utwente.nl](mailto:q.wang-1@utwente.nl)

### Introduction

Large scale zonal flows, which generate strong horizontal winds, can be observed in many natural phenomena and industrial processes, typical examples include zonal flow in giant planets such as Jupiter’s atmosphere, and the alternating jet streams found in the oceans. In toroidal tokamak devices, zonal flows in the poloidal direction are crucial to confine plasmas magnetically. In order to get a better understanding on the physics of zonal flows we study such flows in two-dimensional (2D) Rayleigh-Bénard convection (RBC). RBC is the canonical problem in which a layer of fluid is heated from below and cooled above, and zonal flows are formed in this system when free-slip boundary conditions at the plates are used in a 2D periodic domain. The main control parameters of the system are the Rayleigh number  $Ra$ , a measure for the dimensionless temperature difference, and the Prandtl number  $Pr$ , which is defined as the ratio of momentum diffusivity to thermal diffusivity. The aspect ratio  $\Gamma$  is defined as the width over the height of the system.

Goluskin *et al.* [1] studied zonal flow in 2D RBC with free-slip plates for fixed aspect ratio  $\Gamma = 2$  over a wide range of parameters ( $10^3 \leq Ra \leq 10^{10}$  and  $0.5 \leq Pr \leq 30$ ). However it is still unknown whether zonal flow can also be observed in very large aspect ratio cells, which are the relevant configurations for many geophysical flows. To address this question we study 2D RBC with free-slip plates over a wide range of aspect ratios  $\Gamma$  ( $1 \leq \Gamma \leq 64$ ) for  $Ra = 10^6$  to  $Ra = 10^9$  and from  $Pr = 1$  to  $Pr = 30$  using direct numerical simulations (DNS). The simulations are performed using the AFID code [3].

### Results

We find that zonal flow disappears when the horizontal extent of the system is larger than a critical value, which depends on  $Ra$  and  $Pr$ , see figure 1. Panel (a) shows the  $Pr - \Gamma$  phase diagram for  $Ra = 10^8$  and panel (b) the  $Ra - \Gamma$  phase diagram for  $Pr = 10$ . For small periodic domains we only observe zonal flows (black circles in the phase diagrams). For intermediate aspect ratios we find a regime of bi-stability (red squares in the phase diagrams) in which, depending on the initial conditions, both the zonal flow and the convection roll states can occur. The different states are triggered by carefully selecting the initial conditions. Once the zonal or convection roll state is established in the bi-stable regime it is very stable and long simulations intervals are used to ensure that each state remains stable for at least 4000 free fall time units. During this time we observe no switching between the zonal and convection roll state, which means that there is a strong hysteresis effect in the bi-stable regime. For even larger aspect ratios (blue diamonds in the phase diagrams) we find that only the convection roll state is stable and zonal flows are not stable anymore.

Another interesting observation is the long term stability of different flow states in large aspect ratio cells, see figure 2. The figure shows instantaneous temperature fields for zonal flow, and all the observed convection roll states, for  $Ra = 10^8$ ,  $Pr = 10$ , and  $\Gamma = 16$ . Each state is stable for at least 4000 free fall time units and are triggered by carefully selecting the initial condition for each case. Remarkably, the flow state has a huge influence on the obtained heat transfer, which in dimensionless form is indicated by the Nusselt number  $Nu$ . For zonal flow the heat transfer is lowest, because the flow is dominated by horizontal motions and the vertical transport is suppressed. Next to zonal flow we find different convection roll states, in which the horizontal extend of the rolls compared to the height of the convection cell varies from 8 (figure 2b) to 4/3 (figure 2g). The established roll state has a huge effect on the heat transfer in the system. The heat transfer increases with the number of

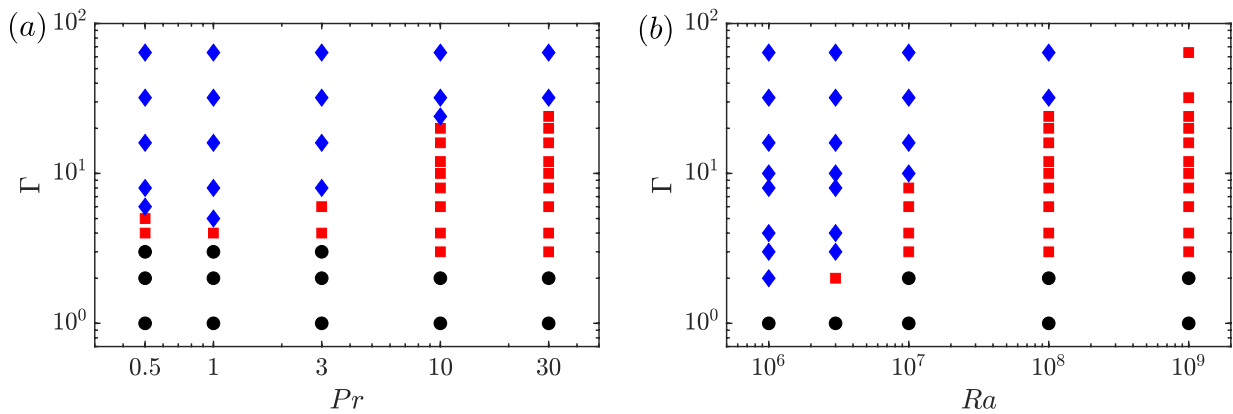


**Figure 1:** (a)  $Pr - \Gamma$  phase diagram for  $Ra = 10^8$  and (b)  $Ra - \Gamma$  phase diagram for  $Pr = 10$ . Black circles (●) correspond to only zonal flow, red squares (■) denote coexistence of zonal flow and convection rolls, and blue diamonds (◆) denote only convection rolls.

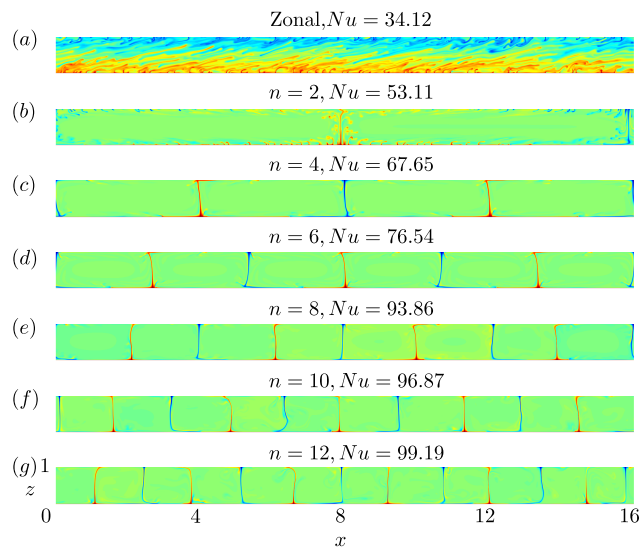


**Figure 2:** Instantaneous temperature fields for zonal flow and different roll states for  $Ra = 10^8, Pr = 10, \Gamma = 16$ . (a) zonal flow. (b) two-roll state. (c) four-roll state. (d) six-roll state. (e) eight-roll state. (f) ten-roll state. (g) twelve-roll state. The roll numbers  $n$  and Nusselt numbers  $Nu$  are also indicated.

rolls, i.e. the reduction of the horizontal extend of each rolls, and varies by as much as 87% for the different states we found, see figure 2. Although there is a huge variation in stable convection roll states it is important to note for  $Ra = 10^8$  and  $Pr = 10$  the horizontal extend of stable rolls varies between roughly 4/3 to 64 times the height of the convection cell (horizontal extend of 64 is observed for  $\Gamma = 128$  cell). The latter is much larger than the size of superstructures observed in 3D RBC with no-slip plates [2], which in part is because free-slip plates can support larger convection rolls than their no-slip counterparts.

### Summary

We study RBC with free-slip plates in 2D periodic domains using DNS. We find that the zonal flow observed in a  $\Gamma = 2$  cell [1] disappears in very large aspect ratio cells, in which we only observe convection roll states. We also observe a bi-stable regime in which, depending on the initial conditions, both zonal flow and convection roll states can be stable. For small aspect ratios only zonal flow is stable. The aspect ratio for which the transition between these different states takes places strongly depends on the Rayleigh number  $Ra$  and Prandtl number  $Pr$  as is indicated in figure 1. In addition, we find that in large aspect ratio cells different convection roll states can be stable. For  $Ra = 10^8$  and  $Pr = 10$  the horizontal extend of stable convection rolls varies roughly between 4/3 and 64 times the height of the convection cell. The heat transfer in the system strongly increases when the horizontal extent of the convection roll is reduced.

### References

- [1] D. Goluskin, H. Johnston, G. R. Flierl, E.A. Spiegel, J. Fluid Mech. **759**, 360-385 (2014).
- [2] R.J.A.M. Stevens, A. Blass, X. Zhu, R. Verzicco, D. Lohse, Phys. Rev. Fluids **3**, 041501 (2018).
- [3] E.P. van der Poel and R. Ostilla-Mónico and J. Donners and R. Verzicco, Comput. Fluids. **116**, 10-16 (2015).



# Spatio-temporal patterns and transport in axisymmetric compressible Taylor Couette flow

Tanumoy Dhar<sup>1</sup>, Pratik Aghor<sup>1</sup>, and Meheboob Alam<sup>1</sup>

<sup>1</sup>Engineering Mechanics Unit, Jawaharlal Nehru Centre for Advanced Scientific Research, Jakkur P.O., Bangalore 560064, India  
E-mail: tanumoydhar@jncasr.ac.in

## Introduction

In the 1880s, Henry Mallock and Maurice Couette independently determined the viscosity of water in an apparatus consisting of two rotating concentric cylinders. Thirty years later, Rayleigh [1] and Taylor [2] demonstrated the instability criterion and transition to Taylor vortex flow (TVF) from the circular Couette flow (CCF). During the past hundred years, the incompressible Taylor-Couette (TC) flow has emerged as one of well-studied problem in fluid mechanics to understand instabilities, pattern formation and the laminar-turbulent transition. The present work focuses on the compressible analog of TC flow which is relevant in accretion disk flows that admit high Mach number ( $Ma$ ). We present numerical results on an axisymmetric TC flow of a compressible gas with the inner cylinder rotating [3,4]. The aim of this work is to study the effects of compressibility and curvature on the flow patterns and transport in the  $(Re, Ma)$  and  $(Re, \eta)$  plane, where  $Re$  is the Reynolds number based on the rotation rate of the inner cylinder and  $\eta (= r_i/r_o)$  is the radius ratio of two cylinders.

## Present Work

We seek solutions of azimuthal invariant  $[\partial/\partial\theta(\cdot) = 0]$ , time-dependent compressible Navier-Stokes equations along with the continuity and energy equations for a monoatomic perfect gas as a function of  $Re$ ,  $Ma$  and  $\eta$ . A related work on linear stability of compressible TC flow has been carried out by Welsh *et al.* [5]. The primary bifurcation from the pure azimuthal CCF leads to the well-known TVF, and the phase diagrams of the patterns are constructed in the  $(Re, Ma)$  and  $(Re, \eta)$  planes. A new time-dependent, axially propagating, axisymmetric flow state, called the Travelling wave solution (TWS), has been identified in wide gap ( $0.3 \leq \eta \leq 0.6$ ) TC cells at higher  $Re$  (beyond the primary bifurcation), see figure 1. We also find that the TWS returns back to TVF for certain  $Re$  and  $\eta$  combinations, and is identified in a distinct region in the phase space. Time series have been analysed for the axial velocity ( $w$ ) and radial velocity ( $u$ ) measured at the midgap between the inner and outer cylinders at the mid-height of the computational domain. The single-sided amplitude spectrum reveals the existence of harmonics and sub-harmonics, and the corresponding phase portraits on  $(u, w)$  plane show a distinct change in its topology with increasing  $Re$ .

The effect of compressibility ( $0.1 \leq Ma \leq 3$ ) on critical Reynolds number has been studied. In general, the onset of both primary and secondary bifurcations are delayed with increase of  $Ma$ . It is found that at a constant  $Re$ , with increasing  $Ma$ , a strong density stratification occurs along the radial direction which affects the specific angular momentum, ( $\mathcal{L} = \rho vr$ ), locally causing  $\frac{d\mathcal{L}}{dr} > 0$  for  $Ma \geq 1.5$ . Figure 2 displays non-monotonic radial profiles of  $\mathcal{L}$  for three different  $Re$ . In the CCF regime, the flow between two cylinders can be divided into ‘‘Rayleigh-stable’’ (stable to axisymmetric inviscid perturbations) and ‘‘Rayleigh-unstable’’ parts [1]. With increasing  $Re$ , at  $Ma \geq 2$ , the radial profiles of  $\mathcal{L}$  tend towards a bimodal distribution. Interestingly, for a given  $Re$ , the radial profiles of  $\mathcal{L}$  for different  $Ma$  cross each other at a fixed radial location ( $r_{\mathcal{L}}$ ) from the inner cylinder;  $r_{\mathcal{L}}$  is found to be invariant in CCF regime and decreases in TVF regime with increasing  $Re$ .

The effective Nusselt number ( $Nu_\omega$ ) in compressible TC flow has been calculated using the local angular momentum current ( $J^\omega$ ), as described in Ref. [6]. The  $Nu_\omega - Re$  plots indicate that  $Nu_\omega \propto Re^0$  holds in the CCF regime of compressible TC, and  $Nu_\omega \propto Re^\beta$  scaling holds in the TVF regime (around the bifurcation point) with  $\beta \sim 1$ .

## Conclusion

Direct numerical simulations of compressible TC flow were carried out. The compressibility primarily affects the radial density profiles by causing an accumulation of mass near the outer cylinder. This radial stratification of density gives rise to increased shear viscosity near inner cylinder creating a local maxima in radial temperature profile. The analyses of axial and radial density ( $\rho$ ), and velocity ( $u, v, w$ ) profiles reveal that the compressibility diminishes the radial, azimuthal and axial transports. At high  $Re$ , we found a new axially-propagating solution (TWS) which has not been previously reported and attribute it to the compressibility of the gas. A summary of all the observed flow

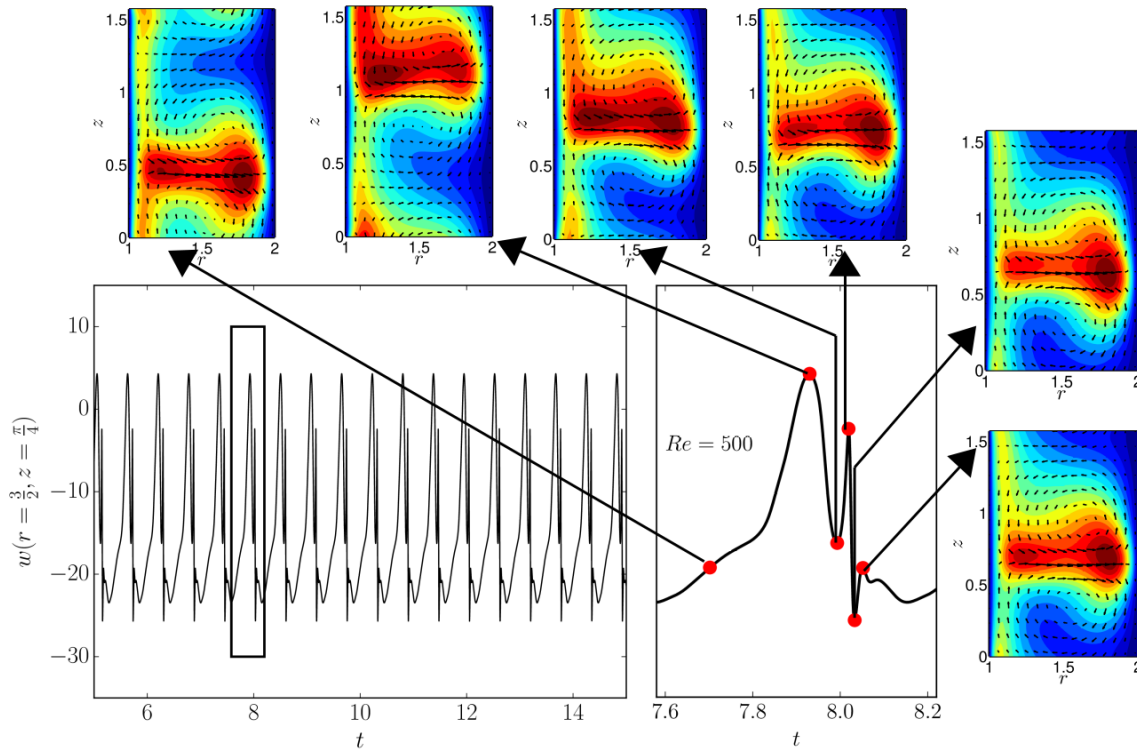


**Figure 1:** Time dependence of axial velocity ( $w$ ) at mid-height and mid-plane of the computational domain; the right panel is an enlargement of the left figure showing a single wave. Velocity vectors on  $(r, z)$  plane superimposed on temperature contour plots are displayed in top and right panels.

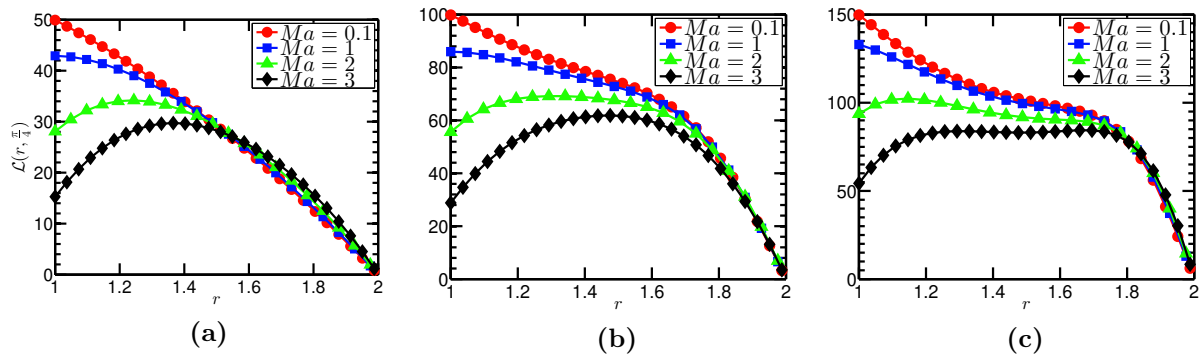


**Figure 2:** Effect of compressibility on mid-height radial profiles of angular momentum for (a)  $Re = 50$  (CCF); (b)  $Re = 100$  (TVF) and (c)  $Re = 150$  (TVF).

patterns are given in  $(Re, Ma)$  and  $(Re, \eta)$  phase-diagram and will be discussed during this workshop.

## References

- [1] Lord Rayleigh. On the dynamics of revolving fluids. Proc. R. Soc. London A. 93 (648), 148-154 (1917).
- [2] G. I. Taylor. Stability of a viscous liquid contained between two rotating cylinders. Philos. Trans. Royal Soc. A. 223, 289-343 (1923).
- [3] T. Dhar, P. Aghor & M. Alam. Spatio-temporal patterns and transport in axisymmetric compressible Taylor-Couette flow. (2019) (*Preprint*).
- [4] P. Aghor. Pattern Formation and Anomalous modes in Axisymmetric, Compressible Taylor-Couette Flow. M.Sc. (Engg.) Thesis (2018), JNCASR, Bangalore.
- [5] S. Welsh, E. Kersalé & C. Jones. Compressible Taylor-Couette flow - instability mechanism and codimension 3 points. J. Fluid Mech. 750, 555-577 (2014).
- [6] B. Eckhardt, S. Grossmann & D. Lohse. Torque scaling in turbulent Taylor-Couette flow between independently rotating cylinders. J. Fluid Mech. 581, 221-250 (2007).



## Dynamics of viscous adhesion : From elongated capillary bridges to fingering instability

Manon L'Estimé<sup>1</sup>, José Bico<sup>1,2</sup>, and Etienne Reyssat<sup>1,2</sup>

<sup>1</sup>Laboratoire de Physique et Mécanique des Milieux Hétérogènes (PMMH) - ESPCI, Paris, France  
E-mail : manon.lestime@espci.fr

<sup>2</sup>CNRS

### Introduction

Fingering instabilities usually occur when a less viscous fluid pushes a more viscous one, as described by the classical Saffman-Taylor instability. However, it has been shown that the inverse situation in which the high viscosity fluid displaces the lower viscosity one is stable. We aim here to present a fingering phenomenon arising when silicone oil penetrates into air of lower viscosity. Indeed, the adhesion of solid surfaces forming a sharp wedge and coated with a viscous liquid occurs through the merging of both adhesive layers. As the adhesion front chases the air and progresses in the narrow gap separating both surfaces, it sometimes undergoes fingering. To explore experimentally this instability, we first address the model problem of a single finger of wetting liquid bridging a bath and a beam placed slightly over the surface of the bath. We then proceed to the description of the fingering instability that occurs when putting two lubricating surfaces in contact.

### Model experiment : Single finger dynamics

We explore the dynamics of a single finger with a simplified model experiment in which a solid beam is placed horizontally above a bath of liquid (see Fig. 1). As a liquid bridge is created at one end of the beam, the bridge spontaneously expands towards the opposite extremity (see Fig. 2). We show that the dynamics of this finger strongly depends on the viscosity of the liquid, on the depth of the pool, and on the gap separating the liquid surface and the overhanging beam.

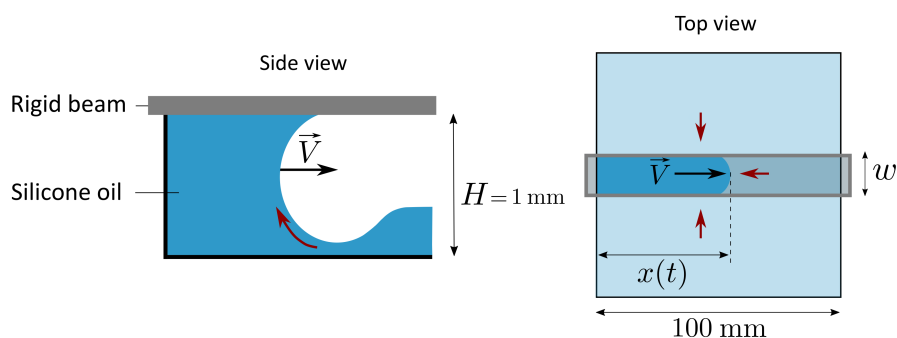


Figure 1 – Schematic of the experimental setup.

### An unexpected fingering instability

We investigate the adhesion between solid surfaces forming a wedge and coated with a viscous fluid (see Fig. 3) which can lead, in some cases, to the formation of finger-like patterns (see Fig. 4). We present how the fingers dynamics is influenced by the angle between the solid surfaces, the amount of liquid available, and the physical properties of the liquid.



**Figure 2** – Successive top views of the experiment :  $h \sim 450 \mu\text{m}$ ,  $\eta = 50 \text{ cSt}$ .

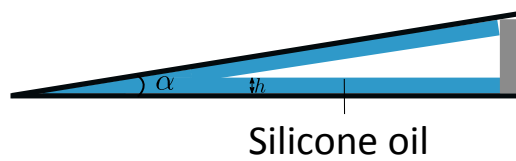


**Figure 3** – Schematic of the experimental setup.

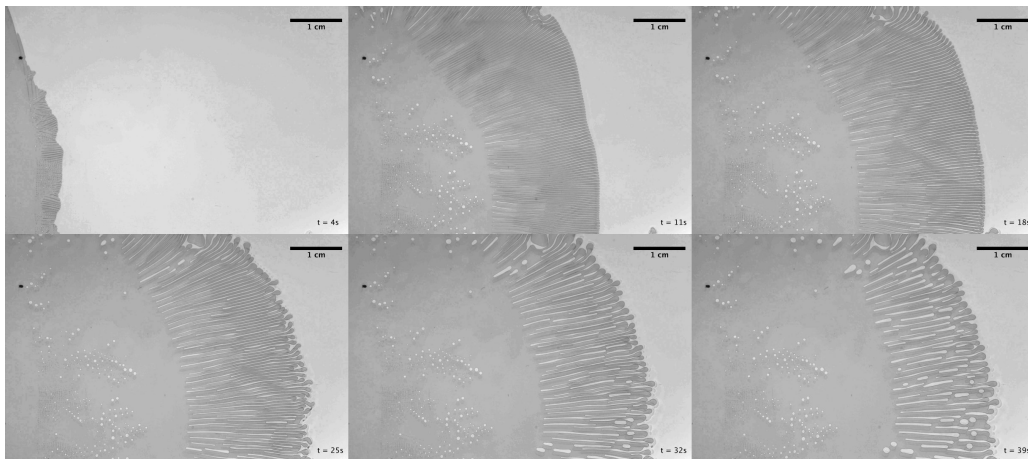


**Figure 4** – Successive top views of the experiment :  $h \sim 30 \mu\text{m}$ ,  $\alpha \sim 0.07^\circ$ .

## Conclusion

We have some interesting results regarding the growth of capillary bridge as well as the formation of fingers in a new configuration and we are glad to present them at the CMiF summer school.

## References

- [1] P. G. Saffman. *J. Fluid Mech.* **176**, 73-94 (1986).
- [2] I. Bihi, M. Baudoin, J. E. Butler, C. Faille and F. oueshtiagh. *Phys. Rev. Lett.* **117**, (2016).



## The complex motion of multi-flagellated bacteria

Maria Tătulea-Codrean<sup>1</sup>, and Eric Lauga<sup>1</sup>

<sup>1</sup>Department of Applied Mathematics and Theoretical Physics, University of Cambridge, Cambridge, United Kingdom

E-mail: [mt599@cam.ac.uk](mailto:mt599@cam.ac.uk), URL: <http://www.damtp.cam.ac.uk/people/mt599/>

### Introduction

The vast majority of motile bacteria exploit chirality in order to break symmetry and generate propulsion at low Reynolds number. Spirochaetes have developed corkscrew-shaped bodies, while other bacteria with simple bodies can assemble and actuate helical appendages called flagella. In the case of multi-flagellated bacteria, the filaments are swept behind the cell body and rotate together in a bundle (Fig. 1a), which leads to a period of straight swimming called a “run”. To change swimming direction, at least one motor must switch its sense of rotation, upon which the associated flagellum will leave the bundle and generate a force imbalance. The subsequent reorientation of the cell is called a “tumble”. The complexity of manoeuvring multiple helical filaments into a coherent bundle, which can be rotated continuously without jamming, is an impressive feat for a single-celled organism, especially since there is no signalling or coordination between the molecular motors actuating them. This problem motivates our contribution to the summer school *Complex Motion in Fluids 2019*.

### The problem of tangling

The ability of multi-flagellated bacteria to bundle and unbundle their flagella is crucial to their run-and-tumble mobility [1]. However, it is surprising that the cell can bundle its flagella without jamming, despite the lack of coordination between molecular motors. This is intriguing because the filaments could, in theory, tangle around each other due to their helical geometry [2]. Yet neither experiments, nor computational studies have reported cases of tangle-induced jamming. Starting from the setup in Fig. 1b, we have established the theoretical conditions under which a pair of rigid helical filaments may tangle, and then compared these constraints with experimental data collected from the literature. Our study suggests that geometric constraints are sufficient to explain why bacterial flagella cannot tangle, therefore increasing the robustness of the bundling process.

### Hydrodynamics of flagellar bundles

Since increasing the number of flagella amplifies the risk of tangling, the obvious question to ask is whether the bacterium obtains a substantial benefit from having multiple flagella. Assuming flagella are randomly distributed on the cell body, increasing their number is expected to reduce misalignment

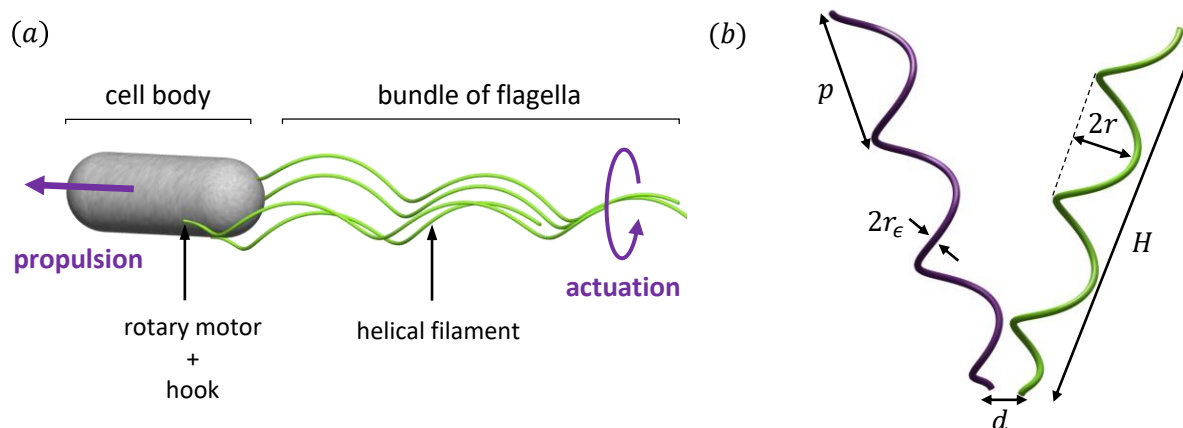


**Figure 1:** (a) Model of a multi-flagellated bacterium. Many species of bacteria, including the widely studied *Escherichia coli* and *Salmonella typhimurium*, propel themselves through viscous fluids by rotating multiple helical filaments, which are connected by a short and flexible hook to molecular rotary motors embedded in the cell wall. (b) Setup of our theoretical model for tangling. We consider a pair of rigid filaments anchored to a plane, and we investigate the necessary conditions under which these two flagella may come from a configuration where they are not intertwined (e.g. pointing away from each other, as they would be at the end of a tumble) into a tangled bundle.

between the axis of the bundle and that of the cell. This in turn would reduce wobbling and lead to smoother trajectories [3]. The impact of multi-flagellarity on the speed and stability of locomotion has also been the subject of a recent computational study [4]. We will discuss further insights coming from our ongoing theoretical work on the problem of hydrodynamic interactions within a bundle of flagella.

### Conclusion

The hydrodynamic benefit of having multiple flagella, as well as the associated risk of geometrical tangling, depend on both the shape and number of flagella. At one extreme, we know that straight flagella could not intertwine, but neither could they propel the cell forward in a viscous fluid. Similarly, one flagellum could never tangle on its own, but neither could it generate a propulsive force as large as a bundle of flagella. We will present some theoretical results about the role of flagellar geometry and number on the robustness of tangle-free bundling and the hydrodynamics of the bundle.

### References

- [1] Z. Qu, F. Temel, R. Henderikx, and K. S. Breuer, *Proc. Natl. Acad. Sci. U.S.A.* **115**, 1707-1712 (2018).
- [2] R. M. Macnab, *Proc. Natl. Acad. Sci. U.S.A.* **74**, 221-225 (1977).
- [3] Y. Hyon, Marcos, T. R. Powers, R. Stocker, and H. Fu, *J. Fluid Mech.* **705**, 58-76 (2012).
- [4] F. T. M. Nguyen, and M. D. Graham, *Phys. Rev. E.* **98**, 042419 (2018).



## Particles at interfaces Formation and erosion of a granular raft

Lagarde Antoine<sup>1</sup>, Josserand Christophe<sup>2</sup>, and Protière Suzie<sup>1</sup>

<sup>1</sup>Sorbonne Université, Centre National de la Recherche Scientifique, UMR 7190, Institut Jean Le Rond d'Alembert, F-75005 Paris, France.

E-mail: antoine.lagarde@dalembert.upmc.fr

<sup>2</sup>LadHyX, CNRS, Ecole Polytechnique, UMR 7646, 91128 Palaiseau, France.

### Introduction

Who has never stared at its cereal bowl during a lethargic breakfast, trying to find the courage to go on with the day, without realizing the intricate physical beauty lying behind the aggregated cereals? The so-called Cheerios effect [1] has many applications, from nature where it is used by fire ants to float, to industry where the aggregation of carefully designed particles serve as the corner stone for the fabrication of objects with a desired microstructure.

Here, we study experimentally the formation and life of an axisymmetric monolayer of dense spherical beads at an oil-water interface, called a granular raft [2]. We first quantify the capillary interaction between two granular rafts and show its dependency with the number of particles in each aggregate. We then focus on the erosion a raft can be subjected to when moving: the raft loses particles during its displacement, which can lead to a modification of the forces experienced. We study this erosion process and deduce the cohesion forces which keep particles together within a raft.

### Interaction between a pair of granular raft

When two identical objects are deposited at an interface, they individually deform the interface. When their respective meniscii overlap, a capillary force is generated and leads to the aggregation of the two entities. For colloidal particles, this interfacial deformation can arise because of non-spherical shapes, surface roughness, or wettability. For larger entities, the main contribution comes from their weight, leading to a motion satisfactorily captured by the linear approximation proposed in 1949 [3]. Good experimental agreement has been found for identical particles, but very few studies describe the interaction between non identical aggregates.

Here, we experimentally study the capillary forces generated by granular rafts, as illustrated in figure 1, for which the vertical deflection of the interface strongly depends on the number of particles they are made of, leading to unusually high capillary forces. In parallel, the viscous drag experienced is also affected by the size of the raft. Thanks to the measured velocity profiles, we derive a model for both the capillary interaction and the drag force, and confirm these experimental results with some numerical simulations for the shape of a raft.

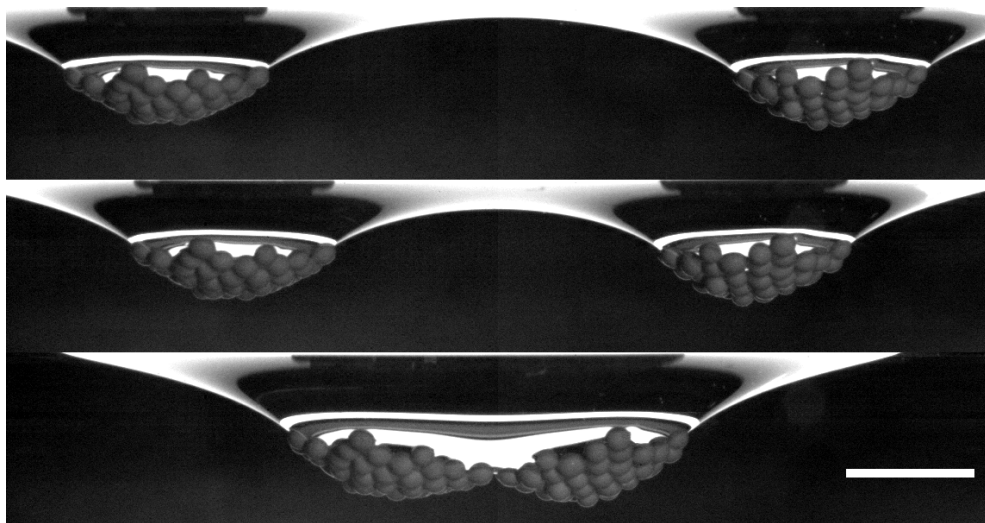


**Figure 1:** Side view of the motion of two granular rafts at an oil-water interface. Each raft is made by 50 ZrO beads (density  $3,800 \text{ kg}\cdot\text{m}^{-3}$ , radius  $0.45 \text{ mm}$ ). Time between two photos:  $0.4 \text{ s}$ . Scale bar:  $5 \text{ mm}$ .

The model we develop strongly relies on the assumption that the discrete nature of a raft can be neglected to account for its motion (the raft is described as a heavy membrane). Nevertheless, this global approach is not sufficient if one wants to describe other effects, such as erosion.

### Erosion of a granular raft

When a granular raft is made of small enough particles (radius  $R_{part} < 0.2$  mm), erosion can occur [4] if its speed exceeds a given threshold. Particles detach behind the raft, modifying its global shape while it is still moving. This erosion mechanism is illustrated in figure 2, where a granular raft has been filmed from above during its motion at an increasing speed. The general shape of the raft changes as the velocity increases, until a point where it cannot even maintain the cohesion of its constitutive elements, leading to the loss of a few beads behind. Surprisingly, the threshold for erosion does not seem to depend strongly on the raft size, even though the attractive force between two rafts is greatly enhanced when more particles are added.

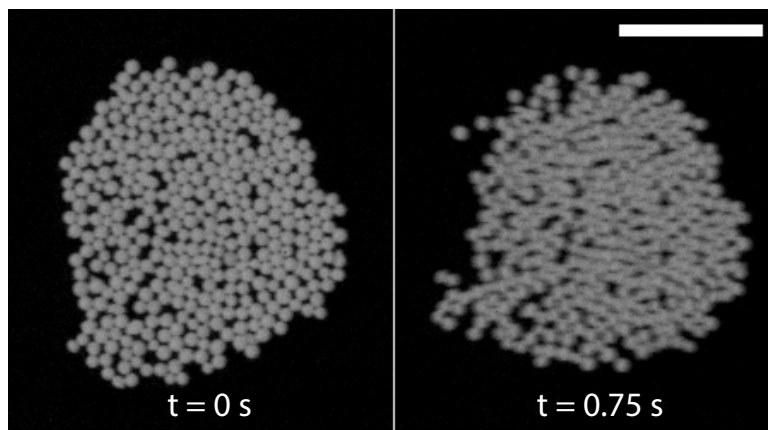


**Figure 2:** Top view centered on a granular raft (ZrO beads, density  $3,800 \text{ kg}\cdot\text{m}^{-3}$ , radius  $0.125 \text{ mm}$ ) during its motion at an oil-water interface. The motion of the raft is directed to the right, and its instantaneous speed increases from left to right. Time between the two photos:  $0.75 \text{ s}$ . Scale bar:  $3 \text{ mm}$ .

We propose a model experiment to characterize the cohesion force. For small particles (Bond number  $Bo = (R/\ell_c)^2 < 0.002$ , with  $\ell_c$  the capillary length), this force appears to be several orders of magnitude higher than the capillary force predicted by the classical linear Cheerios effect [1]. We quantify the dependency between this cohesion force and the particle parameters (radius, density, contact angle).

### Conclusion

The aggregation of particles at an interface has been thoroughly studied for a model system of two interacting clusters, for which both the capillary and drag forces have been deduced from velocity measurements. The erosion of a raft has also been characterized, through the measurement of the force responsible for its cohesion.

From this understanding of the interaction between two rafts, as well as of their cohesion, we wish to generalize to a system of  $n$  rafts, each one constituted by a random number of particles, and describe statistically the aggregation process of such  $n$ -body system, from the distribution of sizes through time to the duration of collapse of all the particles into one single object.

### References

- [1] Vella, Dominic and Mahadevan, L. American journal of physics **73**, 817–825 (2005).
- [2] Protière, Suzie and Josserand, Christophe and Aristoff, Jeffrey M and Stone, Howard A and Abkarian, Manouk. Physical review letters **118**, 108001 (2017).
- [3] Nicolson, MM. Mathematical Proceedings of the Cambridge Philosophical Society **45**, 288–295 (1949).
- [4] Vassileva, Nikolina D and van den Ende, Dirk and Mugele, Frieder and Mellema, Jorrit. Langmuir **23**, 2352–2361 (2007).



## Magnetically powered deformation waves induce locomotion in self-assemblies

Ylona Collard<sup>1</sup>, Galien Grosjean<sup>1</sup>, and Nicolas Vandewalle<sup>1</sup>

<sup>1</sup>GRASP, CESAM - Physics Department, University of Liège, B-4000 Liège, Belgium  
E-mail: [ycollard@uliege.be](mailto:ycollard@uliege.be), URL: <https://www.grasp.uliege.be>

### Introduction

In recent years, many efforts have been made to create synthetic microswimmers. These tiny structures use a wide variety of techniques to move in a fluid at low Reynolds number. Some mimic living microorganisms with artificial flagella while others are propelled by chemical reactions or strong external gradients [1,2]. The motivations for studying these systems range from the fundamental understanding of biological processes to the development of medical and technological applications. However, the synthesis, manipulation and assembly of the required microscopic components can be a challenge. In this paper, we suggest a different approach, we place tiny particles on a liquid interface where the microsystem self-assembles driven by external magnetic fields.

### Bioinspired swimming strategy

When tiny particles are placed at a water-air interface it creates a curvature of the surface around each one of them. This deformation is due to gravity and depends on the shape, buoyancy, and wetting properties of the particles [3]. Nearby particles will therefore attract or repel, as each particle experiences an inclination of the interface caused by the presence of another. Identical spheres will thus deform the interface in the same way, inducing an attraction between them. This phenomenon of agglomeration is playfully called the Cheerios effect [3]. In order to control the interaction between the particles we use tiny soft ferromagnetic spheres. To avoid the contact between them, a vertical magnetic field  $B_z$  is applied perpendicular to the interface. This magnetic field induces magnetic dipoles in the particles leading to repulsive interactions between them. The balance between capillary attraction and magnetic repulsion leads to an equilibrium distance larger than the particle diameter  $D$  for high enough field values. In a series of recent works [2,4,5], we proved that  $N$  floating soft-ferromagnetic particles at a liquid-air interface self-organize into well ordered floating rafts. Here, we demonstrate that precessing magnetic fields induce deformation waves on the periphery of magnetocapillary self-assemblies, similar to the ones observed for ciliated organisms. These deformation waves produce a net and controllable locomotion at low Reynolds number. This collective collaboration between particles takes advantage of many-body interactions in order to develop specific functions along fluid interfaces.

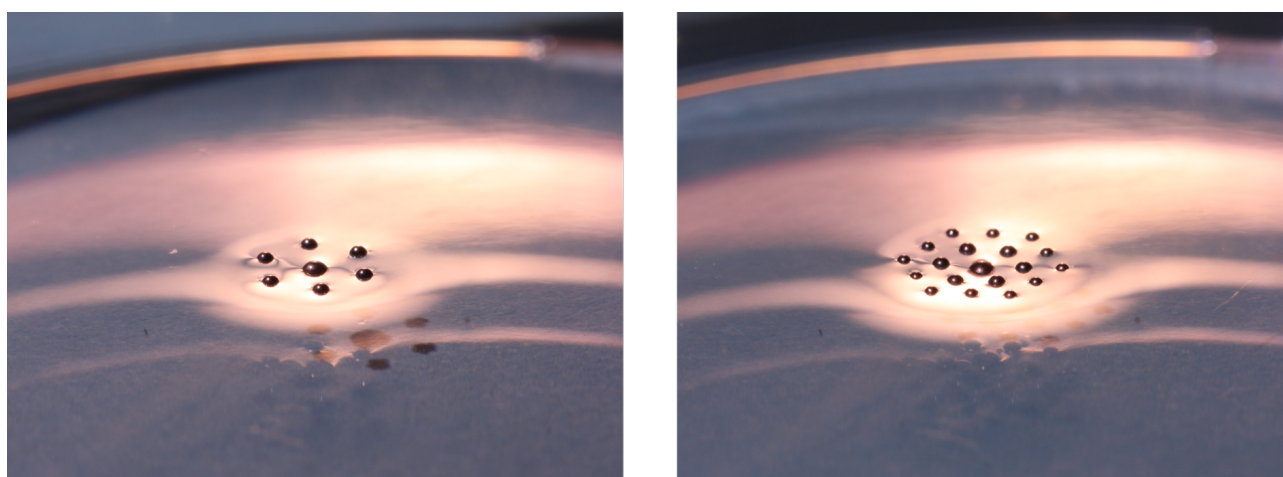


**Figure 1:** Typical magnetocapillary self-assemblies. (Left) Picture of the interface where the 7-bead assembly floats, emphasizing the deformation of the liquid around each particle. The 6 small beads form a hexagonal ring around the larger one. (Right) Assembly of 19 beads of three different sizes. The diameter of the smallest beads is  $400 \mu\text{m}$  giving the scale of the pictures.

## Conclusion

By using a bioinspired strategy, we show that assemblies of particles subjected to magnetocapillary interactions are able to swim powered by precessing magnetic fields. The swimming regime at low Reynolds number is similar to the one propelling bacteria and other microorganisms covered by cilia. We are looking forward to presenting at the summer school *Complex Motion in Fluids 2019* at Kysthusene, near Gilleleje, Denmark, on 18 - 24 August 2019.

## References

- [1] E. Lauga, T. R. Powers, *Rep. Prog. Phys.*, **72**, 096601 (2009)
- [2] G. Grosjean, M. Hubert, Y. Collard, S. Pillitteri, N. Vandewalle, *Eur. Phys.J.E*, **41**, 137 (2018).
- [3] D. Vella, L. Mahadevan, *Am. J. Phys.* **73**, 817–825 (2005).
- [4] G. Grosjean, G. Lagubeau, A. Darras, M. Hubert, G. Lumay, N. Vandewalle, *Sci.Rep.*, **5**, 16035 (2015).
- [5] G. Grosjean, M. Hubert, N. Vandewalle, *Adv. Colloid Interface Sci*, **255**, 84 (2018).



## Sticky creases in soft solids resemble free-surface cusps

Martin H. Essink<sup>1</sup>, Anupam Pandey<sup>1</sup>, Jacco H. Snoeijer<sup>1,2</sup>

<sup>1</sup>Physics of Fluids Group, Faculty of Science and Technology, Mesa+ Institute, University of Twente, 7500 AE Enschede, The Netherlands.

E-mail: [m.h.essink@utwente.nl](mailto:m.h.essink@utwente.nl), URL: <http://pof.tnw.utwente.nl>

<sup>2</sup>Mesoscopic Transport Phenomena, Eindhoven University of Technology, Den Dolech 2, 5612 AZ Eindhoven, The Netherlands.

### Introduction

When a slab of soft elastic material is compressed past a certain critical strain, the free surface of this material becomes unstable to form a crease, and is often observed on swelling gels or growing tissues. Creases are characterised by folded surface making a self-contact, indicated by the length  $L$  in figure 1a. Even though the nucleation, propagation and hysteresis in creases has been studied in detail [1], understanding of the local morphology of surface creases is still at an early stage. Recently, it has been shown that a crease follows a cusp shape with a diverging curvature at the tip [2]. However, in analogy to liquids one could expect the solid surface tension to play a significant role at the highly curved crease edge, which is yet to be explored. By combining finite element simulations and scaling arguments we take a close look at the local morphology of an adhesive crease. Unlike the usual smoothed free-surface cusps, we find that elasticity always imposes an infinite curvature. Remarkably, however, the resulting similarity scalings remain the same (fig. 1b) [3].

### Scaling arguments and numerical results

We consider the horizontal compression of a two dimensional slab of material, allowing for a crease of length  $L$ . Under these conditions we know that the free surface of a non-adhesive crease follows the following scaling law near the crease ( $x \ll L$ ) [2],

$$\frac{y - y_0}{L} \sim \left[ \frac{x}{L} \right]^{2/3}. \quad (1)$$

Further away from the crease ( $x \gg L$ ) the surface will have transitioned towards a flat state.

Surface tension gives rise to a new inner region, characterised by the elastocapillary length  $\gamma/G$ . When  $x \ll \gamma/G$  the problem is dominated by capillary forces. Relating the pressure in a folded elastic substrate to the capillary equations provides the scaling law describing the shape of the free surface in this region near the contact line,

$$\kappa \simeq \frac{\partial^2 y}{\partial x^2} \simeq -\frac{3}{2} \frac{G}{\gamma} \log \left( \frac{G}{\gamma} x \right). \quad (2)$$

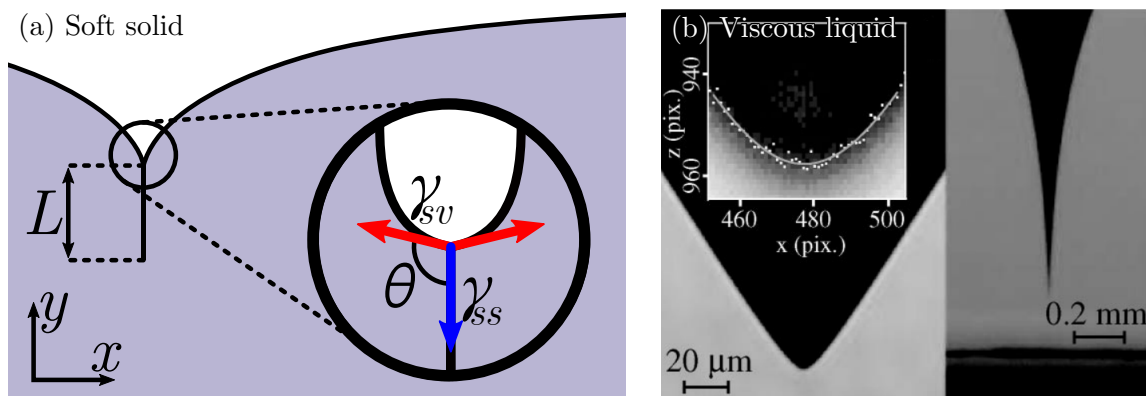


**Figure 1:** (a) Schematic representation of an adhesive crease in a soft solid substrate. The inset shows the structure of the crease near the contact line, which has a well-defined contact angle  $\theta$ . The contact angle is set by the solid-vapor  $\gamma_{sv}$  and solid-solid  $\gamma_{ss}$  surface energies. (b) Analogous structure of a liquid interface near a cusp in viscous flow. Reproduced from [4].

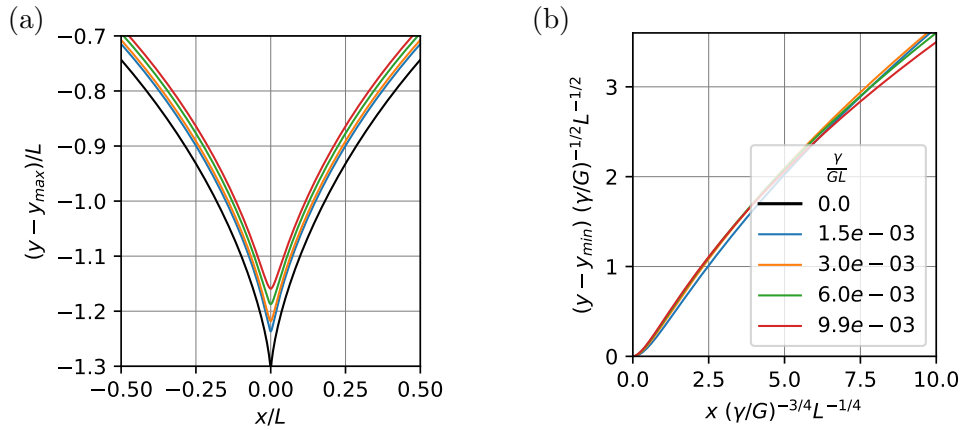


**Figure 2:** (a) Free surface profiles of adhesive creases for different values of the elastocapillary length ( $\gamma/G$ ). (b) Rescaled using the scaling of equation 3.

For a free-surface cusp one would expect the curvature in this third region to be a constant, resulting in a parabolic shape [3]. However, the adhesive crease has a logarithmic correction in the curvature, which will slightly alter the shape. Since this correction is sub-dominant to the parabolic shape of the interface, we can reasonably expect that both solutions do still scale similarly.

Similar to the scaling law for a cusp [2, eq. 4], from equations 1 and 2 one can derive a universal scaling law that collapses all solutions onto a single curve by rescaling  $x$  and  $y$  by respectively,

$$\ell_x = \left[ \frac{\gamma}{G} \right]^{3/4} L^{1/4} \quad \ell_y = \left[ \frac{\gamma}{G} \right]^{1/2} L^{1/2}. \quad (3)$$

To verify the claims on the shape of the free surface of the adhesive crease, we take a close look at the results from the finite element simulations of this problem. The finite elements simulations are performed using the multi-physics library oomph-lib [5]. A fixed length fold with surface tension and contact angle is imposed on the substrate, and is solved to find the compression and free surface shape.

In figure 2a the free-surface profiles are shown for a number of elastocapillary lengths. This shows that the profiles are indeed smoothed when surface tension is present, and when the surface tension increases the range over which this effect is visible increases accordingly. In the limits of both equation 1 and 2 it is also possible to overlay the respective numerical profiles onto the scaling laws, suggesting these are indeed correct.

The numerical free-surface profiles are plotted using to the universal scaling law (eq. 3) in figure 2b, showing the profiles do indeed collapse onto a single curve.

## Conclusion

We find a strong resemblance between adhesive creases in soft solids and free-surface cusps in viscous flow and we identified the scaling laws of the self-similar structure of the crease. We are currently working on additional theory and experimental validation, which we are looking forward to presenting at the summer school *Complex Motion in Fluids 2019* at Kysthusene, near Gilleleje, Denmark, on 18 - 24 August 2019.

## References

- [1] Dervaux, J. and Amar, M.B., *Annu. Rev. Condens. Matter Phys.* **3(1)**, 311-332 (2012).
- [2] Karpitschka, S., Eggers, J., Pandey, A., & Snoeijer, J. H., *Physical review letters* **119(19)**, 198001 (2017).
- [3] Jeong, J.T. and Moffatt, H.K., *Journal of fluid mechanics* **241**, 1-22 (1992).
- [4] du Pont, S.C. and Eggers, J., *Physical review letters* **96(3)**, 034501 (2006).
- [5] Heil, M. and Hazel, A.L., *Fluid-structure interaction*, 19-49 (2006).



## Optimal choice of bow and arrows in archery

Tom Maddalena<sup>1</sup>, Christophe Clanet<sup>1</sup>, Caroline Cohen<sup>1</sup>

<sup>1</sup>LadHyX, Ecole polytechnique, Palaiseau, France  
E-mail: tom.maddalena@polytechnique.edu

### Introduction

Archery is an Olympic sport, where the athlete stands 70 m from a target made of 10 concentric rings (figure 1a and b). We show on figure 1c, a typical arrow dispersion obtained with an international level athlete from the French archery team. The choice of the equipment is essential, in order to minimize this dispersion. Several mechanical phenomena occur during the release of an arrow and its flight ([1-3]). However, to our knowledge, there is no literature on the archer accuracy himself. In this work, we study experimentally the different sources of inaccuracy in archery, and their consequences in term of final dispersion.

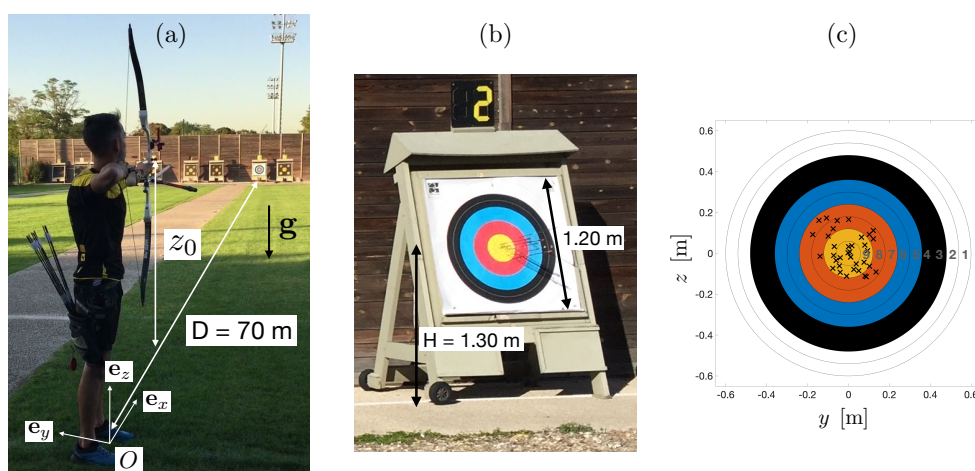


**Figure 1:** (a) Back view of an archer shooting on a target, standing at 70 m. (b) Picture of a target. Its height is 1.20 m and its center is located 1.30 m from the ground. (c) Typical dispersion of arrows of an archer. Each cross represents the position of one arrow on the target. The 36 arrows were shot by the archer shown on figure (a) during a training session.

### Optimal bow strength of a bow

To throw the arrow, the archer has to stretch his bow, that exerts a force  $F_0$  on his hand. It is intuitive that when  $F_0$  increases, it is more and more difficult to maintain a good accuracy. Nonetheless, high level archers use bows which strength ranges from 18 to 25 kg when only 5 kg is enough to reach the target. By solving the equation of motion for the arrow, we find that there is two main sources in the archer inaccuracy: A fluctuation of the initial angular position  $\delta\theta_0$ , and a fluctuation in the force  $\delta F_0$ . Those fluctuations are characterized experimentally with a model experiment described on figure 2a: A person stretches an elastic band and aims with a laser pointer on a target. We track the motion of the laser as well as the force with time, and measure their fluctuations. We deduce from those experiments the evolution of the typical arrows dispersion with the bow strength, that is shown on figure 2b. We find that it reaches an optimal value. For an international level athlete of the French archery team, this optimal value is close to the one he uses.

### Optimal size of the feathers

We study experimentally the role of the feathers on the arrow's flight (figure 3a). We first shoot several arrows with a shooting machine, using different feathers of different sizes. The dispersion of the arrows thus obtained is presented on figure 3b and c. It is much larger for experiments with no feathers on the arrow, that confirms the essential role of the feathers in reducing the dispersion. We also measure experimentally the aerodynamic forces exerted on the arrow in a wind tunnel. We use those experiments to conduct numerical simulations of the arrow flight. First results suggest that an optimal value exists for the size of the feathers, that minimizes the final dispersion.

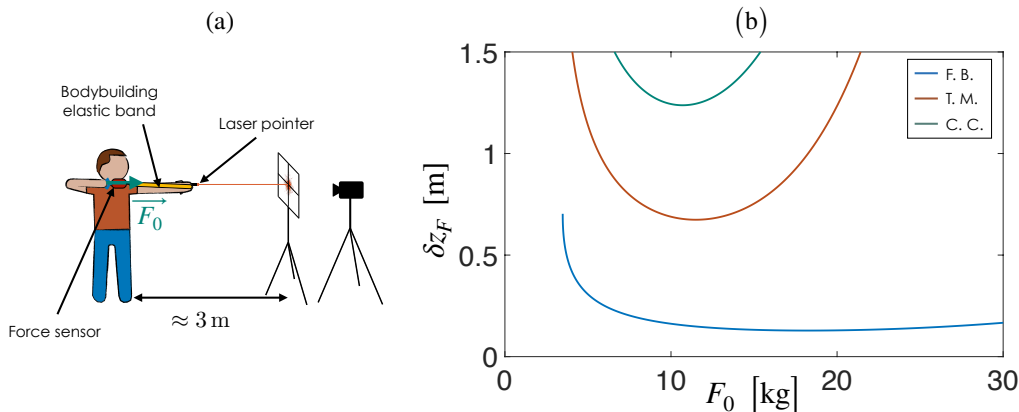


**Figure 2:** (a) Schematic view of the model experiments. A person stands 3 m from a wall and aims at a target with a laser pointer in his hand. A high speed camera records the motion of the laser on the wall. The subject stretches an elastic band between his two hands. A force sensor is attached between the elastic band and the right hand in order to measure the time evolution of the force created. (b) Prediction of the typical dispersion of the final position of the arrow on the target with the strength of the bow. It has been plotted for three subjects: One athlete in blue, and two novices in red and green.

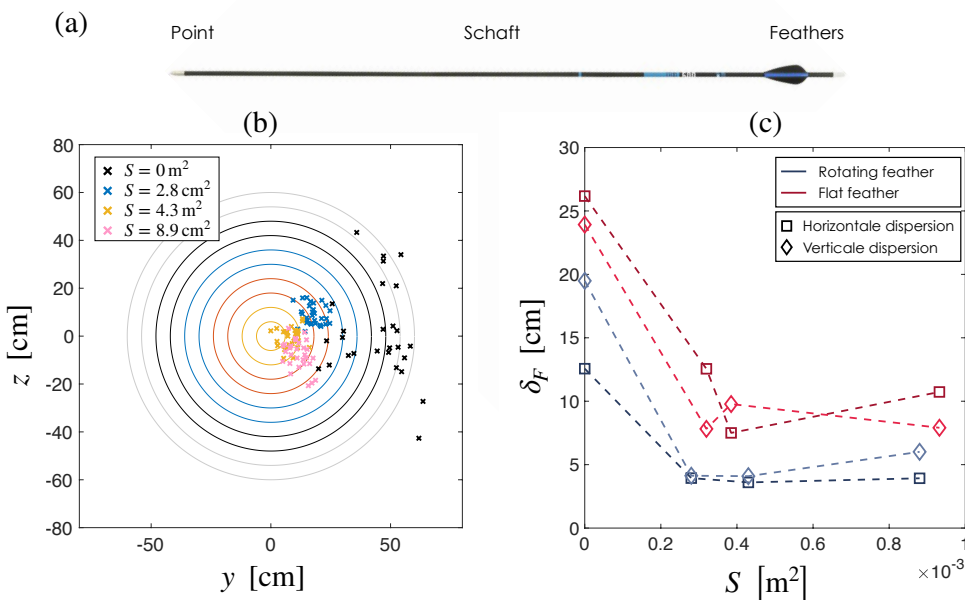


**Figure 3:** (a) Picture of an arrow used in archery. The feathers are fixed at the back of the arrow. (b) Position of the arrows on a target, using a shooting machine. The black crosses correspond to the position of arrows with no feathers. Each color correspond to a different size of the feathers. (c) Size of the dispersion with the feathers surface. The blue points correspond to twisted feathers, and the red ones to flat feathers.

**Conclusion**

In this work, we investigate the different sources of inaccuracy in archery, and how an archer should adapt his equipment consequently. More work is needed to better understand the initial condition given to the arrow. The interaction between the archer fingers and the string (the so called "archer paradox" [4]) seems especially to play an essential role on the final dispersion. It still needs to be characterized more accurately, in order to fully describe the flight of an arrow.

**References**

[1] H. Meyer. arXiv:1511.02250, (2015).  
 [2] Lieu D.K Kim JKKC (2015).  
 [3] Miyazaki T, et al. Sports Engineering 359 (2013)  
 [4] Park JL, Logan O, Journal of Sports Engineering and Technology (2013)



# An improved immersed boundary method for Neumann boundary conditions with the application to Janus particle

Yibo Chen<sup>1</sup>, Xiaojue Zhu<sup>1</sup>, Kai Leong Chong<sup>1</sup>, Roberto Verzicco<sup>3,1,4</sup>, and Detlef Lohse<sup>1,2</sup>

<sup>1</sup>Physics of Fluids Group and Max Planck Center Twente for Complex Fluid Dynamics, MESA+ Institute and J. M. Burgers Centre for Fluid Dynamics, University of Twente, P.O. Box 217, 7500AE Enschede, The Netherlands

<sup>2</sup>Max Planck Institute for Dynamics and Self-Organization, 37077 Göttingen, Germany

<sup>3</sup>Dipartimento di Ingegneria Industriale, University of Rome "Tor Vergata", Via del Politecnico 1, Roma 00133, Italy.

<sup>4</sup>Gran Sasso Science Institute - Viale F. Crispi, 767100 L'Aquila, Italy.

\*E-mail: [y.chen-4@utwente.nl](mailto:y.chen-4@utwente.nl)

## Introduction

Janus particle is a special kind of colloidal particle with different chemical configurations on each side of the hemispherical surface, and this asymmetric setting leads to its self-propulsion. Owing to its richness in particle dynamics and applications, there have been extensive studies on this topic in recent years. However, due to the small length scale of the Janus particle, the current measurements from experiment cannot capture all the details of the dynamics. Thus, the numerical approach becomes essential to give a better insight of this problem. One of the numerical approaches is Immersed Boundary (IB) method which was first introduced by Peskin in 1972 to simulate cardiac mechanics and the associated blood flow [1]. In this method, the boundary of the particle is represented by Lagrangian points and through the transfer function, the boundary conditions can be transferred to the Eulerian grid so that the flow solver can be run on a simple Cartesian grid. The concentration boundary condition for Janus particle is Neumann boundary condition which is a fixed concentration gradient. Commonly, IB method has been widely used for Dirichlet boundary condition (fixed value) [2], however, adopting Neumann boundary condition has posed the challenge in terms of the methodology and accuracy. In this research, we propose the modified probe method which can accurately deal with Neumann boundary condition within IB method. Our method has been validated by the theoretical model for a single and isolated Janus particle [3] which gives excellent agreement. Our method can potentially simulate multiple Janus particles and thus it may be a useful tool for the community.

## Results

The Navier-Stokes equations are solved on fixed Eulerian grids. The discretisation and Navier-Stokes solver are the same as that in [4]. The idea of IB method is to add volume force to impose the desired values at selected grid node. The incompressible Navier-Stokes equations with volume force read:

$$\partial_t \mathbf{u} = -(\mathbf{u} \cdot \nabla) \mathbf{u} - \frac{1}{\rho} \nabla p + \nu \nabla^2 \mathbf{u} + \mathbf{f}, \quad (1)$$

where  $\mathbf{u}$  is the velocity,  $\rho$  is the density of the fluid,  $p$  is the pressure and  $\mathbf{f}$  is the volume force for satisfying the boundary condition. Different from the usual approach, we calculate the force by using its value at the previous timestep:

$$F^n = \frac{U - u}{dt} + F^{n-1} \quad (2)$$

where  $F^n$  is the Lagrangian force at the timestep  $n$ ,  $U$  is the imposed velocity at the surface, and  $u$  is the velocity interpolated at the Lagrangian point. According to the numerical result (Fig.1), the force correction would improve the accuracy and speed up the convergence.

For the Neumann boundary condition we use a probe method to satisfy it. We consider the following Neumann boundary condition:

$$-D \nabla c(\mathbf{x}, t) \cdot \mathbf{n} = \alpha, \quad (3)$$

where  $D$  is the diffusion coefficient,  $c(\mathbf{x}, t)$  is a scalar concentration,  $\mathbf{n}$  is the unit normal vector and  $\alpha$  is the concentration gradient at the surface.

We use two inner probes (Fig.1 (a)) to satisfy the boundary condition:

$$-D \frac{c_o - c_{i1}}{2h} = \alpha, \quad (4)$$

$$-D \frac{c_o - c_{i2}}{3h} = \alpha, \quad (5)$$

where  $c_o$  is the concentration at the outer probe point, and  $c_{i1}$ ,  $c_{i2}$  are correspondingly the concentration at the inner probe point 1 and 2. The two-inner probe method guarantees that the concentration at the surface of the particle is second-order accurate.

To test the proposed method, we validate our numerical result through the theoretical result for a single and isolated Janus particle [3]. The validation includes three steps. First, we show whether the concentration field on the surface of Janus particle has been accurately simulated. There is an analytical solution for how

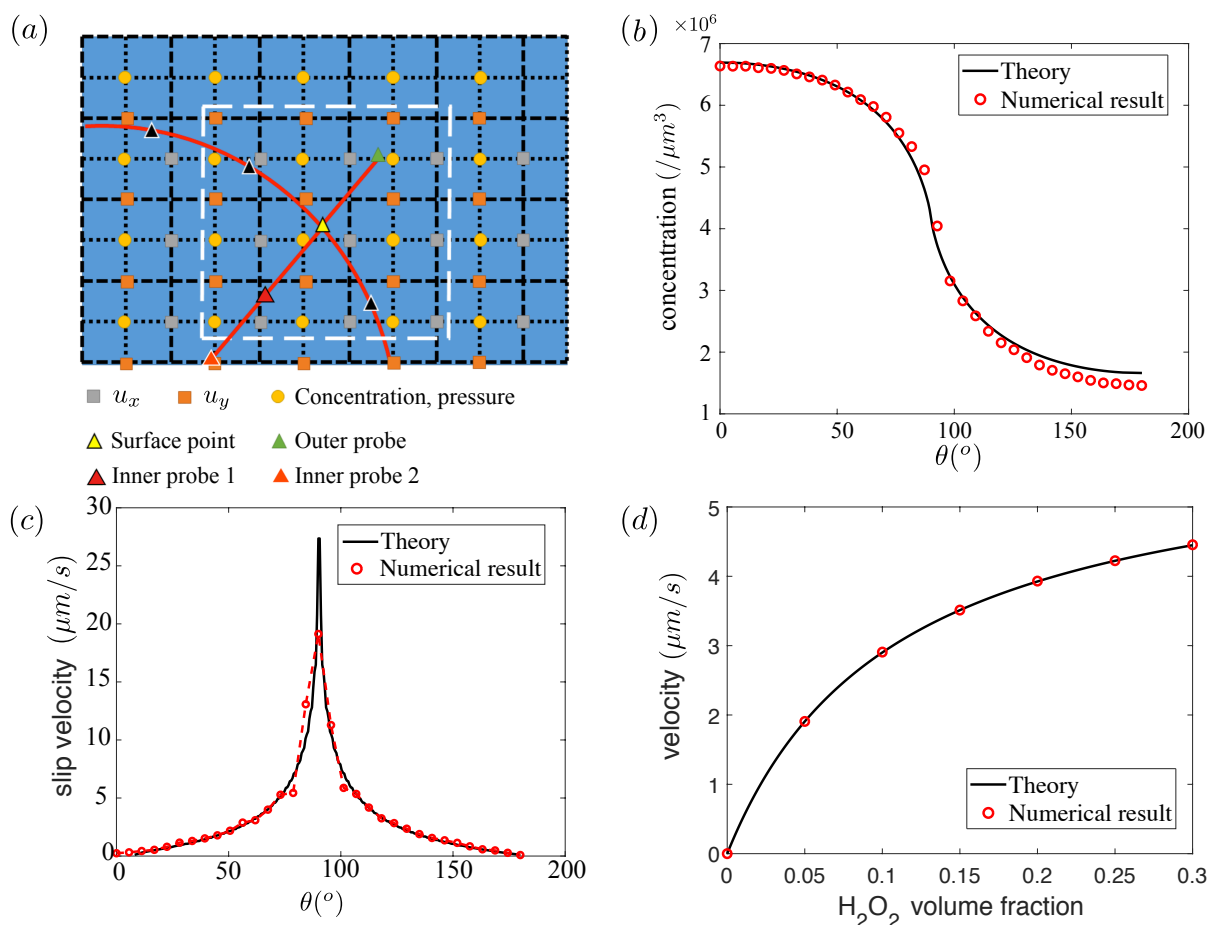


**Figure 1:** The 2D schematic sketch (a) of the numerical method, and the validation by the theoretical result of the Janus particle [3] (b-d). (a) 2D schematic description of the method with two inner probes and an outer probe. (b,c) The theoretical (solid line) and numerical results (red circle) for concentration (b) and slip velocity (c) at different azimuthal angle  $\theta$ . (d) The terminal velocity of Janus particle in  $\text{H}_2\text{O}_2$  solutions with different volume fractions.

the concentration on the surface of particle changes with azimuthal angle, and Fig 1(b) shows indeed a good agreement. Second, for simulating Janus particle, the gradient of concentration is also important. The slip velocity on the surface of particle depends on the concentration gradient at the surface and in Fig.1 (c), again the nice agreement is obtained. Finally, we compare the thermal velocity of Janus particle for different  $\text{H}_2\text{O}_2$  volume fraction in Fig. 1(d). Not only the trend, but also the exact magnitude of the terminal velocity agrees nicely with the theory.

## Summary

In our study, we present a boundary condition enforced method via the immersed boundary method to simulate three-dimensional incompressible viscous flows with Neumann boundary conditions. We improve the code in the following aspects: a) We develop a force correction scheme to calculate the Lagrangian forces; b) We use two probes inside the immersed body to derive the physical quantities on the boundary which satisfies the Neumann boundary condition with 2nd order accuracy. These techniques are implemented in a second order finite difference solver. The code is tested by the case of Janus particles, the results agrees excellently with theoretical result.

## References

- [1] C. S. Peskin, *J. Comput. Phys.* **10**, 252-271 (1972).
- [2] W. Ren, C. Shu, J. Wu, and W. M. Yang, *Comput. Fluids* **57**, 40-51 (2012).
- [3] R. Golestanian, T. Liverpool, and A. Ajdari, *New J. Phys.* **9**, 126 (2007).
- [4] V. Spandan, V. Meschini, R. Ostilla-Mónico, D. Lohse, G. Querzoli, M. D. de Tullio, and R. Verzicco, *J. Comput. Phys.* **348**, 567-590 (2017).



# Two-dimensional inviscid Faraday waves: effect of the static contact angle

A. Bongarzone<sup>1</sup>, F. Viola<sup>2</sup>, and F. Gallaire<sup>1</sup>

<sup>1</sup>Laboratory of Fluid Mechanics and Instabilities, École Polytechnique Fédérale de Lausanne, CH-1015, Switzerland

E-mail: [alessandro.bongarzone@epfl.ch](mailto:alessandro.bongarzone@epfl.ch)

<sup>2</sup>Department of Industrial Engineering, University of Roma Tor Vergata, Italy

## Introduction

The flat interface between two fluids, i.e. a liquid and its vapor, in a vertically vibrating container may be parametrically excited with consequent generation of standing waves, whose stability depends on the combination of the external control parameters, the forcing amplitude,  $f$ , and frequency,  $\Omega$ . In presence of a dissipation source, the strongest parametric resonance is the sub-harmonic one. From a theoretical point view, this classic problem has been extensively studied under the potential flow hypothesis, with a viscous damping coefficient usually added a posteriori in a phenomenological way. Nevertheless, the literature lacks a comprehensive study including the effect of the static angle and thus of an initially non-flat free surface. The main aim of the present work is to formulate a mathematical approach allowing to introduce the meniscus effect and study numerically how this one affects the stability of the free surface associated with the sub-harmonic parametric resonance.

## Governing Equations and weakly nonlinear analysis

We consider a two-dimensional rectangular container of width  $2L$  and filled to a depth  $H$  with an inviscid fluid of density  $\rho$ . The line of contact,  $\Gamma$ , with the lateral solid walls,  $\partial\Sigma$ , is assumed to be able to freely slide (a realistic contact line dynamics, i.e. the contact angle hysteresis due to capillary effects at the solid walls is not considered); a static contact angle different from the classic value,  $\pi/2$ , which corresponds to an initially flat free surface,  $\eta$ , is introduced; in particular, values of  $\theta_s < 90^\circ$  imply the presence of a curved static meniscus. Under the mentioned hypothesis, the nondimensional ( $Bo = \rho g L^2 / \sigma$ : Bond number,  $\sigma$ : surface tension) governing equations describing the problem, in a non-inertial reference framework, read:

$$\nabla^2 \Phi = 0 \quad , \quad \nabla \Phi \cdot \mathbf{n}|_{\partial\Sigma} = 0, \quad (1)$$

$$\left. \frac{\partial \Phi}{\partial t} \right|_{\eta} + \frac{1}{2} \nabla \Phi|_{\eta} \cdot \nabla \Phi|_{\eta} + \eta (1 - f \cos \Omega t) - \frac{1}{Bo} \kappa(\eta) = 0 \quad z = \eta, \quad (2)$$

$$\left. \frac{\partial \eta}{\partial t} + \nabla \Phi|_{\eta} \cdot \nabla \eta - \frac{\partial \Phi}{\partial z} \right|_{\eta} = 0 \quad z = \eta, \quad (3)$$

$$\theta - \theta_s = 0 \quad , \quad \nabla \eta \cdot \mathbf{n}|_{\Gamma} = \cot \theta, \quad (4)$$

where  $\Phi$  is the velocity potential,  $\kappa(\eta)$  the nonlinear surface curvature, while  $f$  and  $\Omega$  are the forcing amplitude and frequency, respectively. The system (1)-(4) is nonlinear and it can not be solved analytically: in the present work we perform a weakly nonlinear analysis through the multiple scale technique and valid in the limit of small external parameters, amplitude  $f$  and the detuning  $\lambda$  (defined in (5)). Let's define the state vector  $\mathbf{q} = \{\Phi, \eta, \theta\}^T$  and introduce the following asymptotic expansions:

$$\mathbf{q} = \mathbf{q}_0 + \epsilon \mathbf{q}_1 + \epsilon^2 \mathbf{q}_2 + \epsilon^3 \mathbf{q}_3 + \mathcal{O}(\epsilon^3) \quad , \quad f = \epsilon^2 F \quad , \quad \Omega = 2\omega + \epsilon^2 \lambda \quad , \quad T = \epsilon^2 t, \quad (5)$$

being  $\omega$  the considered sloshing frequency,  $T$  a slow time scale and  $\epsilon$  a small parameter. Substituting the expansions (5) in (1)-(4), a series of different systems are attained at the various order in  $\epsilon$ : at order  $\epsilon^0$ , the nonlinear equation associated with the shape of the static meniscus is obtained; at order  $\epsilon$ , the classic eigenvalue problem for inviscid sloshing waves is retrieved; at order  $\epsilon^2$ , a linear system forced by the external forcing and previous order solutions is found; finally, at order  $\epsilon^3$ , an amplitude equation for the sloshing modes, which allows us to derive the linear marginal stability curves and to study the weakly nonlinear stability associated with the sub-harmonic parametric resonance in presence of a curved static meniscus, is formulated. This amplitude equation assumes the classic form present in literature,

$$\frac{dB(T)}{dT} + i\frac{\lambda}{2}B(T) + \alpha_1 F \bar{B}(T) + \alpha_2 |B(T)|^2 B(T) = 0, \quad (6)$$

however in Eq.(6), the complex coefficients,  $\alpha_1$  and  $\alpha_2$ , which include the effect of the static meniscus, are here computed numerically.

## Results

The study of Eq.(6) allows to describe the instability tongues and to take into account weakly nonlinear phenomena associated with the sub-harmonic resonance in the limit of small external parameters. These aspects have been investigated considering different Bond numbers,  $Bo$ , in the deep water regime ( $H/L \gg 1$ ); comparison between cases with  $\theta_s = 90^\circ$  and  $60^\circ$ , are shown in Fig.1.

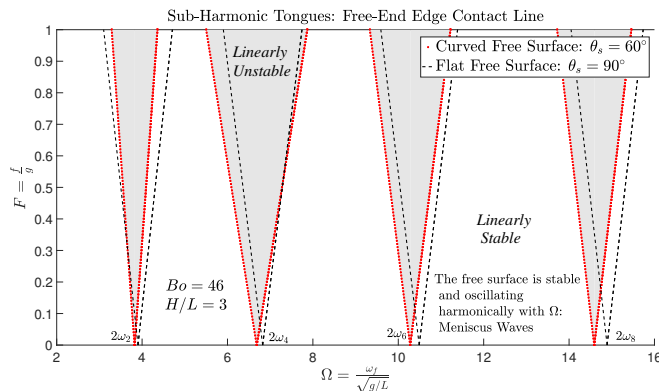


**Figure 1:** Neglecting the last term of (6) and studying its linear stability, the Faraday tongues associated with the sub-harmonic resonance in presence of a static meniscus are numerically evaluated. A low  $Bo$ , i.e.  $Bo = 46$ , implies a relevant meniscus, whose presence slightly modifies the sloshing frequencies, moving all the curves towards slower dynamics; moreover, presence of a static meniscus may perturb significantly the linearly unstable regions. The tongues related to the first four symmetric sloshing modes are illustrated.

Moving to a three-dimensional realistic configuration and introducing the fluid viscosity, it has been numerically computed how the free liquid surface appears below the instability onset. Preliminary results are shown in Fig.2.

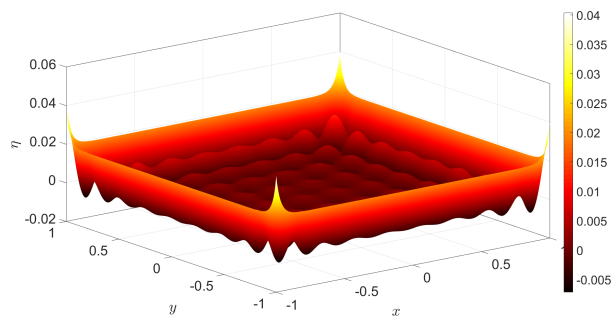


**Figure 2:** Three-dimensional viscous meniscus waves. Presence of viscosity moves the tongues progressively upwards, consequently increasing the instability threshold ( $F_{th} \neq 0$ ). However, out of the unstable Faraday tongues, the surface does not appear flat, indeed, the vertically excited static meniscus emits stable and harmonic (with the external forcing frequency  $\Omega$ ) surface waves, damped by viscosity moving from the lateral solid walls to the cell's center. The free surface pattern here shown (in nondimensional terms) corresponds to the following condition: square cross-sectioned container  $80 \times 80 \times 5mm$ , filled with silicone oil to a depth of  $2mm$  and vertically excited with forcing amplitude  $f = 4g$  and frequency  $\Omega = 20Hz$ ; a pinned-end edge contact line model is assumed.

## Conclusion

A vertically oscillating meniscus, in order to preserve the mass of fluid, always emits surface waves at the excitation frequency, indeed, the capillary length oscillates like the effective gravity acceleration. Consequently, in presence of a meniscus, the free surface is not flat and steady, even below the instability threshold. These so-called meniscus waves give a new initial condition for the Faraday instability and they perturb the parametric waves, since they are directly coupled with them. Through the asymptotic analysis performed (valid for small forcing amplitudes and detuning), it has been numerically studied how meniscus waves influence the linear stability. High Bond numbers (i.e.  $> 200 - 300$ ) imply a small static meniscus and consequently small meniscus waves, which do not significantly modifies the instability; on the other hand, for small Bond numbers, as shown in Fig.1, a significant meniscus is present: this slightly modify the natural sloshing frequencies (slower dynamics) and affects in a not negligible manner the classic Faraday instability.

## References

- [1] T. B. Benjamin and F. Ursell. Proc. R. Soc. Lond. A **225** (1163), 505-515 (1954).
- [2] S. Douady. J. Fluid Mech. **11** (1), 371-400 (1990).
- [3] K. Kumar and L. Tuckerman. J. Fluid Mech. **279**, 49-68 (1994).
- [4] S. T. Milner J. Fluid Mech. **225**, 81-100 (1991).
- [5] J. Rajchenbach and D. Clamond J. Fluid Mech. **777**, (2015).
- [6] F. Viola, P. T. Brun and F. Gallaire. J. Fluid Mech. **837**, 788-818 (2018).